Università degli Studi di Padova

Dipartimento di Fisica e Astronomia "Galileo Galilei"

Corso di Laurea in Astronomia

TESI DI LAUREA

Measuring relativistic corrections with a quadratic estimator for the galaxy power spectrum

Relatore:
Bertacca Daniele
CoRelatore:
Porciani Cristiano

Candidato:
Ieranò Giovanni
Controrelatore:
Cassata Paolo

Academic year 2021-2022

Contents

Abstract **vi**

1 Redshift Space Distortions **1**
1.1 Galaxy clustering 1
1.2 Redshift Space Distortions 8
1.3 Real space and Redshift space 12
1.4 Linear Redshift Distortion Operator 15
1.4.1 Linear Plane-Parallel Redshift Distortion Operator 17
1.5 Wide angle Redshift Space Distortions 18

2 Relativistic simulations **29**
2.1 General relativistic effects 29
2.2 LIGER theory 41
2.2.1 Magnification 48
2.3 LIGER method 49

3 Quadratic estimator **55**
3.1 Old Quadratic estimator 55
3.2 New Quadratic estimator 61
3.2.1 Maximum Likelihood estimator 64
3.2.2 FKP like matrix 66
3.3 The algorithm 66
3.3.1 Matrices inversion 66
3.3.1.1 Maximum Likelihood estimator 67
3.3.1.2 FKP like matrix 68
3.3.2 Calculating Bias and Fisher terms 68
3.3.3 Accumulating the estimator 69

4 Results **71**
4.1 The catalog 71
4.2 Method 74

4.2.1 Simulation volume 74
4.2.2 Monte Carlo simulations 76
4.2.3 Dependencies 78
4.2.4 FKP Comparison 82
4.3 Un-windowed power spectra 84

5 Conclusion **95**

The analysis of the large-scale structure of the Universe represents one of the most promising research fields in Cosmology in the next years. The continuous rising of the amount of data available from the surveys has brought us in the era of the precision cosmology, that means that our understanding in the Universe can be tested up to a precision level that was before impossible. In the last two decades, many experiments have been developed to this aim, leading to the development and observational confirmation of the concordance model ΛCDM (Lambda Cold Dark Matter), which describes the evolution of the components of the Universe. This model is far from be complete and very big questions still domain our understanding of the Universe, such as the nature of the Dark Matter and dark Energy, so it is crucial to use all the information we have available. In the Large Scale Structure field is well known that the study of the Redshift Space Distortions is one of the most interesting and promising subject, since they allow to test theory up to very large scales. They are due to the peculiar motion of the galaxies that alter the pattern of the galaxy configuration observed in the surveys, so it is crucial to account for them in order to recover a real map of the Universe. Nowadays modern galaxy surveys can observe very large and deep region, almost approaching the Hubble radius, and so can be demonstrated that, together with the Redshift Space Distortions, at this scale also General Relativistic effects such as Sachs-Wolfe effect (standard and integrated), Doppler and gravitational lensing and Shapiro time delay can modify the observed positions of the galaxies in Redshift space. The 3D map of a survey is a combination of the Redshift space distortions due to the peculiar velocity and the General relativistic effects. In this thesis we try to understand if these effects can leave an imprint in the Power Spectrum of a galaxy survey, making them distinguishable. In order to do this we use the LIGER code to create galaxy catalogs that contains these effects. We compute the Power Spectrum for these catalogs comparing them and understanding if they presents some differences. The different behavior that we are searching is dominant only in the large scale part of the Power Spectrum, where however the effect of the window function of the specific survey is dominant. It tends to flatten the power spectrum at large scale, destroying the information of the redshift space distortions, so the difference between the various Power Spectrum would be impossible to measure. We overlap this issue computing the Power Spectrum of the mock catalogs using the "Quadratic Estimator" code by Oliver Philcox that takes as input a galaxy mock and measure its Power Spectrum without the effects of the window function, making our analysis possible at all scales.
This thesis is organized as follow: in the first chapter we review the formation of the cosmic structure, introducing the theory of the Redshift Space Distortions, in the second chapter we review the General relativistic effects that have to be taken into account and will be shown how LIGER works, in the third chapter will be shown the theory of the Quadratic Estimator; finally in the fourth and fifth chapter will be presented our results and conclusion.

Chapter 1

Redshift Space Distortions

1.1 Galaxy clustering

In the thesis we set $c = 1$ and we use the common cosmological dimension in which the distances are in Mpc$/h$. The presence of the h term is due to the fact that nowadays the actual value of the Hubble constant is not known and various independent measurement of it give different values (see e.g. Valentino et al. 2021). For example the infer of $H(t)$ from Planck gives a value at present time of $H_0 = 67.8 \pm 0.9$ km s^{-1} Mpc^{-1} (P. A. R. Ade et al. 2016), while inference from the Chepeid distribution is $H_0 = 73.75 \pm 2.11$ km s^{-1} Mpc^{-1} (Cardona, Kunz, and Pettorino 2017). Thus the Hubble constant at present time is written as (Dodelson 2003)

$$H_0 = 100\, h \text{ km s}^{-1} \text{ Mpc}^{-1} = \frac{h}{0.98 \times 10^{10} \text{years}},$$

in which h contains the uncertainties on the actual value, so to specify the Hubble constant that one wants to adopt, we have to specify the value of h. We adopt $h = 0.67$.

The theory of the Large Scale Structure (hereafter LSS) suggests that they begin to form thanks to the gravitational instability process. It is based on the fact that at very early stage of the Universe, it was subjected to an incredible expansion called "Inflation". In this stage the energy for the expansion is due to the presence of the inflaton field, that is the particle (and so the field) that nowadays is associated as the "cause" of the inflation (see e.g. Turok 2002). In figure(1.1) is shown the value of the inflaton field (x-axes) and of its potential (y-axes). The potential of the inflaton at the beginning is almost flat, and this act as a "cosmological constant" allowing the Universe to expands. When inflation ends, the inflaton passes from the constant potential stage to the "bell" shape beginning to oscillate giving rise to the reheating phase, where the inflaton decays creating less massive particle (see e.g. Allahverdi et al. 2010). During the constant potential phase the scale factor suddenly increases, while the Hubble radius,

defined as (Dodelson 2003)

$$r_H(t) = \frac{1}{a(t)H(t)} \tag{1.1}$$

decreases. The term at the denominator is the Hubble constant defined (Dodelson 2003)

$$H(t) = \frac{\dot{a}(t)}{a(t)} \tag{1.2}$$

that quantifies the expansion of the Universe at time t. In figure(1.2) is shown a simple scheme that explain what happens during inflation. The red line is the Hubble radius, the solid black horizontal line is a generic scale k^{-1} and everything evolves with time (from left to right). k is the Fourier modes of a specific distance λ that we are considering, and they are related through $k = 2\pi/\lambda$ (Dodelson 2003), so k^{-1} means that we are referring to the specific length distance $\lambda/2\pi$ (for more details see section(1.3)). Inflation causes the Hubble radius to decreases and so a generic scale k^{-1} at a certain time becomes greater than it, entering in the regime of "super-horizon" scale, but when inflation stops, the Hubble radius becomes to rise, so the same scale becomes less than the Hubble radius (that when inflation ends it begins to increase) re-entering the stage of the "sub-horizon" scale (see e.g. Peebles 1980a, Dodelson 2003, Matarrese, Musso, and Riotto 2004, Gonzalez, Padilla, and Matos 2020). The inflaton being a quantum field is subjected to quantum fluctuations. (see e.g. Tsujikawa 2003). These primordial fluctuations once they cross the horizon are frozen and when they re-enter the horizon (and become sub-horizon) they are enhanced in macro-fluctuations, that means that they pass from a quantum stage to a classical stage (see e.g. Gonzalez, Padilla, and Matos 2020). After inflation the Universe begins its radiation-dominated era, during which the growth of matter perturbations is inhibited by the large pressure provided by the radiation. Perturbations in the coupled photon and baryon fluids oscillate with constant amplitude (see e.g. Dodelson 2003). Shortly before recombination, however, the Universe becomes matter dominated and the radiation pressure disappears, so that density fluctuations can start to grow under the influence of gravity. This growth of the matter perturbations led to the LSS of the Universe (see e.g. Peebles 1980a, Brandenberger 2001, Troxel, Peel, and Ishak 2013, Baumann 2018).

Dark matter halos are gravitationally bound regions of matter that have decoupled from the Hubble expansion and collapsed. Within the radius of a dark matter halo there may be multiple, distinct peaks in the density field with virialized clumps of dark matter gravitationally bound to them, where galaxies form. These sub-halos are smaller than the host halo, and they orbit within the gravitational potential of the host halo (Wechsler and Tinker 2018). Galaxies move with the flow of mass inside the dark matter halo in which are formed and so they will contribute to grow over-dense regions, and empty under-dense regions, creating the galaxy clustering. This because the force that drive this process is the gravitational one, so the matter following the potential is forced to

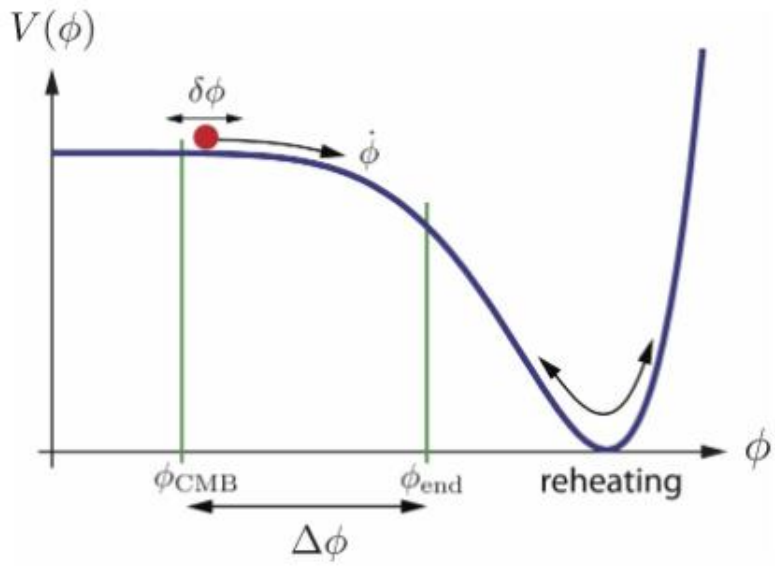

Figure 1.1: The schematic process of how the potential of the inflaton changes. At the beginning the inflaton potential remains almost constant, before beginning to oscillate during the reheating phase. (Figure from Gonzalez, Padilla, and Matos 2020).

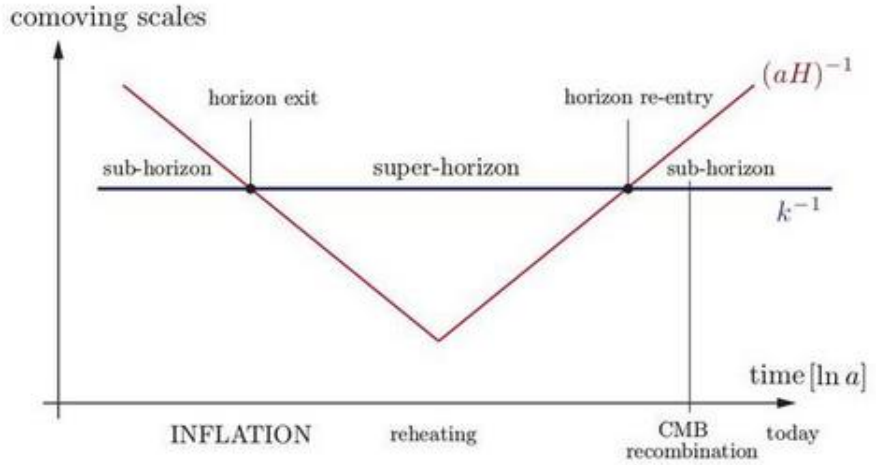

Figure 1.2: Behaviour of the Hubble radius (equation1.1) during inflation, in which are highlighted when a generic scale k^{-1} (as previous defined as $k = 2\pi/\lambda$) enters and exits the horizon (Figure from Nandi 2017a).

agglomerate at the centre of the potential, going from the under-dense region to the over-dense, making the first more under-dense and the second more dense (see e.g. Kravtsov and Borgani 2012). At a certain time the matter flow is so high that the over-dense region begin the radiative processes that allow creation the galaxies, that since are in the same dark matter halo, they resent the gravitational force of the others, and so they begin to agglomerate giving rise to the so called "galaxy clustering" (see e.g. Walker et al. 2019). This section is based on (A. J. S. Hamilton 1998, Bertschinger 1994) and it gives a review of how the perturbation in the density field growth in which we show how the perturbations in the density field grow, deriving a relation for the growing velocity of the perturbation in the linear regime, that will be useful in section(1.4).

Since the Universe expands we have to be careful when we define distances. We define the physical and the comoving distance(J. A. Peacock 1998). In figure(1.3) is shown a scheme that explain the difference between the distances. Imagine to select four points in the Universe (that for simplicity form a square), that tend to expand with the Universe. We define the comoving system as a reference frame that expands with the Universe, so each point is at rest in this frame (see the comoving coordinate) and they don't change their comoving distance, while their physical distance is changing, that is the actual distance between the points. Calling the physical distance $\mathbf{r}$ and the comoving one $\mathbf{x}$, they are related through (Dodelson 2003)

$$\mathbf{r} = a(t)\mathbf{x}, \tag{1.3}$$

in fact the changing of the physical distance is proportional to the expansion of the Universe, and so on the scale factor, which is set to $a(t_0) = a_0 = 1$. We define the comoving distance as the distance between a distant emitter at redshift $z = 1/a - 1$ and us as (Dodelson 2003)

$$\chi(a) = \int_{t(a)}^{t_0} \frac{dt'}{a(t')} = \int_a^1 \frac{da'}{a'^2 H(a')}, \tag{1.4}$$

Where we have changed the integration over t' to $1/a'$, which brings in the additional factor of $da/dt = aH$ in the denominator. We define also the conformal time as the time that is the distance light could have traveled in the absence of interactions since $t = 0$

$$\eta = \int_o^t \frac{dt'}{a(t')} \tag{1.5}$$

The reason this distance is so important is that no information could have propagated further than η since the beginning of time.

We have to distinguish between matter that satisfies a continuity equation given by equation(1.6) and galaxies which don't, because of galaxy formation and merging. The matter satisfies this equation since it is considered as a fluid, that at large scale

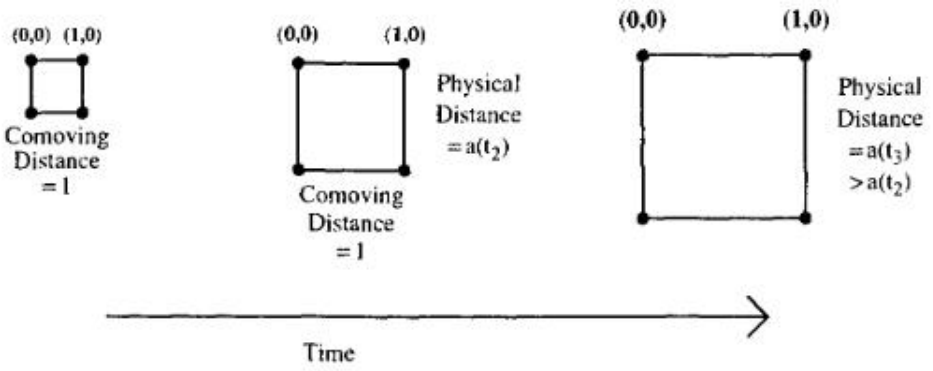

Figure 1.3: Taking four coordinate points that makes a square, is qualitatively shown the difference between the physical and comoving distance. The first depends on time and is bigger since the expasion of the square, while the latter remain constant, since it expands with the Universe.(Figure from Dodelson 2003)

can be treated at linear order. On the contrary galaxies are formed in a high non-linear regime, where the perturbations are not $|\delta_M| \ll 1$, and so the matter perturbation are so high that they collapse, giving rise to the formation of galaxies (Somerville and Davé 2015, Benson 2010). In LSS analysis we use the galaxies as tracers of the underlying matter field, this means that we use the first to infer properties of the second, but we have to take into account the fact galaxy surveys do not measure the matter density field itself, but rather the distribution of galaxies, that is, of highly nonlinear objects which are the result of a complex formation process. Bias describes, in a statistical sense, the relation of the distribution of these objects to that of matter, that means that we use it to connect the galaxy distribution to the matter one (see e.g. Coles 1986, Demiański and Doroshkevich 1999, Cooray and R. Sheth 2002, Desjacques, Jeong, and Schmidt 2018) . The linearized continuity equation for the matter is given by (A. J. S. Hamilton 1998)

$$\beta\delta + \nabla \cdot \mathbf{v} = 0, \tag{1.6}$$

with β the value that solves this equation and $\mathbf{v}$ the *irrotational* velocity (as predicted by gravitational growth theory). As we now will show equation(1.6) can be linearized if we are in the linear regime, that means that the perturbations are small $|\delta \ll 1$ (see below). The continuity, Euler and Poisson equations for cold pressurless matter in a perturbed Friedmann-Robertson-Walker Universe in comoving coordinates are (see e.g.

Dodelson 2003, Bertschinger 1994, Peebles 1980b)

$$\frac{\partial \delta_M}{\partial t} + \frac{1}{a}\nabla \cdot (1+\delta_M)\,\mathbf{v}_M = 0, \tag{1.7}$$

$$\frac{\partial \mathbf{v}_M}{\partial t} + \frac{\dot{a}}{a}\mathbf{v}_M + \frac{1}{a}(\mathbf{v}_M \cdot \nabla)\mathbf{v}_M = -\frac{1}{a}\nabla\phi, \tag{1.8}$$

$$\nabla^2\phi = \frac{3H_0^2\Omega_m}{2a}\delta. \tag{1.9}$$

with the subscript M that indicates matter, $\bar{\rho}_M$ the proper mean matter density that scales as $\bar{\rho}_M \propto a^{-3}$ since being a density it is defined in a volume $(a(t)^3)$), that however expands with the Universe, so it scales as the volume expands and Ω_m the cosmological matter density that is defined as (Dodelson 2003)

$$\Omega_m = \frac{\rho_{M,0}}{\rho_{crit}}$$

with $\rho_{crit} = 3H^2/8\pi G$ that is the critical density value at which the Universe would be flat (see e.g. Ryden 2017, Bertschinger 1994). Since the over-densities are small $|\delta_M| \ll 1$, we are in the linear regime, so the the continuity and Euler equations become:

$$\frac{\partial \delta_M}{\partial t} + \frac{1}{a}\nabla \cdot \mathbf{v}_M = 0, \tag{1.10}$$

$$\frac{\partial \mathbf{v}_M}{\partial t} + \frac{\dot{a}}{a}\mathbf{v}_M = -\frac{1}{a}\nabla\phi. \tag{1.11}$$

Combining the linearized continuity, Euler and Poisson equations we obtain a second order linear differential equation for the overdensity δ_M (Dodelson 2003)

$$\frac{\partial^2 \delta_M}{\partial t^2} + 2H\frac{\partial \delta_M}{\partial t} - \frac{3H_0^2\Omega_m}{2a^3}\delta_M = 0. \tag{1.12}$$

The meaning of the equation is that an over-density evolve according to a "source" term proportional to the quantity of matter, diluted by a term proportional to the Universe expansion. The general solution can be factorized and written as (Dodelson 2003)

$$\delta(\mathbf{x},t) = D_+(t)\Delta_+(\mathbf{x}) + D_-(t)\Delta_-(\mathbf{x}), \tag{1.13}$$

with $D_+(a)$ the linear growth factor. Inserting equation(1.13) into equation(1.12) we find the temporal behaviour of D_+ and D_-. In a matter dominated Universe ($\Omega_m = 1$) the two solutions are $D_+ = a$ and $D_- = a^{-3/2}$, so the latter decays with time and so the interesting solution is the growing one, that for a generic value of the density parameter it is written as (T. Padmanabhan 1995)

$$D_+(a) = \frac{5\Omega_{m,0}}{2}H(a)\int_0^a da'/(da'/dt)^3, \tag{1.14}$$

which evolves in time without changing in shape (Peebles 1980a). $\Omega_{m,0}$ is the matter density parameter evaluated at present time. Equation(1.14) is normalized such that $D_+ \to a$ as $a \to 0$ (A. J. S. Hamilton 2001). Equation(1.14) goes through two stages, at $z \gg 1$, the density parameter $\Omega_m \approx 1$, so the perturbation grows linearly. At low redshift, $\Omega_m \approx 0$, so the grow freezes out. This gives us yet another way to probe cosmological parameters: by looking at the density of objects in the universe, or the abundance of structures in the universe, if the universe is of critical density, then the number density will decline rapidly towards high-z; if it is low density, then the number density will be roughly constant and then decline towards high redshift.

In order to find the velocity field first as saw we write it in terms of a gradient of a scalar potential (A. J. S. Hamilton 1998)

$$v = \nabla\psi. \tag{1.15}$$

We use the continuity equation to relate the potential ψ to the physical matter over-density δ. The continuity equation can be wrote as (A. J. S. Hamilton 1998)

$$\nabla^2\psi = -aHf\delta. \tag{1.16}$$

where

$$f = \frac{d\ ln\ D_+}{d\ ln\ a} \tag{1.17}$$

is the dimensionless linear growth rate of the growing mode (Dodelson 2003). Equation(1.17) measures how rapidly structures in the Universe are growing as a function of cosmic time or redshift and in a ΛCDM Universe with a cosmological constant it is (A. J. S. Hamilton 1998)

$$f(\Omega_m, \Omega_\lambda) \approx \Omega_m^{0.6} + \frac{\Omega_\Lambda}{70}\left(1 + \frac{\Omega_m}{2}\right). \tag{1.18}$$

Solving this equation bring the velocity field for the matter field (Davis 1998)

$$v(\mathbf{x}, a) = \frac{faH}{4\pi}\int d^3x'\delta_M(\mathbf{x}', a)\frac{\mathbf{x}' - \mathbf{x}}{|\mathbf{x}' - \mathbf{x}|^3}, \tag{1.19}$$

In linear perturbation theory, the initial peculiar velocities are damped by the expansion of the Universe, and the peculiar velocity field is directly proportional to the gravitational acceleration due ti matter distribution around the position $\mathbf{x}$. Equation(1.19) assumes that the velocity field is determined by all the matter that is clustering, however since we are in the linear regime, it smooths all the non-linear contributions, such as the collapse and merging of galaxies at small scales (see e.g. Strauss and Willick 1995, Strauss, Yahil, et al. 1992, Bertacca 2020)

Regard that all these equations are solved for the matter, but actually we are interested in solving the linearized continuity equation for the galaxies, so we need a bias

factor that connect the galaxy distribution and the matter distribution, accounting for the fact that the galaxies form in dark matter halos, but they don't trace perfectly the underlying matter distribution of matter. The simplest bias factor at linear order is $\delta = b\delta_M$ (see e.g. Coles 1986, Demiański and Doroshkevich 1999, Cooray and R. Sheth 2002, Desjacques, Jeong, and Schmidt 2018) that assumes that the matter distribution is linearly biased by a constant factor b. We assume that the galaxies velocity faithfully follow the velocity of matter, but pay attention that this is an assumption, since in theory also the velocity could biased (Carlberg, Couchman, and Thomas 1990). Thus the un-biased velocity field for the galaxies is

$$v(\mathbf{x},a) = \frac{\beta aH}{4\pi}\int d^3x'\,\delta(\mathbf{x}',a)\frac{\mathbf{x}'-\mathbf{x}}{|\mathbf{x}'-\mathbf{x}|^3}, \tag{1.20}$$

with

$$\beta = \frac{f}{b}. \tag{1.21}$$

1.2 Redshift Space Distortions

In this and following sections, distances discussed are proper distances unless mentioned otherwise and velocities refer to the proper velocity as $d\mathbf{r}/d\tau = (aH_0)d\mathbf{r}/dt$ (A. J. S. Hamilton 1998). Modern galaxy surveys such as the "Dark Energy Survey" (Hartley et al. 2021, Sevilla-Noarbe et al. 2021) or the "Sloan Digital Sky Survey" (Margony 1999) create very accurate 3D maps of the Universe , in which each galaxy position is parameterized only by three parameters: right ascension, declination (that are the angles between the object projected position in the sky and the coordinate system used) and the distance from the observer. The firsts two are basically angles in the sky coordinates and are strongly affected by the lensing of a galaxy. This means that the the "shape" of the galaxy is altered. To infer its position one have to account for a lensing model, in order to delete its effect in the received image of the galaxy, being able to reconstruct its actual shape (Dunham et al. 2019). The distance is inferred using the Hubble law as after shown. The Universe energy is dominated by the cosmological constant, in fact around $z \approx 0.55$ it passes from a matter dominated era to the era dominated by the cosmological constant (see e.g. Velten, Marttens, and Zimdahl 2014), that makes it expands with an an accelerated motion. The acceleration felt by an object is proportional to the distance from the observer(see e.g. Garriga, Livio, and Vilenkin 1999)) and so the farthest the object the higher the recession velocity from us. The photons received are redshifted proportional to the recession velocity and so to the distance. It is possible to connect the measured redshift of the received photon with the distance of the emitting galaxy through the relation proposed by Hubble (1929). The redshift z

is the fractional change of the wavelength of the light emitted from an object due to the cosmological expansion, it is defined as (Dodelson 2003)

$$z = \frac{\lambda_0}{\lambda_e} - 1, \tag{1.22}$$

where λ_o and λe are the received and emitted wavelength. Hubble found the relation (Hubble 1929)

$$v \approx z = H_0 d. \tag{1.23}$$

with z the redshift (the term should be cz but we set $c = 1$ as said) and d the distance of an object from the observer, such that the true distance is $r = H_0 d$. Actually equation(1.23) is valid at low-z, since it is an approximation of a relativistic form that is valid at all redshift (see e.g. Carroll 2019). Assuming a cosmological model, we know the behaviour of $H(t)$ and so starting from the redshift of the photon, is possible to infer the distance of the galaxy and this method would be exact if the motion of the galaxy would be given only by the recession due to the expansion of the Universe. In reality the motion of each galaxy is given not only by the recession velocity, but also by others factors (see e.g. Anand et al. 2019). It can be affected both by the gravitational attraction from near galaxies and by the infalling of the galaxy into the potential well of the Dark matter halo in which it resides (see e.g. Lokas 2000,Karachentsev et al. 2006). These others factors give to the galaxy a peculiar velocity that is independent from the one due to the Universe expansion, since their causes are disconnected by the causes of the expansion, in fact the velocity direction due to the expansion is not the same given by the other factors (R. K. Sheth and Diaferio 2001) The position $\mathbf{s}$ in redshift space is related to the particle position in real space $\mathbf{r}$ through(A. J. S. Hamilton 1998)

$$\mathbf{s} = \mathbf{r} + \hat{\mathbf{r}} v, \tag{1.24}$$

given by the sum of the true distance plus the $\hat{\mathbf{r}}v$ term that is the projected velocity of the galaxy along the Line of Sight. The former term in the equation contains the part of the distance inferred considering the redshift due to the cosmic expansion, while the latter is the part of the redshift due to the peculiar motion. Note that $\mathbf{r}\cdot\mathbf{v}$ may be both positive, negative and null, so the value of the redshift distance could be higher, lower or equal respect to the real one, depending on the direction of the peculiar velocity of the galaxy along the Line of Sight direction:

- if $\mathbf{r}\cdot\mathbf{v}>0$ the galaxy is moving away from the observer, so it gives an "extra" redshift summed to the expansion one, so $\mathbf{s}>\mathbf{r}$ and the position in Redshift space is higher then the one in Real space;
- if $\mathbf{r}\cdot\mathbf{v}=0$ the peculiar motion is perpendicular to the Line Of Sight, so the distance due to it is zero and so the positions in Redshift and Real space are the same: $\mathbf{s}=\mathbf{r}$;

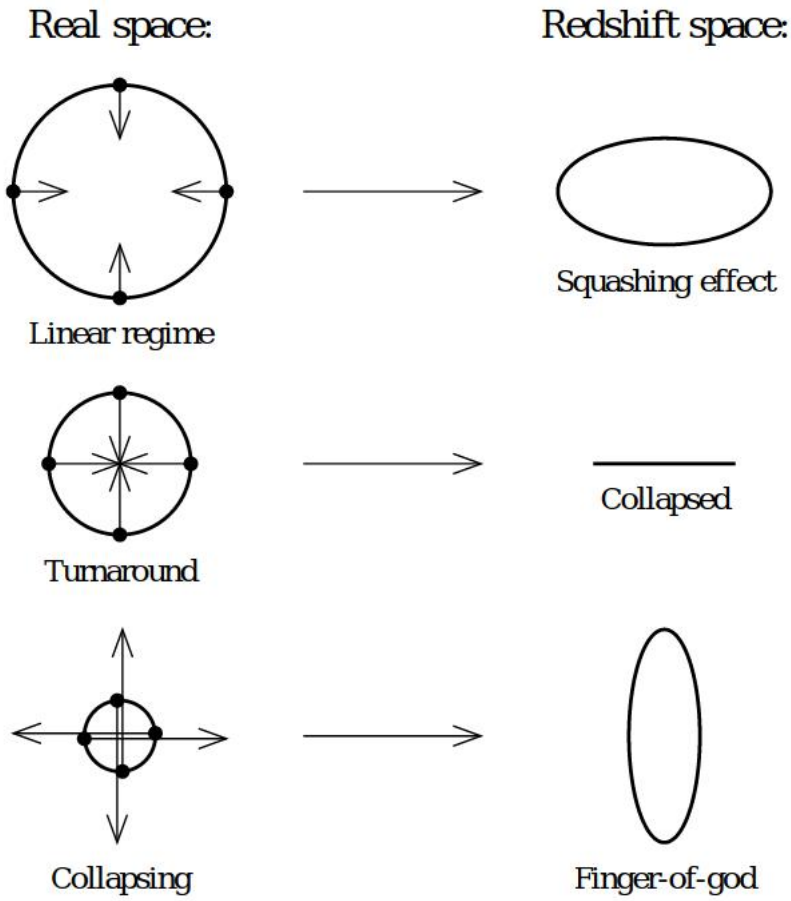

Figure 1.4: Differences of the positions measured between the Real and Redshift spaces, figure from A. J. S. Hamilton (1998).

- if $\mathbf{r}\cdot\mathbf{v}<0$ the galaxy is approaching the observer, so the measured redshift is the expansion one minus the one due to the peculiar motion, so the position in Redshift space is thus reduced: $\mathbf{s}<\mathbf{r}$.

In fig(1.4) is shown how the positions of the galaxies change between the Real space and the Redshift space, considering a spherical pattern of galaxies that are falling into the centre of the system (considering that we are observing from down):

- *First panel*: the positions of galaxies on the sides aren't modified since their movements are perpendicular to the Line of Sight. The galaxy that is receding from the observer will be measured with an higher redshift and so the inferred position would be higher, while in the opposite case, since the galaxy is approaching the observer, the redshift is less (since the peculiar velocity gives a blueshift contri-

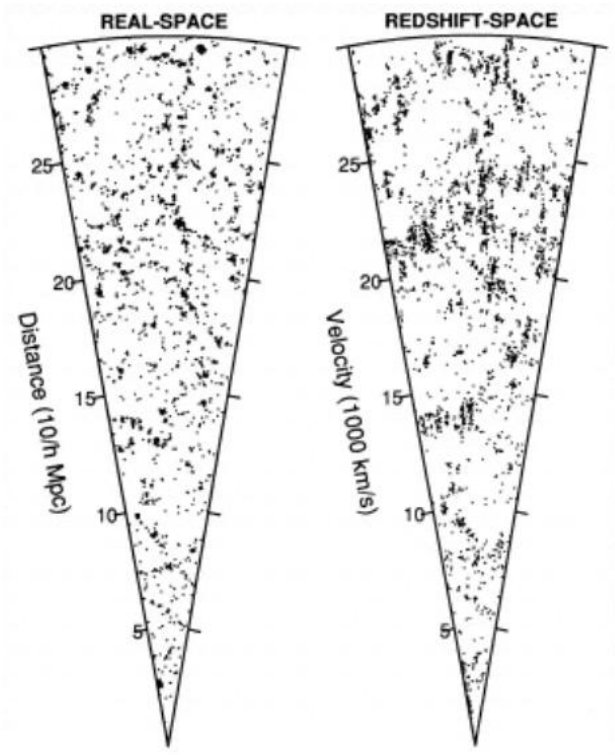

Figure 1.5: Difference between a survey in Real space and Redshift space (Figure from Praton, Melott, and McKee 1997)

bution) and so the inferred position is lower. This means that a spherical configurations in the Real space is translated into a "squashed" one in the Redshift space.

- *Middle panel*: For the galaxies on the sides hold the same argument as before, while the positive and negative contributions of $\mathbf{r}\cdot\mathbf{v}$ is exactly the same, so the in Redshift space the galaxies seems to be in the same position. This gives a straight line configuration.

- *Bottom panel*: The peculiar velocities of the galaxies on the Line of Sight when they enter the non linear regime are so strong that the nearest galaxy in Real space "acquires" so much redshift that it becomes the farest in Redshift space and viceversa for the other galaxy. So a spherical pattern in Real space assumes the classical "Finger of God" pattern in Redshift space.

In fig.(1.3) is shown how a galaxy survey changes if the galaxies positions are inferred in the Real or Redshift space, according with how just explained. In the Redshift one

the Finger of God and the squashed pattern are very visible.

In reality the peculiar motion is not the only effect that could alter the observed redshift of the received photons and consequently the inferred position of the galaxies in the two spaces. Can be shown that when the size of a survey is large enough there are some Relativistic effect that have be taken into account. For example Doppler effect, Shapiro time delay and Sachs-Wolfe effect alter the measured redshift as well, while the magnification effect alter the number of counts of the galaxies into the survey. These effects will be discussed in detail in the next chapter, while in the next section we introduce the Real and the Redshift spaces.

1.3 Real space and Redshift space

In this section we define what the Real and Redshift spaces are, defining also the power spectrum in the two spaces, following (A. J. S. Hamilton 1998, Linder 2005, Nandi 2017b, Okumura et al. 2015)

We begin introducing a theoretical quantity that is the true density field of the universe. Let $\rho(\mathbf{r})$ be the matter density of the universe at the real (true) position indicated with $\mathbf{r}$ and $\bar{\rho}$ the constant mean density. We define the matter contrast at each single position $\mathbf{r}$ as (A. J. S. Hamilton 1998)

$$\delta(\mathbf{r}) = \frac{\rho(\mathbf{r}) - \bar{\rho}}{\bar{\rho}}. \tag{1.25}$$

Measuring this quantity in all the positions $\mathbf{r}$ would means to measure the behaviour of the over and under densities in the Universe, namely understanding its properties. In a survey we are not able to observer at the same time the whole Universe, so what we do is to try to infer its properties observing only a portion of it. The observed galaxies are thus considered as a statistical sample randomly drawn from a *true* underlying theoretical population, thus using the observed to infer the properties of the true population.
The statistic to study the over-densities is the 2 Point Correlation Function (2PCF) and its Fourier transformation that is the Power Spectrum. The 2PCF called also correlation function is the expectation value of the product of the over-densities of a pair of randomly positioned points at $\mathbf{r}_1$ and $\mathbf{r}_2$ respectively separated by $r_{12} = |\mathbf{r}_1 - \mathbf{r}_2|$ (A. J. S. Hamilton 1998)

$$\xi(r_{12}) = \langle \delta(\mathbf{r}_1)\delta(\mathbf{r}_2) \rangle. \tag{1.26}$$

The fact that the 2PCF depends only on the separation between the two points and not on their orientation is a direct consequence of the isotropy of the universe. The Fourier transform of the over-density and its inverse Fourier transform are defined as (Sefusatti et al. 2016)

$$\hat{\delta}(\mathbf{k}) \equiv \int e^{i\mathbf{k}\cdot\mathbf{r}} \delta(\mathbf{r}) d^3r, \quad \delta(\mathbf{r}) = \int e^{-i\mathbf{k}\cdot\mathbf{r}} \hat{\delta}(\mathbf{k}) d^3k/(2\pi)^3. \tag{1.27}$$

The Power Spectrum is defined as the covariance of the Fourier modes and so simply the Fourier transform of the correlation function (A. J. S. Hamilton 1998)

$$\left\langle \hat{\delta}\left(\mathbf{k}_1\right)\hat{\delta}\left(\mathbf{k}_2\right)\right\rangle = \int e^{i\mathbf{k}_1\cdot\mathbf{r}_1+i\mathbf{k}_2\cdot\mathbf{r}_2}\xi\left(r_{12}\right)d^3r_1d^3r_2, \tag{1.28}$$

and since the correlation function is written in function only of the separation, it becomes:

$$\left\langle \hat{\delta}\left(\mathbf{k}_1\right)\hat{\delta}\left(\mathbf{k}_2\right)\right\rangle = (2\pi)^3\delta_D\left(\mathbf{k}_1+\mathbf{k}_2\right)P\left(k_1\right), \tag{1.29}$$

where the Dirac Delta function contains the assumption of translation invariance due to the homogeneity of space, while the isotropy assumption make the power spectrum depends on the modulus of the modes $|\mathbf{k}|$ and not on its orientation. P(k) is the Power Spectrum:

$$P(k) \equiv \int e^{i\mathbf{k}\cdot\mathbf{r}_\xi}\xi(r)d^3r, \quad \xi(r) = \int e^{-i\mathbf{k}\cdot\mathbf{r}}P(k)d^3k/(2\pi)^3. \tag{1.30}$$

As said these quantities are related to the *theoretical* density field expressed in equation (1.25), but the actual surveys scan only a part of the sky and so only a portion of the density field of the Universe, giving only a "restricted" representation of this field. Obviously the bigger the survey the nearest the statistical sample can reproduce the theoretical properties. Each survey is characterized by a selection function $\bar{n}(\mathbf{r})$ (A. J. S. Hamilton 1998) which is the expected mean number of galaxies at position $\mathbf{r}$ given a selection criteria (e.g. selection on the flux, on distance...). The main hypothesis is that the observed galaxies form a Poisson process on the underlying population with the selection function specifying the probability of including a galaxy at position $\mathbf{r}$ into the survey. Let $n(\mathbf{r})$ denote the number density of galaxies at position $\mathbf{r}$ in a survey, thus the observed galaxy contrast is defined as (A. J. S. Hamilton 1998)

$$\delta_{\rm obs}(\mathbf{r}) \equiv \frac{n(\mathbf{r})-\bar{n}(\mathbf{r})}{\bar{n}(\mathbf{r})}. \tag{1.31}$$

Being this process Poissonian the expectation value $C\left(r_1,r_2\right)$ of the Covariance of the observed over-densities is a sum of the true correlation function $\xi\left(r_{12}\right)$ with a Poisson sampling noise, or shot noise, term (A. J. S. Hamilton 1998)

$$\left\langle \delta_{\rm obs}\left(\mathbf{r}_1\right)\delta_{\rm obs}\left(\mathbf{r}_2\right)\right\rangle \equiv C\left(\mathbf{r}_1,\mathbf{r}_2\right) = \xi\left(r_{12}\right)+\delta_D\left(\mathbf{r}_1-\mathbf{r}_2\right)\left[\bar{n}\left(\mathbf{r}_1\right)\right]^{-1}. \tag{1.32}$$

Thus any average $\left\langle \delta_{\rm obs}\left(\mathbf{r}_1\right)\delta_{\rm obs}\left(\mathbf{r}_2\right)\right\rangle$ of products of pairs of over-densities at any finite separation $r_{12} \equiv |\mathbf{r}_1-\mathbf{r}_2| \neq 0$, provides an unbiased estimate of the true correlation function $\xi\left(r_{12}\right)$. Note that the higher the selection function, the lower the shot noise ($1/\bar{n}(\mathbf{r}_1) \to 0$), this means that the more galaxies are observed in a survey, the more the *observed* density field approaches the *theoretical* one.

With the same spirit we can define in the Redshift space the Redshift space correlation function as

$$\xi^s(s_{12}, s_1, s_2) \equiv \langle \delta^s(\mathbf{s}_1)\, \delta^s(\mathbf{s}_2) \rangle, \tag{1.33}$$

that is the ensemble average of the over-densities measured at redshifts $\mathbf{s}_1$ and $\mathbf{s}_2$. Note that since the redshift is for definition measured along a Line Of Sight, this partially destroy the translation symmetry, preserving the rotational one, so the correlation function depends also on the separation $s_{12} = |s_1 - s_2|$. Suppose that the angle between the two galaxy positions s_1 and s_2 is small enough, the Redshift distortions are plane-parallel and thus the the correlation function is written in terms of the parallel and perpendicular part of the Redhsift

$$\xi^s(s_{12}, s_1, s_2) \approx \xi^s\left(s_{//}, s_\perp\right). \tag{1.34}$$

with $s_{//}$ and $s_\perp$ the part of the redshift respectively parallel and perpendicular to the Line Of Sight The Fourier transform of the true Redshift space over-density defines the redshift Fourier modes

$$\hat{\delta}^s(\mathbf{k}) \equiv \int e^{i\mathbf{k}\cdot\mathbf{s}^s}(\mathbf{s}) d^3s, \quad \delta^s(\mathbf{s}) = \int e^{-i\mathbf{k}\cdot\mathbf{s}} \hat{\delta}^s(\mathbf{k}) d^3k/(2\pi)^3. \tag{1.35}$$

The Covariance of the redshift Fourier modes defines the Redshift space power spectrum, which is equal to the Fourier transform of the redshift correlation function

$$\left\langle \hat{\delta}^s(\mathbf{k}_1)\, \hat{\delta}^s(\mathbf{k}_2) \right\rangle = \int e^{i\mathbf{k}_1\cdot\mathbf{s}_1 + i\mathbf{k}_2\cdot\mathbf{s}_2} \xi^s(s_{12}, s_1, s_2)\, d^3s_1 d^3s_2. \tag{1.36}$$

As said in Redshift space there is not statistical homogeneity (thus translation symmetry) and so the redshift Power Spectrum is no longer a diagonal matrix. The residual rotational symmetry around the observer that is still preserved implies that the redshift power spectrum is a function only of the modulus of the combinations of the various modes (and not on their orientation):

$$\left\langle \hat{\delta}^s(\mathbf{k}_1)\, \hat{\delta}^s(\mathbf{k}_2) \right\rangle = \hat{\xi}^s(|\mathbf{k}_1 + \mathbf{k}_2|, k_1, k_2). \tag{1.37}$$

As before if we apply the plane-parallel approximation we recover the statistical homogeneity, and in this case the redshift Power Spectrum is again a diagonal matrix:

$$\left\langle \hat{\delta}^s(\mathbf{k}_1)\, \hat{\delta}^s(\mathbf{k}_2) \right\rangle \approx (2\pi)^3 \delta_D(\mathbf{k}_1 + \mathbf{k}_2) P^s\left(k_{1//}, k_{1\perp}\right), \tag{1.38}$$

where $k_{1//}$ and $k_{1\perp}$ are the components of the wavevector $\mathbf{k}_1$ respectively parallel and perpendicular to the Line Of Sight, and

$$P^s\left(k_{//}, k_\perp\right) \equiv \int e^{i\mathbf{k}\cdot\mathbf{s}^s} \xi^s\left(s_{//}, s_\perp\right) d^3s. \tag{1.39}$$

Remind that this discussion is for the underlying theoretical field in redshift space. The observational density contrast field from a survey is given by

$$\delta^s_{obs}(\mathbf{s}) = \frac{n^s(\mathbf{s}) - \bar{n}(\mathbf{s})}{\bar{n}(\mathbf{s})}, \tag{1.40}$$

with $n^s(\mathbf{s})$ the observed number density of galaxies at redshift position $\mathbf{s}$ and $\bar{n}^s(\mathbf{s})$ the redshift space selection function. As for for the real space the actual observed quantities don't match perfectly the theoretical one, and so assuming that a survey is a Poisson process the expectation value $C^{ss}(s_1, s_2)$ of the Covariance of observed Redshift space over-densities $\delta^{ss}_{\text{obs}}(s)$ defined by (3.18) is a sum of the corresponding true Redshift space Correlation function $\xi^{ss}(s_{12}, s_1, s_2)$, equation (4.83), with a Poisson sampling noise term

$$\left\langle \delta^{ss}_{\text{obs}}(\mathbf{s}_1)\, \delta^{ss}_{\text{obs}}(\mathbf{s}_2) \right\rangle \equiv C^{ss}(\mathbf{s}_1, \mathbf{s}_2) = \xi^{ss}(s_{12}, s_1, s_2) + \delta_D(\mathbf{s}_1 - \mathbf{s}_2) \frac{\bar{n}(\mathbf{s}_1)}{\left[\bar{n}^s(\mathbf{s}_1)\right]^2}. \tag{1.41}$$

Again, the coefficient $\bar{n}(s_1) / \left[\bar{n}^s(s_1)\right]^2$ of the Poisson sampling term is valid for a flux-limited redshift survey.

1.4 Linear Redshift Distortion Operator

In the previous sections we introduced the Real and the Redshift space, now we show how these spaces are connected, introducing the Linear Redshift Distortion Operator $\mathbf{S}$ that contains the information of how the galaxies positions are displaced due to the Redshift Space Distortions. It connects the over-densities observed in the Redshift space with those observed in the Real, so it is written as (A. J. S. Hamilton 1998)

$$\delta^s = \mathbf{S}\delta, \tag{1.42}$$

with δ^s and δ the over-densities respectively in the Redshift and Real space. To derive the Linear Redshift Distortion operator we begin from the conservation equation of galaxies, that is based on the fact that in Redshift space the positions of the galaxies are displaced, but the actual number of galaxies has to be the same of that one in the Real space, since galaxies can't appear or disappear, so the number density is conserved:

$$n^s(\mathbf{s}) d^3 s = n(\mathbf{r}) d^3 r. \tag{1.43}$$

We write this expression in terms of the over-densities

$$\bar{n}(\mathbf{s})\left[1 + \delta^s(\mathbf{s})\right] s^2 ds = \bar{n}(\mathbf{r})[1 + \delta(\mathbf{r})] r^2 dr, \tag{1.44}$$

and using the expression that connects the position in the Redshift space with the one in the Real space

$$\mathbf{s} = \mathbf{r} + \hat{\mathbf{r}} v, \tag{1.45}$$

It becomes:

$$1 + \delta^s(\mathbf{s}) = \frac{r^2 \bar{n}(\mathbf{r})}{(r+v)^2 \bar{n}(\mathbf{r} + v\hat{\mathbf{r}})} \left(1 + \frac{\partial v}{\partial r}\right)^{-1} [1 + \delta(\mathbf{r})]. \tag{1.46}$$

Now we do two assumptions:

- We are interested in the linear regime, so the perturbation (so the over-densities) are small: $|\delta(\mathbf{r})| \ll 1$, which implies also that $|\partial v/\partial r| \ll 1$
- We assume that the peculiar velocities of the galaxies are very small compared to the distance from the observer: $|v| \ll r$

So at linear order equation (1.46) becomes:

$$\delta^s(\mathbf{r}) = \delta(\mathbf{r}) - \left(\frac{\partial}{\partial r} + \frac{\alpha(\mathbf{r})}{r}\right) v, \tag{1.47}$$

with

$$\alpha(\mathbf{r}) \equiv \frac{\partial \ln r^2 \bar{n}(\mathbf{r})}{\partial \ln r}$$

In equation (1.20) we have derived an expression for the velocity in the linear theory, and so putting this result into equation (1.47) it yields the final Linear Redshift Distortion Operator:

$$\delta^s(\mathbf{r}) = \delta(\mathbf{r}) + \beta \left(\frac{\partial^2}{\partial^2 r} + \frac{\alpha(\mathbf{r})}{r} \frac{\partial}{\partial r}\right) \nabla^{-2} \delta. \tag{1.48}$$

The Redshift Space Distortion operator since introduce a Line Of Sight destroys translation symmetry, so that Fourier modes are no longer eigenmodes of the distortion operator, and the redshift space power spectrum isn't a diagonal matrix. The radial redshift distortion operator does however preserve angular symmetry about the observer (A. J. S. Hamilton 1998), in fact the distortion operator $\mathbf{S}$ commutes with the angular momentum operator $\mathbf{L}$, so that the eigenmodes of the angular momentum operator, which are the spherical harmonics Y_{lm}, are also eigenmodes of the distortion operator. In next section we introduce the plane parallel approximation, in which the plane-parallel distortion operator is diagonal in Fourier space, which is intimately associated with the fact that plane-parallel redshift distortions preserve translation invariance.

1.4.1 Linear Plane-Parallel Redshift Distortion Operator

In the previous section we showed the derivation of the Linear Redshift Distortion Operator that allows to connect the galaxy positions in Real space with the ones in Redhsift space. Nowadays instead of the expression in equation (1.48) is commonly used the Plane-Parallel approximation (called also "distant observer") that is based on the assumption that the galaxies observed are very far from the observer, that is $r \gg 1$ and so galaxies move along only one Line Of Sight since the separation angle is $\theta = 0$. The second term in equation (1.48) goes to zero, so we ends up with

$$\mathbf{S}^p = 1 + \beta \frac{\partial^2}{\partial z_{LOS}^2} \nabla^{-2}, \tag{1.49}$$

with z the distance along the Line Of Sight (we use the subscription $_{LOS}$ to clarify that this is a quantity computed along the Line Of Sight and is not the redshift). In Fourier space we have:

$$(\partial/\partial z_{LOS})^2 \nabla^{-2} = k_{z,LOS}^2/k^2 = \mu_{\mathbf{k}}^2, \tag{1.50}$$

with $\mu_{\mathbf{k}} = \hat{\mathbf{z}_{LOS}} \cdot \hat{\mathbf{k}}$ the cosine of the angle between the wavevector $\mathbf{k}$ and the Line Of Sight $\mathbf{z}_{LOS}$. So the Linear Redshift Distortion operator in the Plane-Parallel approximation becomes:

$$\mathbf{S}^p = 1 + \beta \mu_{\mathbf{k}}^2, \tag{1.51}$$

and so writing it with the over-densities in Redshift and Real space

$$\hat{\delta}^s(\mathbf{k}) = \left(1 + \beta \mu_{\mathbf{k}}^2\right) \hat{\delta}(\mathbf{k}), \tag{1.52}$$

we can recover the relation between the Power Spectra:

$$P^s(\mathbf{k}) = \left(1 + \beta \mu_{\mathbf{k}}^2\right)^2 P(k). \tag{1.53}$$

This equation has a very simple meaning, it states that the Power Spectrum computed in Redshift space is simply equal to the one in real space, amplified by a term $\left(1 + \beta \mu_k^2\right)^2$. This results was first obtained by (Kaiser 1987). In fig.(1.6) there is a simple "visual" explanation for this effect: the over-densities along the Line Of Sight are parametrized by a wave of amplitude $\delta(\mathbf{k})$ in Real space (thin line) and in Redshift space (thick line). The peculiar velocities (indicated with the arrows) make the amplitude in Redshift space enhanced by a factor $(1 + \beta)$ if the wavevector $\mathbf{k}$ is along the line of sight, or by $(1 + \beta \mu_{\mathbf{k}}^2)$ if the wavevector form a general angle. In figure (1.7) is shown the comparison between the predicted power spectrum for a full sky configuration limited to the redshift $z = (1.5, 1.8)$ in Real space and with the relative Kaiser prediction. The

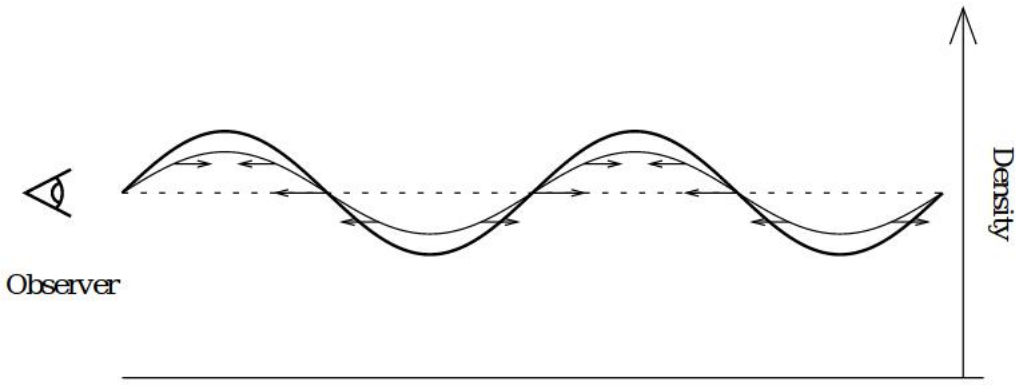

Figure 1.6: Visualization of how the over-densities change between the Redshift and real space. (Figure from A. J. S. Hamilton 1998)

Real Space power spectrum is obtained by correcting the linear power spectrum for the time evolution within the light-cone as in (Yamamoto, Nishioka, and Suto 1999),

$$P_{LC} = \left[\frac{\int_{z_i} z^f b^2 \bar{n}_g^2 D_+^2 \frac{dV_s}{dz} dz}{\int_{z_i} z^f \bar{n}_g^2 \frac{dV_s}{dz} dz} \right] P_{Lin}(k), \tag{1.54}$$

with $P_{lin}(k)$ the matter power spectrum at $z = 0$, D_+^2 the linear growth factor normalised to one at present time and V_s the comoving volume within the past light-cone of the observer, everything computed assuming the cosmology in Table(4.1).The kaiser prediction is instead obtained as just showed with equation(1.7). It's very visible that the power spectrum in the Redshift space is similar to the one in Real space, only with an enhanced amplitude.

1.5 Wide angle Redshift Space Distortions

The plane-parallel analysis describes sufficiently well galaxy surveys where the number of pairs with large angular separation is small (i.e the θ angle between the two galaxies is very small for most of the pairs). However, this approximation could be valid in the past, but the situation is going to be different for current and future wide-angle galaxy surveys such as DESI (DESI Collaboration et al. 2016), SPHEREx (Doré et al. 2014), Euclid (R. Scaramella et al. 2022) and SKA (Weltman et al. 2020) since they will have a better sky coverage and probe larger and wider scales (for example the sky coverage of Euclid is roughly $\approx$ 15000 square degrees). When we drop the plane-parallel approximation we lose the translation symmetry about the observer; this happens because if we introduce an observer and we adopt the most realistic description

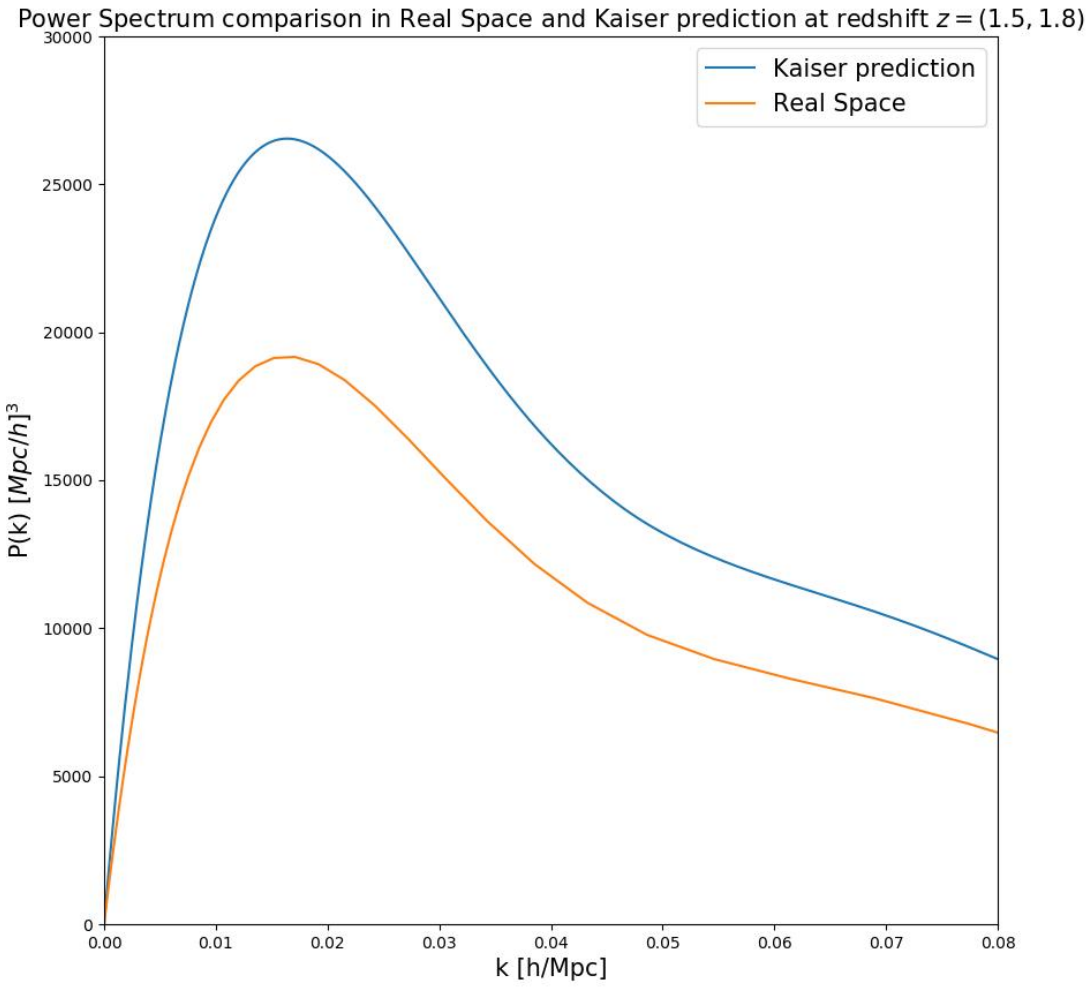

Figure 1.7: Comparison between the predicted power spectrum in Real space and with kaiser formula for a full sky survey with $z = (1.5, 1.8)$. The Real Space power spectrum is computed with equation(1.54) assuming the cosmology in table(4.1), while the power spectrum in Redshift space is computed with equation(1.7) with same cosmology.

of $\theta \neq 0$, galaxies do not move along parallel, radial, lines, but they will move as in figure(1.8) (Castorina and M. White 2020). In figure(1.8) is shown the plane parallel case on the left, where the galaxies passing from Real to Redshift Space move along only one Line Of Sight, giving rise to the common pattern described in section(1.2), while on the right is shown the wide angle case, where now there are various Line Of Sight directions and each galaxy moves along one giving rise to the so called "Pancacke of God".

Wide-angle effects can be subdivided in “purely wide-angle” and “mode-coupling” terms: “purely wide-angle” effects correct plane-parallel predictions accounting for the fact that the separation angle is non-zero (see e.g. Beutler, Castorina, and Zhang 2019), “mode-coupling” terms in addition account for the fact that galaxy pairs coherently move in a way that is dependent on sample density (see e.g. Raccanelli, Bertacca, Jeong, et al. 2016). The wide-angle distortion operator turns out to have a more complicated expression than the plane parallel one (Raccanelli, Bertacca, Jeong, et al. 2016). This happens because without translation symmetry, Fourier modes are no longer eigenmodes of the redshift distortion operator, and thus the redshift space power spectrum $\langle \delta_s(k_1)\delta(k_2)\rangle$ is no longer a diagonal matrix. In the Kaiser formula it is used a single Fourier mode approximation; this is correct in the plane parallel case, where modes are independent, but it is not in the wide-angle case (Kaiser 1987). The fact that the power spectrum is no longer a diagonal matrix means that different modes are “mixed”, and so this assumption is not anymore valid. The wide-angle redshift distortion operator does however preserve angular symmetry about the observer (see e.g. Castorina and M. White 2018). This because the distortion operator $\mathbf{S}$ commutes with the angular momentum operator $\mathbf{L}$ (that is defined as $\mathbf{L} = i\mathbf{r} \times \partial/\partial\mathbf{r} = i\mathbf{k} \times \partial/\partial\mathbf{k}$, that is the same in Real or Fourier spaces as showed in A. J. S. Hamilton (1998), so that the spherical harmonics Y_{lm}, that are the eigenmodes of the angular momentum operator, are also eigenmodes of the distortion operator (A. J. S. Hamilton 1998). For this reason, spherical harmonics modes remain statistically orthogonal with respect to the angular indices in redshift space (see e.g. Yoo and Seljak 2014). Spherical harmonics are special functions defined on the surface of a sphere and they form a complete set of orthogonal functions and thus an orthonormal basis, each function defined on the surface of a sphere can be written as a sum of these spherical harmonics. This is similar to periodic functions defined on a circle that can be expressed as a sum of circular functions (sines and cosines) via Fourier series (Altmann, Bradley, and Hume-Rothery 1963). The over-density δ using spherical harmonics is defined as (A. J. S. Hamilton 1998)

$$\delta_{lm}(r) = \int Y_{lm}(\hat{\mathbf{r}})\delta(\mathbf{r})do_{\mathbf{r}}, \qquad \delta(\mathbf{r}) = \sum_{lm} Y^*_{lm}(\hat{\mathbf{r}})\delta_{lm}(r), \tag{1.55}$$

and its counterpart in Fourier space

$$Y_{lm}(\hat{\mathbf{k}})\delta(\mathbf{k})do_{\mathbf{r}}, \qquad \delta(\mathbf{k}) = \sum_{lm} Y^*_{lm}(\hat{\mathbf{k}})\delta_{lm}(k), \tag{1.56}$$

with $do_{\mathbf{r}}$ and $do_{\mathbf{r}}$ that denotes an interval of solid angle in Real and Fourier space and Y_{lm} the tabulated spherical harmonics. The wide-angle redshift distortion operator is not Hermitian, unlike the plane-parallel one, so not all the eigenvalues of its eigenfunctions are real; this means that redshift distortions cause a phase shift to some modes when passing from the real to the redshift space, and so generating the "mode-coupling" terms (A. J. S. Hamilton 1998).

When we derived the Linear Redshift Distortion operator in section(1.4), we obtained equation(1.46) that can be rewritten as (Raccanelli, Bertacca, Jeong, et al. 2016)

$$1+\delta^s(\mathbf{s}) = \frac{\bar{n}(\mathbf{r})}{\bar{n}(\mathbf{r}+v\hat{\mathbf{r}})}\left(1+\frac{\partial v}{\partial r}\right)^{-1}\left(1+\frac{v_r}{r}\right)^{-2}[1+\delta(\mathbf{r})], \tag{1.57}$$

with $v_r = \hat{\mathbf{r}}\cdot v/(aH)$ that is the radial component of the peculiar velocity normalized with the Hubble parameter. Working in the linear regime the term $(1+v/r)^{-2}$ is proportional to v/r and assuming the plane parallel approximation as in section(1.4.1) this terms is negligible since at large distance $v/r \ll 1$. Is important to underlying that in this approximation this term being very small is negligible, but it is not completely null. In the wide angle computation the $(1+v/r)^{-2}$ (that we call "Doppler term") can't be neglected and its presence can alter the power spectrum, especially at small redshift (see e.g. 2.2)(Raccanelli, Samushia, and Percival 2010,Pápai and Szapudi 2008,Raccanelli, Bertacca, Jeong, et al. 2016). It is very important to underlying that in the computation of the Redshift Space Distortions made in the previous chapters, we did the assumption of working in the linear regime (where all the calculation are simpler) and in the flat-sky approximation. This allowed us to write the power spectrum in redshift space in function of the power spectrum in real space, through the proportionality term $(\beta\mu_{\mathbf{k}}^2)$. If we instead adopt the more realistic prescription that the Doppler term is not negligible in a general relativistic contest, the things change. Now we are not able to write the power spectrum in redshift space in function of the power spectrum in real space, since as just said we lose translation symmetry and the Fourier modes are no longer eingemodes of the redshift space distortion operator and so the redshift space power spetcrum isn't a diagonal matrix, as it is in the flat-sky case. In this case, with all the relativistic corrections the $\alpha(z)$ term is expressed as in Bertacca et al. (2012)

$$\alpha(z) = -\chi(z)\frac{H(z)}{(1+z)}\left[b_e(z)-1-2\mathscr{Q}(z)+\frac{3}{2}\Omega_m(z)-\frac{2}{\chi(z)}[1-\mathscr{Q}(z)]\frac{(1+z)}{H(z)}\right], \tag{1.58}$$

Note that now the distance that enter in the α term is χ, that is the comoving one expressed in equation(1.4), so now we are mapping from the observed coordinates, rather than the real one as before. Note that in a general relativistic context we can't implement a flat-sky approximation as in the previous section, since even for $\chi \gg 1$ the $\alpha(z)$ term becomes not negligible, so in this case the flat-sky approximation is infeasible. As showed in Raccanelli, Bertacca, Jeong, et al. (2016) the Redshift Space Distortion

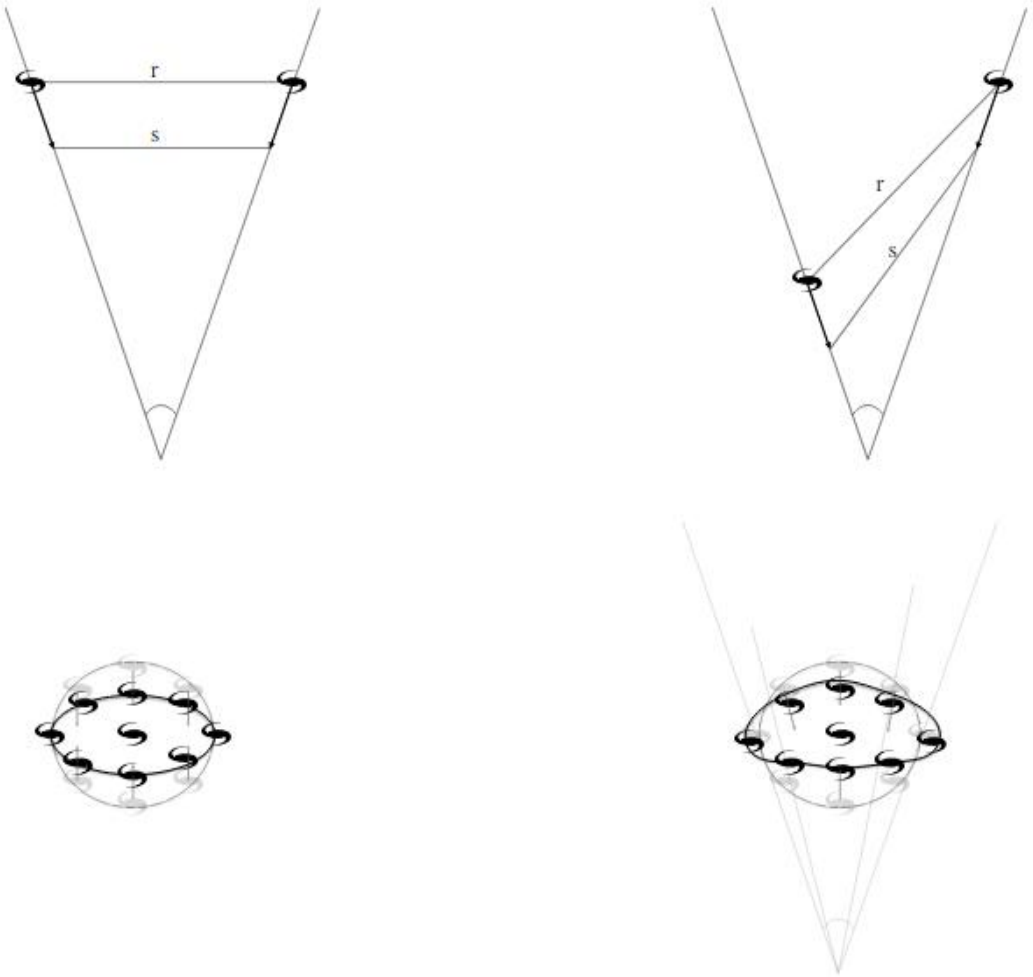

Figure 1.8: *Left:* How galaxies moves from Redshift to Real Space adopting the plane parallel approximation, giving rise to the "Pancake" of God shape. *Right*: How the situation change adopting the wide angle formalism, now the galaxies moves along different Line of Sight, giving rise to the "Croissant" of God shape.(Figure from Raccanelli, Bertacca, Jeong, et al. 2016)

operator can be written as

$$\mathbf{S} = \mathbf{S}^{kaiser} + \mathbf{W}_\alpha, \tag{1.59}$$

with $\mathbf{S}^{kaiser}$ the standard operator in the flat-sky approximation, plus

$$\mathbf{W}_\alpha = \alpha \frac{\beta\mu}{k\chi}, \tag{1.60}$$

with χ the comoving distance and μ the cosine of the angle Φ as in figure(1.9). $\mathbf{W}_\alpha$ is an operator that accounts for the wide angle corrections, with $\alpha(z)$ that in this case is written as (Raccanelli, Bertacca, Jeong, et al. 2016) where the magnification bias paramater for a magnitude-limited survey is

$$\mathscr{Q} = -\left.\frac{d\ln\bar{n}_{\rm g}}{d\ln L}\right|_{L=L_{\rm lim}},$$

and

$$b_e(z) = -(1+z)\left.\frac{\partial \ln[n_g(1+z)^{-3}]}{\partial z}\right|_{L=\text{const.}}.$$

(Note that this definition is the same of equation(2.60 only written make explicit the redshift dependence, for details on these parameters see section(3.3). Note that the presence of k in equation(1.60) is directly connected to the "mode coupling" explained before. The operator in equation(1.60) contains the doppler term, so the Redshift Space power spectrum is (Raccanelli, Bertacca, Jeong, et al. 2016)

$$P^s(k,\mu) = \left[(1+\beta\mu^2)^2 + \left(\alpha\frac{\beta\mu}{k\chi}\right)^2\right] P^r(k), \tag{1.61}$$

that the first term is the usual term from the Kaier approximation (Kaiser 1987), plus a "correction" due to the doppler term. Note that also here we are mapping in the observed coordinates. In figure(1.10) and figure(1.11) are shown the angular averaged power spectra using the flat-sky approximation and adding the $\mathbf{W}$ operator in the wide angle case at different redshift $z = 0.1$ and $z = 1$ and for various values of the non-gaussianity parameter f_{NL}, we will discuss this parameter in section(2.1), so in the figures we analyze only the $f_{NL} = 0$ case. In the figures is clear that adding the doppler term the power spectrum acquires power at large scale, especially for survey at low redshift. This is totally expected, because the lower is the redshift, the higher is the v/r term. As showed in equation(1.61) the Doppler term introduces an additive term in the power spectrum so we expect that the power spectrum including wide angle effect will be over-powered with respect to the one in flat sky.

Signature of wide angle effects can be seen also in the correlation function (Raccanelli, Bertacca, Jeong, et al. 2016) as shown in figure(1.12), where are plotted the 2D

redshift space galaxy correlation function, comparing the correlation function including the doppler term (with the subscript $_{WA}$) and the one in the flat-sky approximation (with the suscript $_{FS}$) for redshift $z = 0.1$ (top) and $z = 1$ (bottom). $r_{//}$ and $r_{\perp}$ are the parallel and perpendicular component of the galaxy pair distance (remind that we are using the observed distance not the proper). The colored contours indicate the correlation accounting for the doppler term, black lines instead the correlation excluding it. Black lines overlapping with borders between different colored contours indicates that the effect of including the Doppler term is negligible, since this means that the amount of correlation between the two cases is the same. At high redshift this happens in both the plane-parallel (as expected) and wide-angle cases (bottom panels), since in this case the term v/r is small and so $(1 + v/r)^{-2} \to 1$ (also here hold the previous comments on which distance we are adopting). At low-z, in the plane-parallel approximation, the lines overlap meaning that the doppler term is negligible. However, the top right panel shows how the wide-angle in the low-z case is not negligible, since the black lines and colored contour are not overlapping, meaning that at low-z the correlation function strongly depends on if the wide angle effects are considered or not.

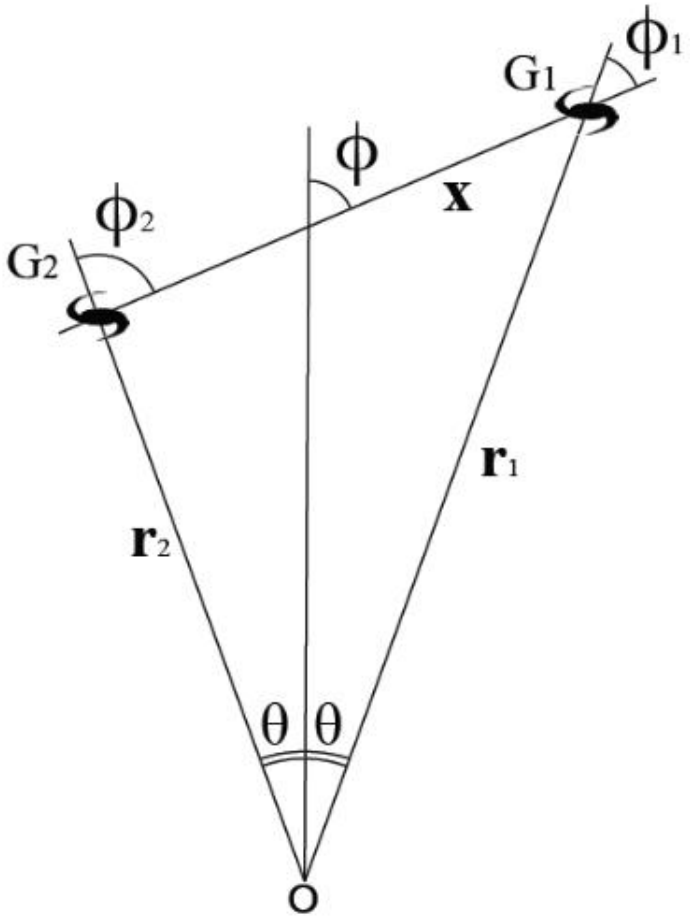

Figure 1.9: Position of galaxies in the wide angle formalism. here each galaxy has its own Line Of Sight through it is projected, and so now the θ angle is the observational angle, while ϕ is the angle between the galaxies separation directiona and the Line of Sight (Figure from Raccanelli, Samushia, and Percival 2010)

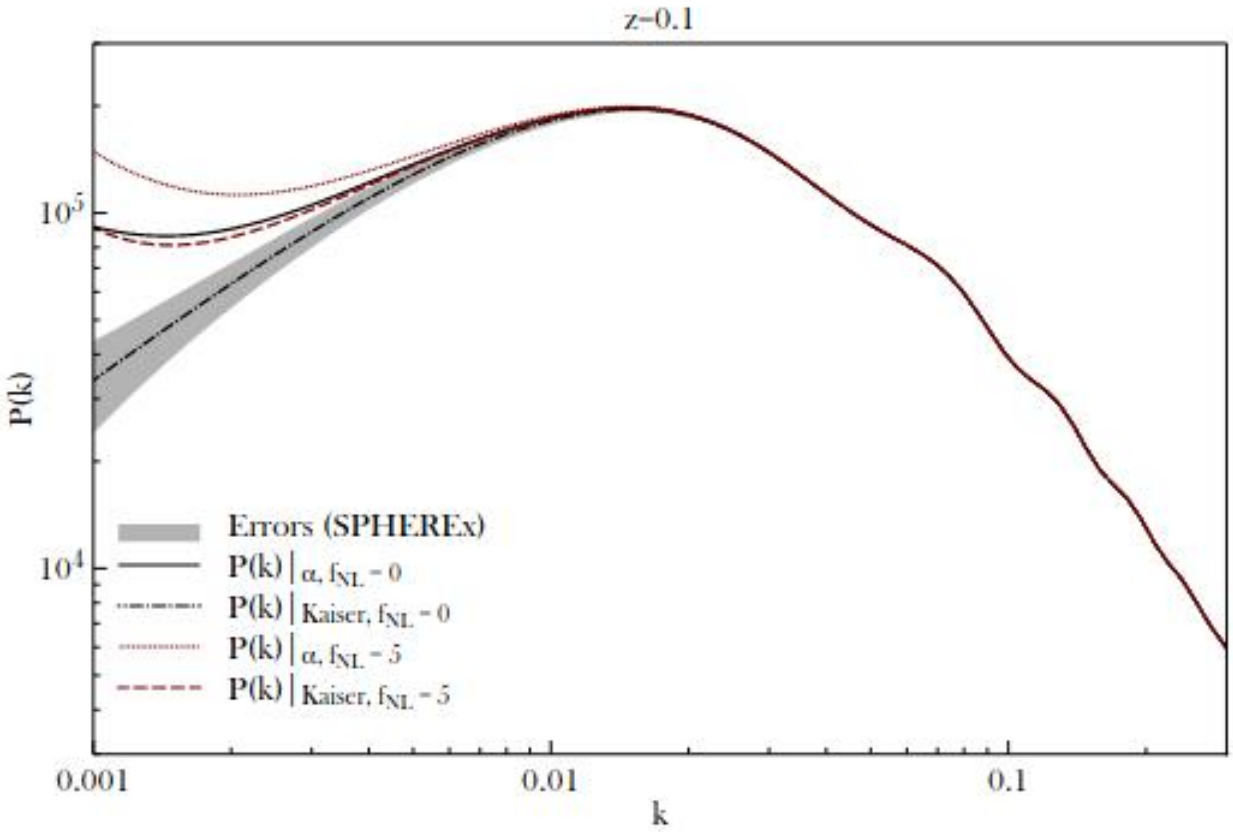

Figure 1.10: The angle averaged power spectra for $z = 0.1$ computed in the flat-sky approximation (solid black line) with $f_{NL} = 0$ (for a detailed discussion on f_{NL} see section(2.1)), accounting for wide angle effect, that is the Doppler term (dotted black) with $f_{NL} = 0$, in the flat-sky approximation (solid black line) with $f_{NL} = 5$ and accounting for wide angle effect, that is the Doppler term (dotted black) with $f_{NL} = 5$ (Figure from Raccanelli, Bertacca, Jeong, et al. 2016). For comparison are showed the expected error obtained with the SPHEREx (Spectro-Photometer for the History of the Universe, Epoch of Reionization and Ices Explorer), that is a mission that will scan the whole sky. SPHEREx will survey hundreds of millions of galaxies near and far, some so distant their light has taken 10 billion years to reach Earth.

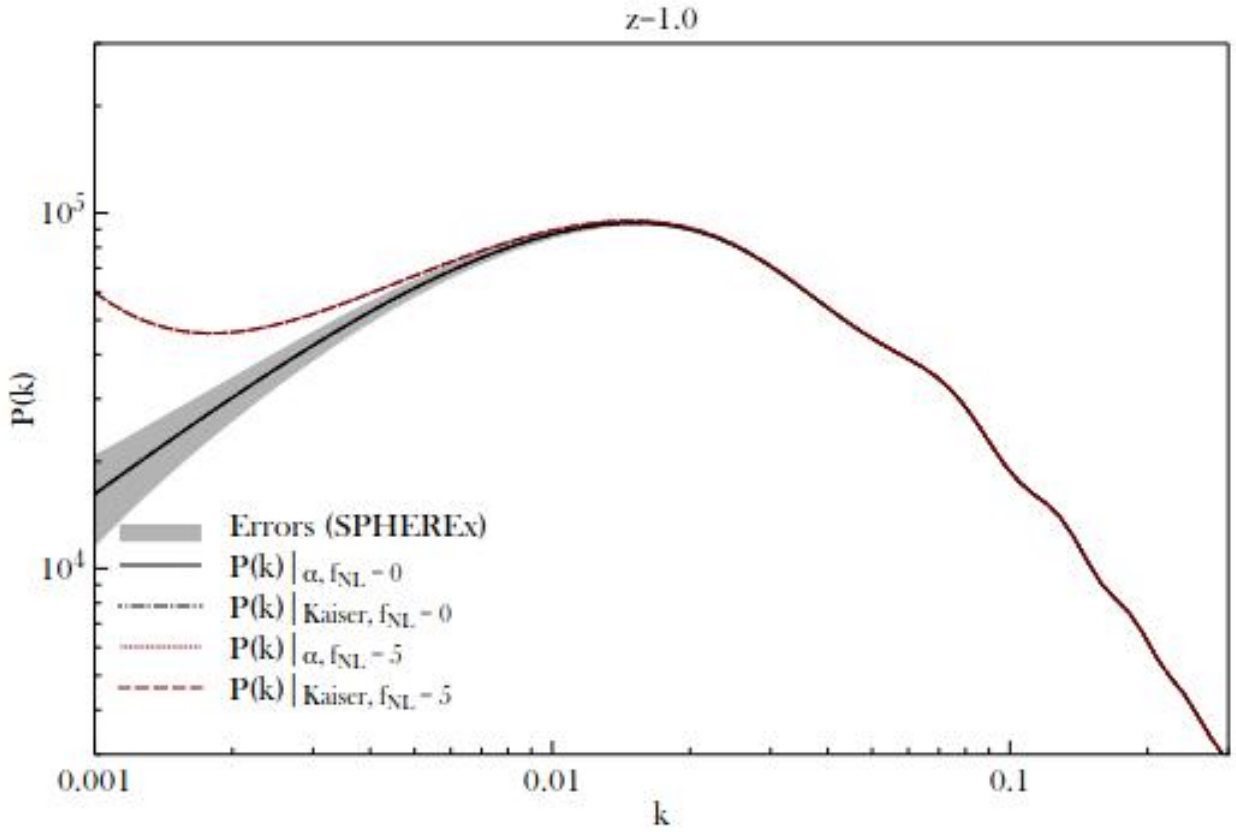

Figure 1.11: The angle averaged power spectra for $z = 1$ computed in the flat-sky approximation (solid black line) with $f_{NL} = 0$ (for a detailed discussion on f_{NL} see section(2.1)), accounting for wide angle effect, that is the Doppler term (dotted black) with $f_{NL} = 0$, in the flat-sky approximation (solid black line) with $f_{NL} = 5$ and accounting for wide angle effect, that is the Doppler term (dotted black) with $f_{NL} = 5$ (Figure from Raccanelli, Bertacca, Jeong, et al. 2016). For comparison are showed the expected error obtained with the SPHEREx (Spectro-Photometer for the History of the Universe, Epoch of Reionization and Ices Explorer), that is a mission that will scan the whole sky. SPHEREx will survey hundreds of millions of galaxies near and far, some so distant their light has taken 10 billion years to reach Earth.

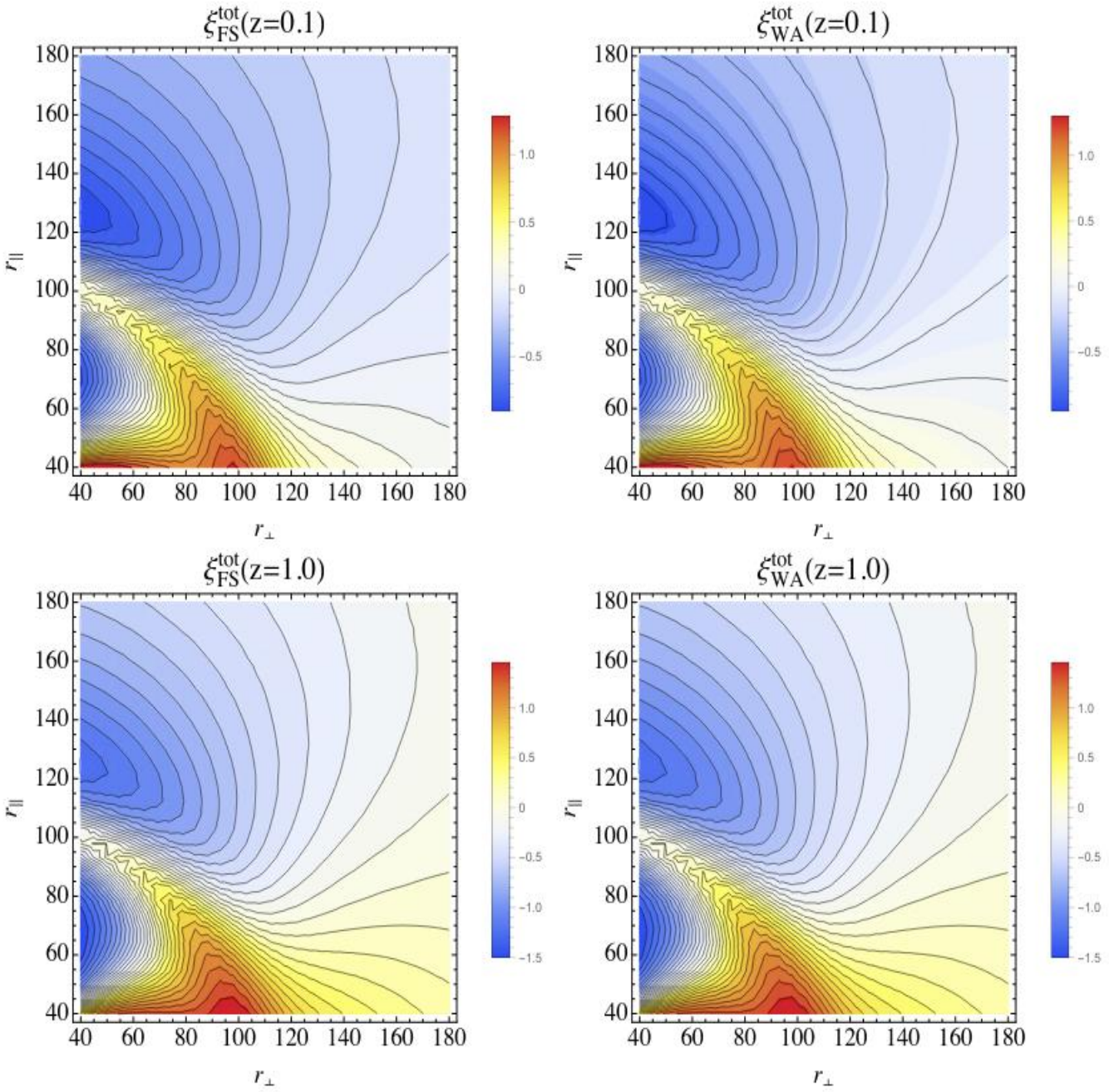

Figure 1.12: 2D redshift space galaxy correlation function accounting (black lines, right) and not accounting (colored contour, left) for the wide angle effects, at redshift bins $z = 0.1$ (top) and $z = 1$ (bottom). At high redshift the Doppler term is negligible. At low-z, in the plane-parallel approximation, the lines overlap meaning that the doppler term is negligible. However, the top right panel shows how the doppler term in the low-z case is not negligible, since the black lines and colored contour are not overlapping, meaning that at low-z the correlation function strongly depends on if the doppler term effects are considered or not. (Figure from Raccanelli, Bertacca, Jeong, et al. 2016)

Chapter 2

Relativistic simulations

2.1 General relativistic effects

In the previous chapter we saw how the peculiar velocities of the galaxies alter the observed galaxy pattern between the Real and Redshift space. The observed redshift and positions of the photons emitted by a galaxy can be actually modified not only by the peculiar velocities, but also by other general relativistic effects (see e.g. Yoo (2009a), Jeong, Schmidt, and Hirata (2012), Bonvin (2014), Challinor and Lewis (2011), Bertacca (2015)). These effects arise from the fact that we observe the photon that had travelled in a perturbed Friedman-Robertson-Walker (hereafter FRW) Universe (see equation(2.22)), and so all the inhomogeneities encountered altered its path and its energy and consequently the inferred position in the sky and redshift, distorting the total galaxy pattern (see e.g. Grimm and Yoo (2021), Grimm, Scaccabarozzi, et al. (2020)). The total effects that have to be taken into account for a proper treatment are:

- *Gravitational lensing*: The path of the photons is altered due to the curvature of the space-time around a perturbation between the source and the observer, meaning that the galaxy is observed in a wrong position in the sky (Bartelmann 2010);

- *Doppler lensing*: This is an effect due to the peculiar motion of a galaxy as showed in fig.(2.2). In the picture there are an observer on the left that observes three galaxy: two with peculiar motion signed by the arrow (galaxy B and C) and the galaxy A at rest. Since the distance of the galaxy C and B is altered, all three galaxies are seen at the same redshift (equal to the redshift of A). This means that since the angular size of B is the same, while the distance inferred is higher, this galaxy will be magnified with respect to A, because for emitting the same flux at an higher inferred distance It should be larger than A; while the galaxy C will be de-magnified, since the distance inferred is shorter (Bacon et al. 2014).

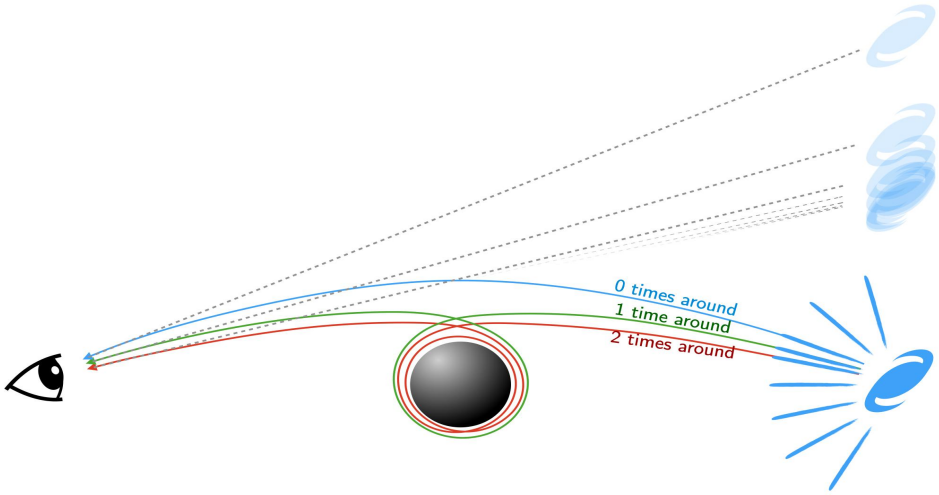

Figure 2.1: A scheme of how the Gravitational lensing distorts the position of a source. The inferred poisition on the sky of the galaxy depends on hoy the photon path was influenced by the inhomogeneity between the observer and the source. Source: "http://cmbcorrelations.pbworks.com", credit: Peter Laursen

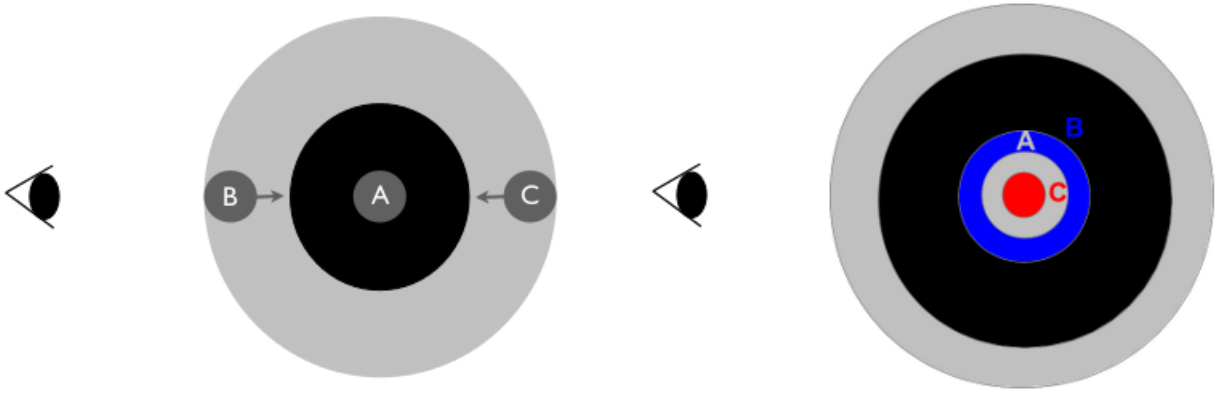

Figure 2.2: A scheme of how doppler lensing works in which are shown how the galaxies are magnified or de-magnified according to their peculiar motion(Bacon et al. 2014)

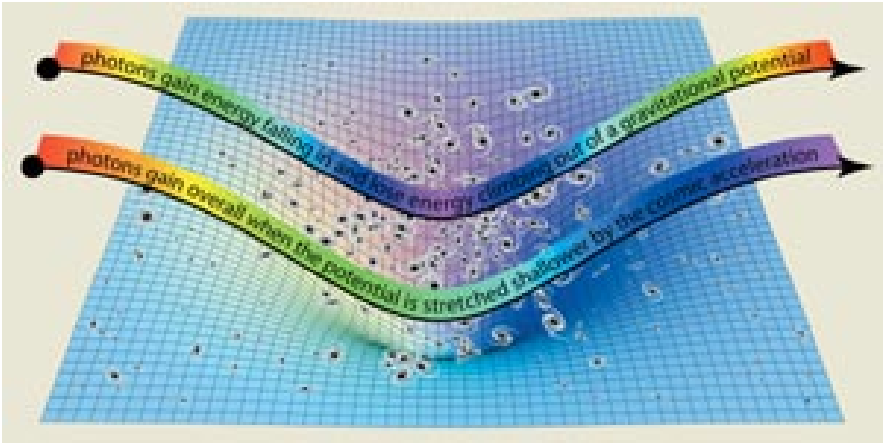

Figure 2.3: A scheme of how Sachs-Wolfe effect works. Are shown the two cases in which a photon acquires or loose energy. Source: (Figure from Nandi 2017b)

- *Sachs-Wolfe effect* (abbreviated SC effect): It gives two contributions:
  Standard SC effect: that modifies the redshift of the photon when it climb the potential well of the emitting source;
  Integrated SC effect: when a photon during its path encounter a gravitational potential, it is subject to a blueshift (rise of energy) when it enters the potential and a redshift (lose of energy) when It climbs away the potential. If the gravitational potential of the source remain constant, the energy of the exiting photon is equal to the energy of the entering one, but if the gravitational potential increase or decrease (for example due to the expansion of the Universe) the energy gained is not equal to the energy lost, so the photon is redshifted or blueshifted as shown in fig(2.3) (Boughn and Crittenden 2005).

- *Shapiro time delay*: due to the space-time dilation around a massive object (Shapiro 1964).

The angular diameter size of a source is its angular widthness. We describe a perturbative correction to the angular diameter distance, relative to the background distance $\bar{d}_A$ at background redshift z_s, by

$$d_A(z_s) = \bar{d}_A(z_s) + \delta d_A(z_s), \tag{2.1}$$

and using the parametrization as in Bacon et al. (2014) we write the perturbed angular diameter size as

$$d_A(z_s, \mathbf{n}) = \bar{d}_A(z_s)[1 - \kappa(z_s, \mathbf{n})], \tag{2.2}$$

with $\bar{d}_A(z_s)$ the angular diameter size for a source observed at z_s in the direction $-\mathbf{n}$ in the perturbed model and k the convergence term, that is a correcting factor which

includes all the contributions of the various gravitational, doppler, Sachs-Wolfe and Integrated Sachs-Wolfe effects:

$$\kappa = \kappa_g + \kappa_d + \kappa_{SW} + \kappa_{ISW}. \tag{2.3}$$

In Bacon et al. (2014) they show that actually the last two terms are sub-dominant so we can write

$$\kappa = \kappa_g + \kappa_d. \tag{2.4}$$

We now briefly discuss when the gravitational lensing is dominant with respect to the Doppler, and vice-versa, as shown in fig(2.4).
The convergence term of the Doppler and Gravitational lensing parts can be written as (Bacon et al. 2014)

$$\kappa_d = \left(1 - \frac{1+z_s}{H\chi_s}\right)\mathbf{v}_s \cdot \mathbf{n}, \tag{2.5}$$

$$\kappa_g = \int_0^{\chi_s} d\chi(\chi_s - \chi)\frac{\chi}{\chi_s}\nabla_\perp \Phi, \tag{2.6}$$

with χ_s the comoving distance, $\mathbf{v}_s$ the velocity of the source and $\mathbf{n}$ the Line of Sight direction and Φ the Bardeen potential (Bardeen 1980), that is a gauge-invariant potential that enters in the perturbed-FRW metric that accounts for the inhomogenities of the metric, as shown in equation(2.22) (see e.g. Uggla and Wainwright 2011, Bardeen 1980). Firstly note that the Doppler terms sign depends on the motion of the source, for object moving towards us $k_v < 0$ so $d_A(z_s, \mathbf{n}) > \bar{d}_A(z_s)$ and the source appears dimmer, so is de-magnified, while if the source is moving away from us $k_v > 0$ and $d_A(z_s, \mathbf{n}) < \bar{d}_A(z_s)$ it appears brighter, thus magnified, as already shown in fig.(2.2). Secondly with increasing redshift, the factor in brackets in equation(2.5) decreases in amplitude, so the magnitude of the Doppler lensing falls, while that of κ_g grows. Therefore k_d profiles change sign at high redshift (Bacon et al. 2014); this is due to an effect which dominates at high redshift, in which the object's image experiences significantly more (or less) cosmic expansion than we inferred from its observed redshift. To have an estimate at which scale the Doppler lensing is important we estimate the velocity contribution $|v| \approx H_0\delta/k$ (Bacon et al. 2014), so we expect that the effect is important on large scales. The region where the Doppler lensing dominates over standard gravitational lensing is shown in Fig.(2.4). Here we expands the κ_d and the κ_g via spherical harmonics (Bacon et al. 2014)

$$\kappa_g(z,\theta,\phi) = \sum_{lm} \kappa^g_{lm} Y_{lm}(\theta,\phi), \quad \kappa_d(z,\theta,\phi) = \sum_{lm} \kappa^d_{lm} Y_{lm}(\theta,\phi), \tag{2.7}$$

where the coefficients κ^g_{lm} and κ^d_{lm} are (Bacon et al. 2014)

$$\kappa^g_{lm}(z) = \int d\Omega_\theta d\Omega_\phi Y^*_{lm}(\theta,\phi)\kappa_g(z,\theta), \tag{2.8}$$

$$\kappa^d_{lm}(z) = \int d\Omega_\theta d\Omega_\phi Y^*_{lm}(\theta,\phi)\kappa_d(z,\theta). \tag{2.9}$$

The angular auto-power spectrum $C_l(z,z')$ between two redshift z and z' can be extracted from the average (Bacon et al. 2014)

$$\langle \kappa^i_{lm}(z)\kappa^i_{l'm'(z'}\rangle = C^{ij}_l(z,z')\delta_{ll'}\delta_{mm'} \quad with \quad i = g,d \tag{2.10}$$

The "l" index is associated with the number of spatial oscillations, also called nodes, that are equal $l+1$ in the θ direction in spherical coordinates, and "m", the number of spatial oscillations (nodes) in the ϕ direction. m varies from "˘l" to "l". For example, the $l = 0$ mode has zero oscillation in the θ direction, i.e., a monopole, or constant value over the whole sphere, that sets the overall scale. $l = 1$ is a dipole: one full oscillation over the sphere in the θ direction. Go to higher and higher l values, and you get more spatial oscillations (and therefore smaller wavelength) over the sphere surface. We see that Doppler lensing dominates over gravitational lensing from medium to low redshifts and wavenumbers ($l \leq 1000$ at $z = 0.2$ and $l \leq 100$ at $z = 0.4$). Be careful that we are only comparing the "importance" of these two lensing, because both at large scales have to be considered since their contributions even if is not the same, it is non-negligible. It is very important to note also that the importance ranges are divided also in "wide angle" and "small scale", this means that the doppler lensing dominated over the gravitational lensing also if the observational angle under which the galaxies are seen is wide, as seen in the previous section. On the contrary for small angles the gravitational lensing dominates.

All the presented effects (Gravitational and Doppler lensing, SC effects and time-delay) begin to become non-negligible at large scales and since modern galaxy survey are able to observe portion of Universe comparable with the horizon $1/H(z)$ (see e.g. DESI Collaboration et al. 2016, Doré et al. 2014, R. Scaramella et al. 2022, Weltman et al. 2020), they could be effectively detectable (see e.g. Yoo 2009a, Jeong, Schmidt, and Hirata 2012, Bonvin 2014, Challinor and Lewis 2011, Bertacca 2015). At these scales the galaxy count is affected by the peculiar motion of the galaxies as described in the previous chapter (Kaiser 1987, A. J. S. Hamilton 1998), magnification due to lensing (see e.g. Sasaki 1987, Matsubara 2000)) and the other presented general relativistic effects (see e.g. Bertacca et al. 2012, Raccanelli, Bertacca, Doré, et al. 2014, Raccanelli, Bertacca, Maartens, et al. 2016,Raccanelli, Montanari, et al. 2016, Gaztanaga, Bonvin, and Hui 2017)). The depth and in particular the wide observational angle of modern survey make these effects indispensable for a complete cosmological treatment, because they can affect a lot of cosmological quantities. For example as

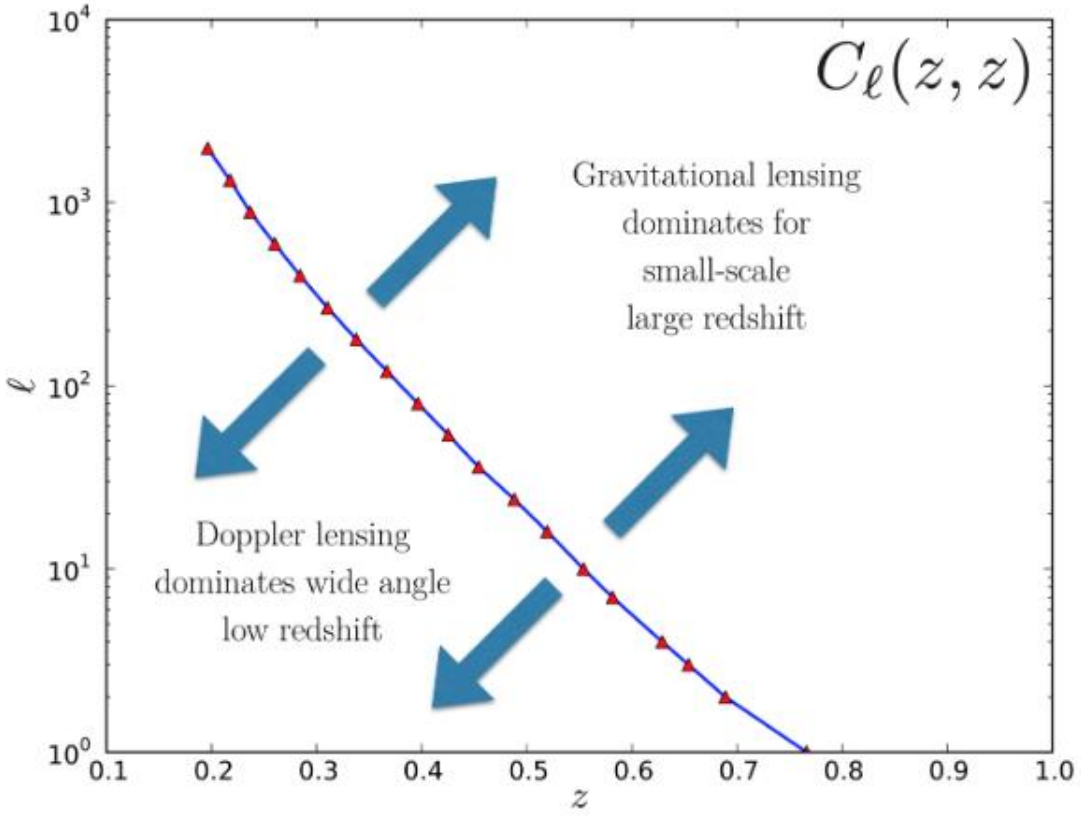

Figure 2.4: The red dot are the points where the doppler lensing multipoles power is equal to the gravitational one in function of the redshift, with the blue line the interpolating function. The plot shows the ranges in which the gravitational and doppler lensing dominates. The former at large redshift and small observational angle, while the latter for low redshift and wide observational angle. (Figure from Bacon et al. 2014)

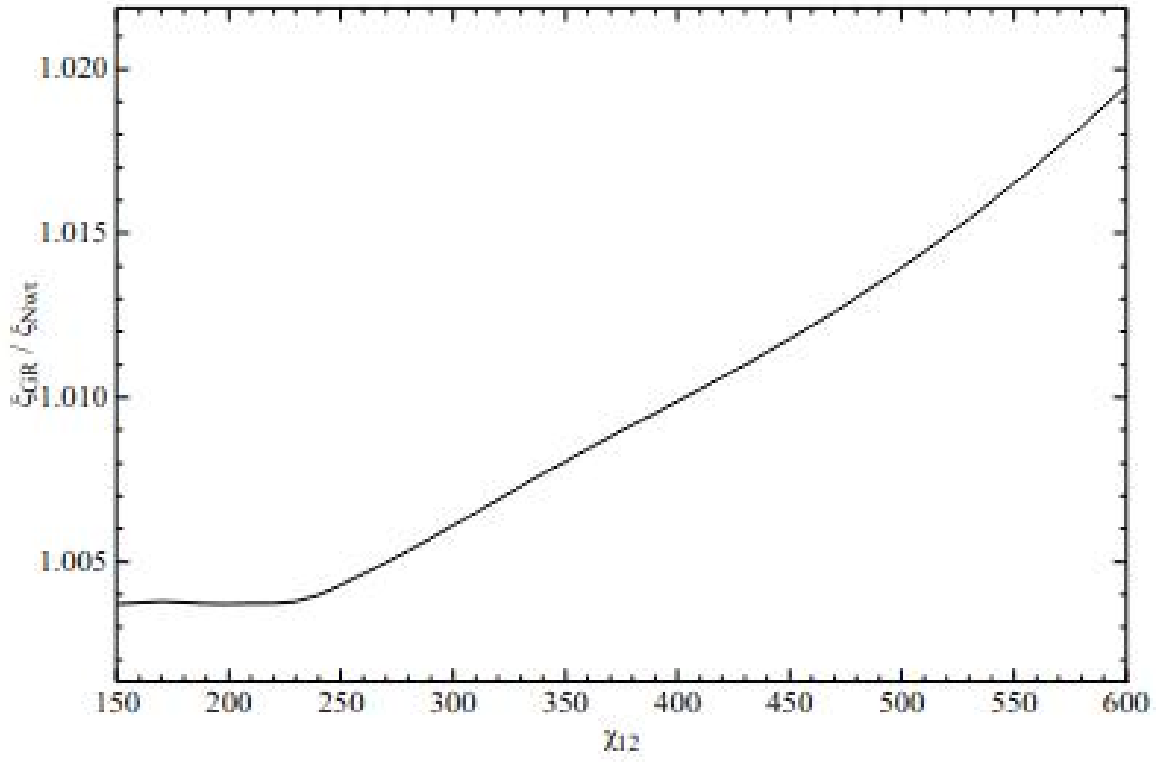

Figure 2.5: Ratio between the correlation function accounting for general relativistc effects and in the Newtonian case. (Figure from Bertacca et al. 2012)

showed in Bertacca et al. (2012), the galaxy correlation function and so the power spectrum in Redshift Space at large scale have to include these effects to recover the proper behaviour at large scales. In figure(2.5) is plotted the ratio of the redshift space galaxy correlation function accounting for the general relativistic effects and the one that consider the Newtonian plane-parallel approximation, in function of the angular separation of the pair of galaxies χ_{12}. It is visible that the two correlations function deviates for wide galaxy separation angles, while for low separation angle we recover the flat-sky approcimation and so the ratio$\rightarrow 1$, so it necessary to include the relativistic effects to recover the right correlation function and so the power spectrum.

Since these quantities are present in the large scale part of the power spectrum, it is immediate to observe that they could affect also the inference of the primordial non-Gaussianity (as anticipated in section1.5). In the standard model of cosmology, the primordial perturbations, corresponding to the seeds for the LSS, are chosen from a Gaussian distribution with random phases. Actually the central limit theorem (Kwak and Kim 2017) implies that a Gaussian distribution arises whenever one has a variable which is a linear superposition of a large number of independent random variables which are all drawn from the same distribution. Nevertheless, a minimal deviation from Gaussianity is perhaps the most robust theoretical prediction of models that explain the observed Universe; it is necessarily present even in the simplest scenario (see e.g. Bartolo et al. 2004. In addition, most inflationary models produce far higher levels of non-Gaussianity. Since non-Gaussianity directly probes the dynamics in the early Universe, a detection would present a monumental discovery in cosmology, providing clues about physics at very high energy scales. (see e.g. Byrnes and Choi 2010, Celoria and Matarrese 2018, Meerburg et al. 2019). The common parametrization of the non-Gaussianities is the f_{NL} parametrization, where the Bardeen potential is written as (Raccanelli, Bertacca, Maartens, et al. 2016)

$$\Phi_{NG} = \phi + f_{NL}(\phi^2 - \langle\phi^2\rangle), \tag{2.11}$$

that on scales lower than the Hubble scale reduces to the Newtonian one. ϕ is a gaussian random field and f_{NL} include the degree of deviation from Gaussianity. As showed in Dalal et al. (2008) the amount of galaxy cluster depends on the value of the assumed f_{NL}. In fact in figure(2.6) are shown various simulation that assumes a ΛCDM model with $\Omega_m = 0.24$ and $\Omega_\Lambda = 0.76$ at redshift $z = 0$ generated with the same Fourier phases, but with (from top to bottom) $f_{NL} = -5000, -500, 0, +500, +5000$. Each slice is 375 h^{-1}Mpc wide, and 80 h^{-1} Mpc high and deep. Note that for positive f_{NL}, overdense regions are more evolved and produce more clusters than their Gaussian counterparts, while underdense regions are less evolved. For negative f_{NL}, underdense regions are more evolved, producing deeper voids, while overdense regions are less evolved, as illustrated by the grid lines apparent in the left of the top panel. This shows that f_{NL} influence the galaxy cluster, but actually we use the galaxy cluster to infer it (Cunha,

Huterer, and Doré 2010), so since the clustering is affected by the general relativistic effects, this implies that also f_{NL} is affected. In particular, f_{NL} introduces a scale-dependent modification of the large-scale halo bias (Dalal et al. 2008) that is written (see e.g. Dalal et al. 2008,Raccanelli, Bertacca, Maartens, et al. 2016)

$$b(k) = b + \Delta b(k), \tag{2.12}$$

with

$$\Delta b(z,k) = [b(z) - p] f_{NL}(k) \delta_{ec} \frac{3\Omega_{m,0} H_0^2}{k^2 T(k) D(z)}, \tag{2.13}$$

where $b(z)$ is the usual bias calculated assuming Gaussian initial conditions, which we assume to be scale-independent, $1 < p < 1.6$ and $p = 1$ for galaxies that entirely populates halos in a given mass range and $p = 1 + \delta_{ec}^{-1} \approx 1.6$ for galaxies that populates only recently merged halos (Slosar et al. 2008), $D(z)$ is the linear growth factor, $\Omega_{m,0}$ is the matter density parameter at present day and δ_{ec} is the critical value of the matter over-density for ellipsoidal collapse set to $\delta_{sc} \approx 1.68$ (see e.g. R. K. Sheth, Mo, and Tormen 2001). The f_{NL} parameter is assumed scale-dependent (Raccanelli, Bertacca, Maartens, et al. 2016)

$$f_{NL}(k) = f_{NL} \left(\frac{k}{k_{*,NG}} \right)^{n_{NG}}, \tag{2.14}$$

with the pivot scale $k_{*,NG} = 0.04\ h\ \mathrm{Mpc}^{-1}$ and $n_{NG} \approx O(1)$. In figure(2.7) are shown the ellipsoidal errors on f_{NL} and n_{NG} accounting for the general relativistic effects (solid line) and with a Newtonian treatment (dashed line) for a SKA-like (Weltman et al. 2020) and Euclid-like (R. Scaramella et al. 2022) survey after marginalizing over all the others parameters. It is visible that accounting for general relativistic effects produces more restricted constraints, and so they are fundamental for putting more bounds in the inference of this parameter.

General relativistic effects don't impact only the estimation of non-Gaussianities, but as showed in Raccanelli, Bertacca, Maartens, et al. (2016) and Lorenz, Alonso, and Ferreira (2018) also the constraint on the Dark matter nature can be affect. Nowadays its nature remain an open question in Cosmology, even its most basic behaviour, for example if it has a constant value of it varies with time (Yang et al. 2018). Dark energy is distinguished from the cosmological constant simply considering that the latter has an equation of state $w = p/\rho = -1$ with p the pressure and ρ the energy density of the "cosmic fluid", while the former has an unknown equation of state, and so its ratio is written as (see e.g. Raccanelli, Bertacca, Maartens, et al. 2016, Linder 2003, Linder 2005)

$$w(a) = w_0 + w_a(1 - a), \tag{2.15}$$

with $w(a)$ normalized as $w(a) = 1$ at $a_0 = 1$. It is called "dynamical dark matter" since it depend on the scale factor and so evolves with time. To constrain a dark matter model

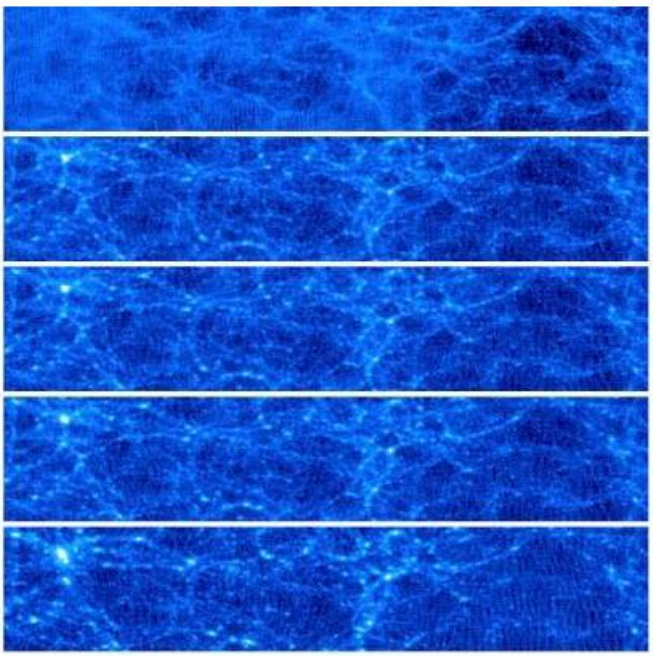

Figure 2.6: The dependence of the galaxy clustering on the f_{NL} value: (from top) $f_{NL} = -5000, -500, 0, +500, +5000$. (Figure from Dalal et al. 2008)

we have to put constrain on the w_0 and w_a parameter, and so in figure(2.8) are shown the constraints on the dynamical dark energy parameters for survey like the SKA and Euclid one, marginalized over other cosmological parameter. As before the constraint that accounts for general relativistic effects are more bounded and restricted, meaning another time that these effects are fundamental for the cosmological parameter estimation.

How these effects change the power spectrum?

Now we show how the presence of the general relativistic effects can alter the power spectrum. In Jeong, Schmidt, and Hirata (2012) and Challinor and Lewis (2011) they derive a complete and self-consistent treatment of the power spectrum accounting for the peculiar velocities of the galaxies and also for the general relativistic effects. Here we highlight the main result. In figure(2.9) are shown the three dimensional galaxy power spectra of the Kaiser prediction (dotted line) (Kaiser 1987), of the kaiser prediction with a $f_{NL} = -0.147$ (dashed line) and the one that accounts for the General relativistic effects (thick line), all at various redshift bins and bias factor b. The vertical line is at $k = aH$, that is the horizon. At small scales the behaviour of the power spectra is basically the same, and begins to deviate when the scales approaches $k \leq 10^{-3}\ h\,\mathrm{Mpc}^{-1}$. At larger scales the contribution of the general relativistic effects presented becomes dominant, and it is much higher with respect to the Kaiser one. Note that at all redshift the power spectrum with general relativistic effects has this behaviour. One very im-

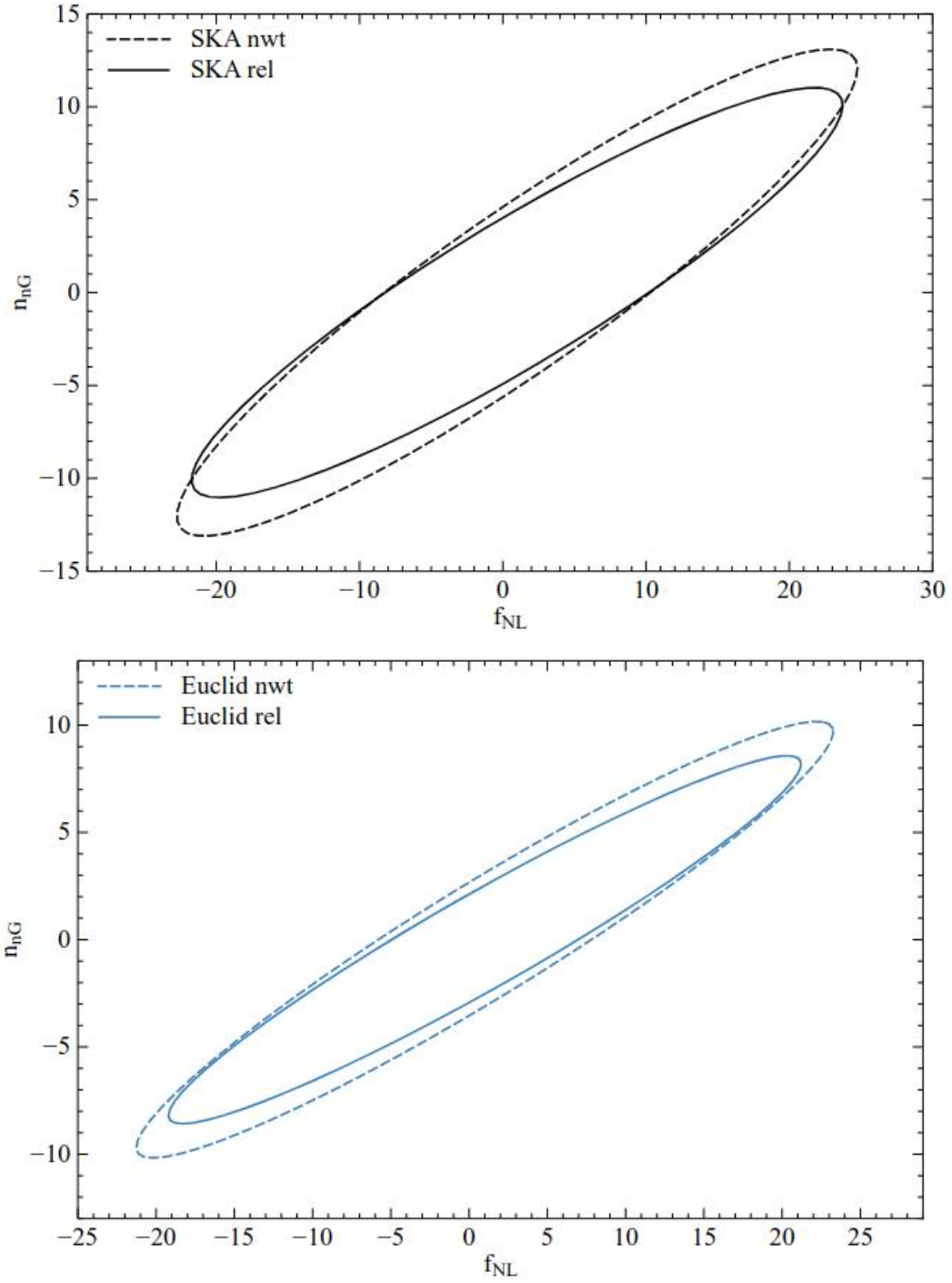

Figure 2.7: Ellipsoidal error on the f_{NL} and n_{NG} parameters, accounting (solid line) and not accounting (dotted line) for general relativistic effects (Figure from Raccanelli, Bertacca, Maartens, et al. 2016)

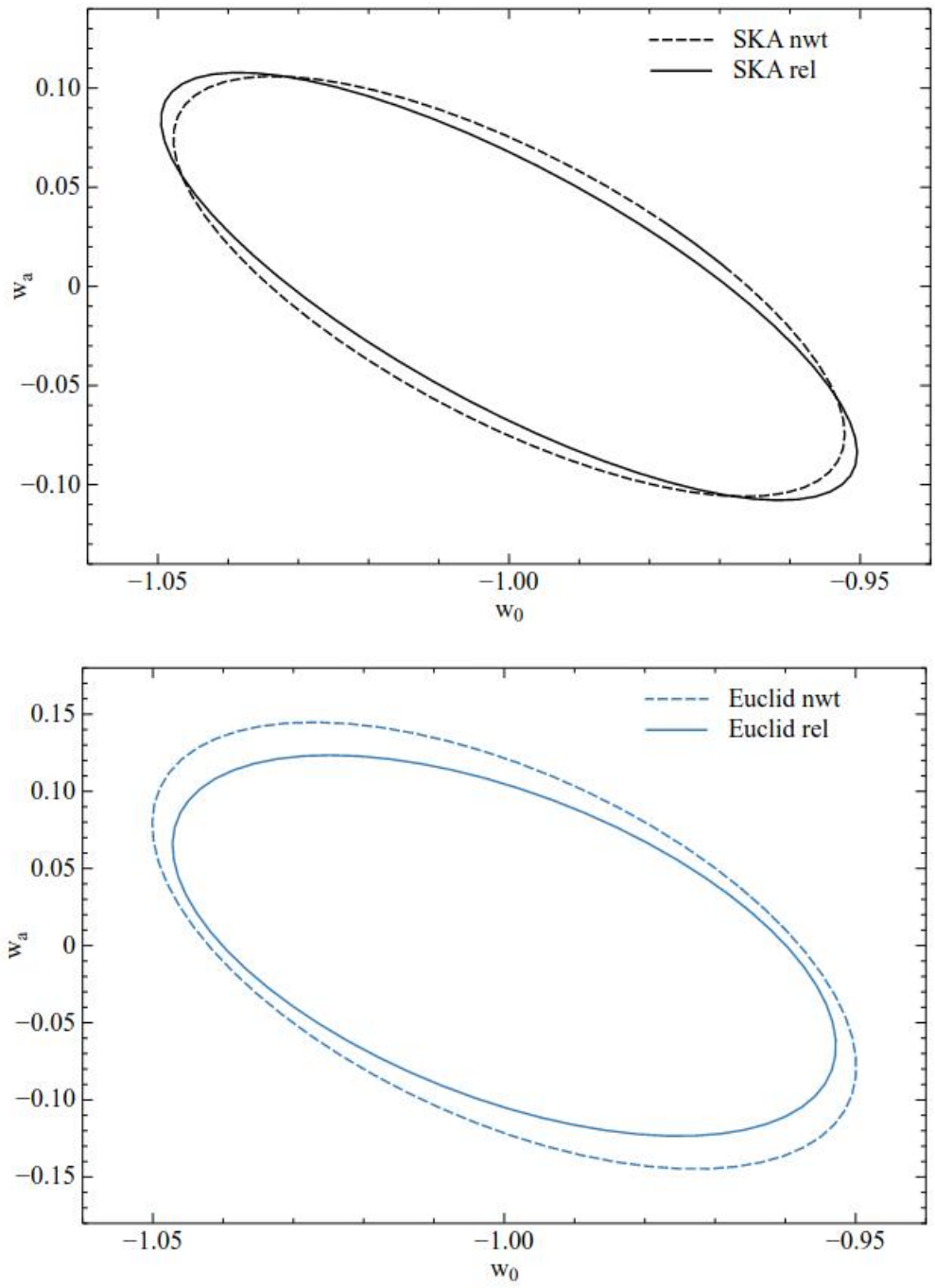

Figure 2.8: Ellipsoidal error on the w_0 and w_a parameters, accounting (solid line) and not accounting (dotted line) for general relativistic effects(Figure from Raccanelli, Bertacca, Maartens, et al. 2016)

portant thing to note is the behaviour of the power spectrum with the relativistic effects and the one with the kaiser prescription plus a non-gaussian parameter, since as said in the previous section, the presence of the relativistic effects can "induce" a non-gaussian behaviour at large scale and in fact the two spectra are very similar. In figure (2.10) is shown instead the two-dimensional redshift galaxy power spectrum divided in the components of the modes parallel to the line Of Sight $k_{//}$ and perpendicular $k_{\perp}$, for various redshift and bias factor. Here are showed the result including the relativistic effects (black solid lines), the Newtonian result from Kaiser (contour and dashed line). The first thing that we can note is the typical behaviour of the "squashed" configuration in redshift space, as shown in the first chapter, that become more and more squashed along the perpendicular direction as redshift increases. Second note that the contour and solid lines deviates only at large scales (as saw in figure(2.9)), becoming very distinguishable again around $k \leq 10^{-3}\ h\,\mathrm{Mpc}^{-1}$.

In the next section we will give a quantitative explanation on how LIGER is able to account for the Redshift Space Distortions and the general relativistic effects to create galaxy mocks.

2.2 LIGER theory

As shown in figure(2.11) we observe a galaxy as it was at the time when its world-line intersect our past light cone (see e.g. Cuesta-Lazaro et al. 2018). The null geodesic of the photon emitted by a galaxy is altered due to all the perturbations on its path, so actually we observe the modified photon path. In figure(2.11) the direction $\mathbf{n}_r$ is the actual direction of the galaxy, while $\mathbf{n}_s$ is the direction under which the galaxy is observed after the perturbation of its position. The position of the galaxy can be parametrized by two angles that indicates its position $\mathbf{n}_s$ in the sky and its redshift z that indicates the distance. We can think as the actual position of the galaxy in the sky is displaced by $\Delta x_i = n_s^i \delta\chi + \delta x^i$ that is the displacement vector that connects the actual position and the observed one. It is composed by the first term that is a displacement in the distance and the second that is a displacement in the position on the sky. What LIGER does essentially is to compute this displacement vector Δx^i in order or be able to create a map between the Real and Redshift space accounting for the peculiar velocities and the general relativistic effects. As showed in (Borzyszkowski, Bertacca, and Porciani 2017) in redshift space a null geodesic from an observed galaxy is described by the 4-vector:

$$x_{\mathrm{s}}^{\mu} = (\eta_{\mathrm{s}}, \mathbf{x}_{\mathrm{s}}) = (\eta_0 - \chi_{\mathrm{s}}, \chi_{\mathrm{s}}\mathbf{n}_{\mathrm{s}})\,, \tag{2.16}$$

with η_0 the conformal time at present time, $\mathbf{n}_{\mathrm{s}}^i = \mathbf{x}_{\mathrm{s}}^i/\chi_{\mathrm{s}}$ a unit vector that point to the galaxy position in the sky and $\chi_{\mathrm{s}}(z)$ the comoving distance. The relation between the position in Real space and Redshift space is given by (Borzyszkowski, Bertacca, and

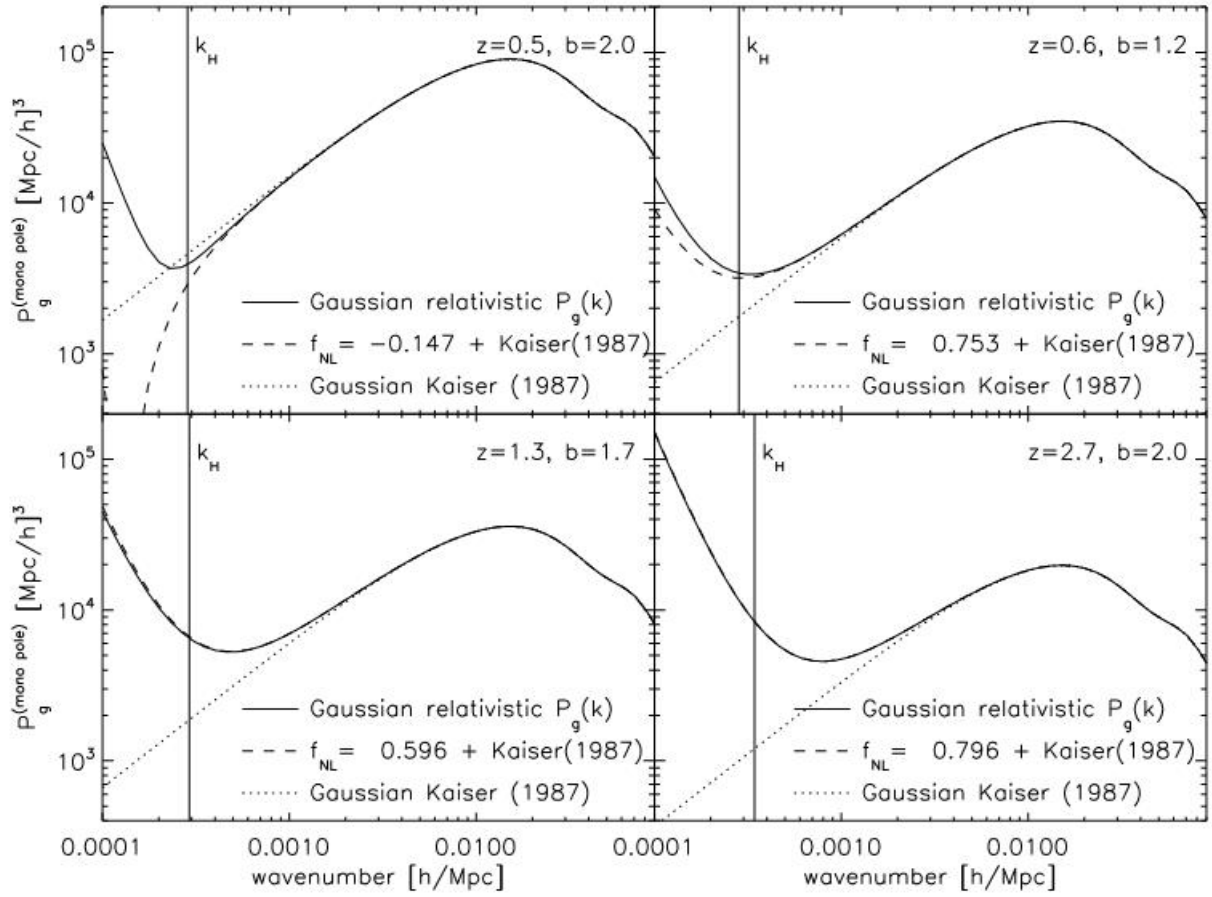

Figure 2.9: The three dimensional galaxy power spectra of the Kaiser prediction (dotted line) (Kaiser 1987), of the kaiser prediction with a $f_{NL} = -0.147$ (dashed line) and the one that accounts for the General relativistic effects (thick line), all at various redshift bins and bias factor b. The vertical line is at $k = aH$, that is the horizon.(Jeong, Schmidt, and Hirata 2012)

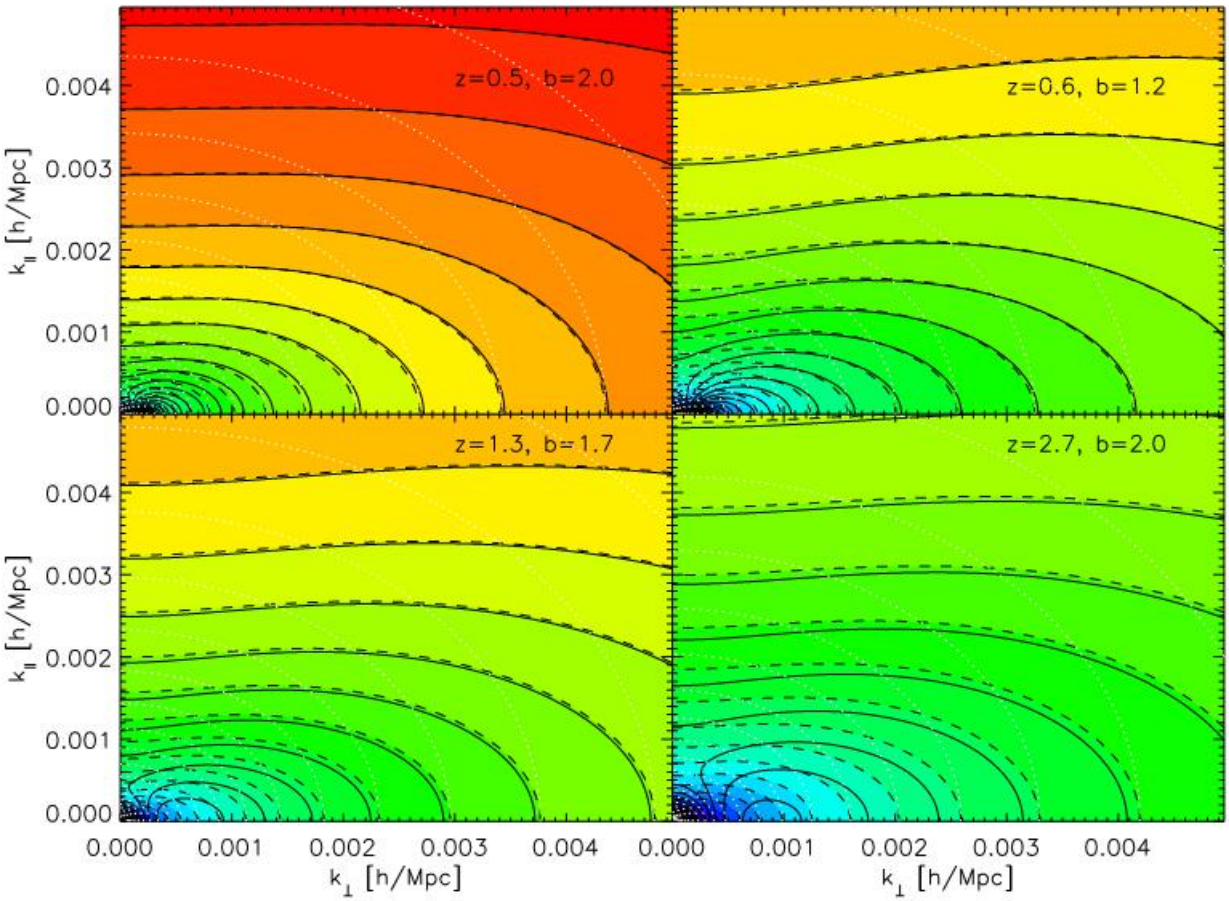

Figure 2.10: The two-dimensional redshift galaxy power spectrum divided in component of the modes parallel to the line Of Sight $k_{//}$ and perpendicular $k_{\perp}$, for various redshift(Jeong, Schmidt, and Hirata 2012) and bias factor

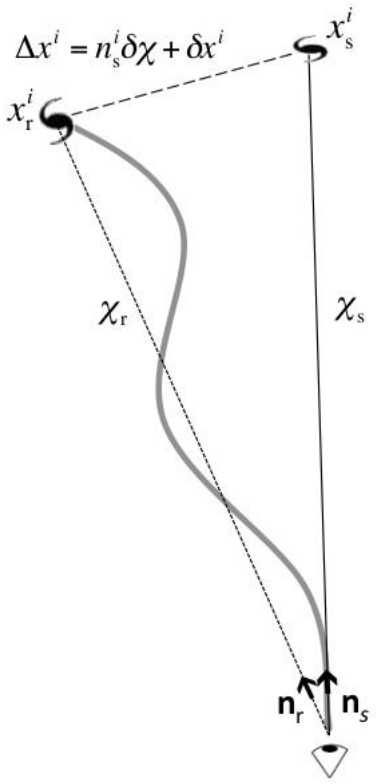

Figure 2.11: The configuration of how the path of a photon is altered and consequently the position of the emitting galaxy (Figure from Borzyszkowski, Bertacca, and Porciani 2017)

Porciani 2017)

$$x_{\rm r}^{\mu}\left[\chi_{\rm r}\left(\chi_{\rm s}\right)\right]=x_{\rm s}^{\mu}\left(\chi_{\rm s}\right)+\Delta x^{\mu}\left(\chi_{\rm s}\right). \tag{2.17}$$

This means that the actual position of the galaxy is the one observed into the redshift map, plus a 4-vector that contains the displacement due to the various effects $\Delta x^{\mu}\left(\chi_{\rm s}\right)$. Since the displacement are very small, we can write $\chi_{\rm r}=\chi_{\rm s}+\delta\chi$ and perturbing x_r^{μ} around x_s^{μ} we obtain at linear order (Borzyszkowski, Bertacca, and Porciani 2017)

$$x_{\rm r}^{\mu}\left(\chi_{\rm r}\right)=x_{\rm s}^{\mu}\left(\chi_{\rm r}\right)+\delta x^{\mu}\left(\chi_{\rm r}\right) \tag{2.18}$$

$$=x_{\rm s}^{\mu}\left(\chi_{\rm s}\right)+\frac{{\rm d}x_{\rm s}^{\mu}}{{\rm d}\chi_{\rm s}}\delta\chi+\delta x^{\mu}\left(\chi_{\rm s}\right), \tag{2.19}$$

and so combining equation (2.17) and (2.18), the displacement is written as (Borzyszkowski, Bertacca, and Porciani 2017)

$$\Delta x^{0}(\chi_s)=-\delta\chi+\delta x^{0}(\chi_s), \tag{2.20}$$

$$\Delta x^{i}(\chi_s)=n_s^{i}\delta\chi+\delta x^{i}(\chi_s), \tag{2.21}$$

assuming that ${\rm d}/{\rm d}\chi_{\rm s}=-\partial/\partial\eta_{\rm s}+n_{\rm s}^{i}\partial/\partial x_{\rm s}^{i}$, χ_s as affine parameter and that at linear order $dx_s^i/d\chi_s=n_s^i$. Knowing $\delta\chi$, δx^0 and δx^i means to know how the position of the galaxy is displaced, and so now our aim is to compute esplicity these terms, studying how the Redshift Space Distortions and the general relativistic effects actually contribute.

In the linear regime the perturbed metric in the Poisson gauge is (see e.g. Bardeen 1980, Peebles 1982, Dodelson 2003, Brandenberger 2001)

$${\rm d}s^2=a^2(\eta)\left[-(1+2\Psi){\rm d}\eta^2-(1-2\Phi)\delta_{ij}\,{\rm d}x^i\,{\rm d}x^j\right], \tag{2.22}$$

with Ψ and Φ the Bardeen potentials of the inhomogeneities and $a(\eta)$ the scale factor. A zero-shear velocity field u^{μ} projected along ∂_{μ} can be written as (Challinor and Lewis 2011, Bardeen 1980, Peebles 1980b)

$$u^{\mu}=a^{-1}(1-\psi)\delta_0^{\mu}, \tag{2.23}$$

$$u_{\mu}=a(1+\psi)\delta_{\mu 0}. \tag{2.24}$$

We decompose the wavevector $k^{\mu}={\rm d}x^{\mu}/{\rm d}\lambda$ into a directional part e^a and a frequency (energy) part that satisfy $k\cdot u=\varepsilon/a$, so that the differential equation for the photon can be written as

$$\frac{{\rm d}\mathbf{x}}{{\rm d}\eta}=(1+\phi+\psi)\mathbf{e}, \tag{2.25}$$

$$\frac{{\rm d}\eta}{{\rm d}\lambda}=a^{-2}\varepsilon(1-\psi). \tag{2.26}$$

This implies that the geodesic equation is simply given by a propagation equation of $\mathbf{e}$ that account for the "positional" part and an evolutionary equation of the frequency ε that account for the energy of the photon. We can then write the geodesic equation as a propagation equation for $\mathbf{e}$ and an evolution equation for the frequency

$$\frac{\mathrm{d}\mathbf{e}}{\mathrm{d}\eta} = -\nabla_{\perp}(\phi+\psi), \tag{2.27}$$

$$\frac{\mathrm{d}\varepsilon}{\mathrm{d}\eta} = -\varepsilon\frac{\mathrm{d}\psi}{\mathrm{d}\eta} + \varepsilon(\dot{\phi}+\dot{\psi}), \tag{2.28}$$

where $\nabla_{\perp} = \nabla - e\cdot\nabla$.
Combining equations (2.25), (2.26) and the integral with the propagation equation of $\mathbf{e}$ we recover the equation for a generic photon path (Challinor and Lewis 2011)

$$\mathbf{x}(\hat{\mathbf{n}};\eta) = -\mathbf{e}_{\mathrm{o}}(\eta_{\mathrm{o}}-\eta) + \mathbf{e}\int_{\eta_{\mathrm{o}}}^{\eta}(\psi+\phi)\mathrm{d}\eta' - \int_{\eta_{\mathrm{o}}}^{\eta}(\eta-\eta')\,\nabla_{\perp}(\psi+\phi)\mathrm{d}\eta', \tag{2.29}$$

Where "o" means that are quantities seen by the observer so that $-\mathbf{e}_o$ is the Line-of-sight direction for a Newtonian-gauge observer. Equation(2.29) states that the position of an observed galaxy is due to the summation of the first term that is the "unperturbed" one, since it account only for the cosmic time at which the photon was emitted (in the direction $-\mathbf{e}_o$) through the observer; and the last two terms that account for the "perturbed" part (in fact are the only terms where the Bradeen potentials appear), with the first that is the radial displacement that correspond to the Shapiro time delay and the second is the transverse displacement due to the lensing.

What is missing is how the redshift (and so the radial part) are affected by the perturbation along the path. We begin by the usual relation between the emitted redshift ("e") considered perfectly known and the observed ("o"), that is translated into an equation of the energies (Borzyszkowski, Bertacca, and Porciani 2017)

$$1+z = \frac{\left(u_{\mathrm{e}}^{\mu}k_{\mu}\right)\big|_{\mathrm{e}}}{\left(u_{\mathrm{o}}^{\mu}k_{\mu}\right)\big|_{o}}, \tag{2.30}$$

we decompose the velocities both of the source and of the observer into two components:

$$u_{\mathrm{e}}^{\mu} = u^{\mu} + v_{\mathrm{e}}^{\mu}, \tag{2.31}$$

$$u_{\mathrm{o}}^{\mu} = u^{\mu} + v_{\mathrm{o}}^{\mu}. \tag{2.32}$$

Regarding that $u_s^{\mu} = a^{-1}[1-\psi, v^i]$, equation (2.30) becomes (Challinor and Lewis 2011)

$$1+z = \frac{a_{\mathrm{o}}}{a}\frac{\varepsilon}{\varepsilon_{\mathrm{o}}}\left[1+\hat{\mathbf{n}}\cdot(\mathbf{v}_{\mathrm{e}}-\mathbf{v}_{\mathrm{o}})\right], \tag{2.33}$$

with $\hat{\mathbf{n}} = -\mathbf{e}_{oA}$ the line-of-sight direction. The energy ratio $\varepsilon/\varepsilon_{\rm o}$ can be determined from integrating the energy evolution (equation(2.28))

$$\frac{\varepsilon}{\varepsilon_{\rm o}} = 1 + \psi_{\rm o} - \psi + \int_{\eta_{\rm o}}^{\eta} (\dot{\psi} + \dot{\phi}) {\rm d}\eta', \tag{2.34}$$

that as before is divided into the first term that is the "unperturbed" part (in fact the emitted and observed energies are equals if there are not perturbation along the path) and the "perturbed" part that contain the standard Sachs-Wolfe effect and the integrated Sachs-Wolfe (ISW) effect. So combining equations (2.33) and (2.34) we write

$$1 + z = \frac{a_{\rm o}}{a} \left[1 + \psi_{\rm o} - \psi + \int_{\eta_{\rm o}}^{\eta} (\dot{\psi} + \dot{\phi}) {\rm d}\eta' + \hat{\mathbf{n}} \cdot (\mathbf{v}_{\rm e} - \mathbf{v}_{\rm o}) \right]. \tag{2.35}$$

Setting $\eta \equiv \eta_{\rm s} + \delta\eta$, thus η is given by t its value for a source of redshift $z_{\rm s}$ plus a little displacement where the unperturbed metric relation $1 + z_{\rm s} = a_{\rm o}/a(\eta_{\rm s})$ holds, we must have

$$\delta\eta = \frac{1}{\mathscr{H}(\eta_{\rm s})} \left[\psi_{\rm o} - \psi + \int_{\eta_{\rm o}}^{\eta_{\rm s}} (\dot{\psi} + \dot{\phi}) {\rm d}\eta' + \hat{\mathbf{n}} \cdot (\mathbf{v}_{\rm e} - \mathbf{v}_{\rm o}) \right], \tag{2.36}$$

and so combining this with equation (2.29) we obtain the radial position of a photon at observed source redshift z_s (Challinor and Lewis 2011)

$$\chi(\hat{\mathbf{n}}, z_{\rm s}) = \chi_{\rm s} + \delta\chi = \eta_{\rm o} - \eta_{\rm s} - \delta\eta - \int_{\eta_{\rm o}}^{\eta_{\rm s}} (\psi + \phi). \tag{2.37}$$

So writing the positional shift as in equation (2.20), substituting all the perturbed quantities just found and setting the observer spatial coordinate to zero, we ends up with the final coordinate displacement for the galaxies position between the Redshift and Real space (Borzyszkowski, Bertacca, and Porciani 2017):

$$\begin{aligned}\delta\chi = &-\left(\chi_{\rm s} + \frac{1}{\mathscr{H}}\right) \left[\psi_{\rm o} - \left(n_{\rm s}^i v_i\right)_{\rm o}\right] + \frac{1}{\mathscr{H}} \left[\psi_{\rm e} - \left(n_{\rm s}^i v_i\right)_{\rm e}\right] + \frac{1}{\mathscr{H}} \int_0^{\chi_{\rm s}} \partial_0(\phi + \psi) {\rm d}\chi \\ &+ \int_0^{\chi_{\rm s}} \left[2\psi + (\chi_{\rm s} - \chi)\, \partial_0(\phi + \psi)\right] {\rm d}\chi,\end{aligned} \tag{2.38}$$

$$\delta x^0 = -\chi_{\rm s} \left[\psi_{\rm o} - \left(n_{\rm s}^i v_i\right)_{\rm o}\right] + 2\int_0^{\chi_{\rm s}} \psi {\rm d}\chi + \int_0^{\chi_{\rm s}} (\chi_{\rm s} - \chi)\, \partial_0(\phi + \psi) {\rm d}\chi, \tag{2.39}$$

$$\delta x^i = -\left(v_{\rm o}^i + \phi_{\rm o} n_{\rm s}^i\right) \chi_{\rm s} + 2 n_{\rm s}^i \int_0^{\chi_{\rm s}} \phi {\rm d}\chi - \int_0^{\chi_{\rm s}} (\chi_{\rm s} - \chi)\, \delta^{ij} \partial_j(\phi + \psi) {\rm d}\chi, \tag{2.40}$$

with $\mathscr{H} = \partial_0 {\rm ln} a$. These equations are the explicit form of the displacement in equation(2.20), accounting for how the inferred position of a source is affected by the various relativistic effects presented and by the peculiar velocities.

2.2.1 Magnification

Since the Redshift Space Distortions alter the both the position and the distance of a galaxy, we have to be careful when we study the flux received from a galaxy (see e.g. Hui, Gaztañ aga, and LoVerde 2008, Breton, Torre, and Piat 2022). If a galaxy is saw at redshift $z1$ under a solid angle Ω_{z1} and flux F_{z1} and supposing that its actual redshift is at $z2 > z1$, this implies that the galaxy to emit the observed flux has to be brighter than inferred, since it is farther. For same reason if the actual position is at $z3 < z1$, to have the same flux and solid angle it has to be fainter then expected at $z1$. This effect is called Magnification and it is important for limited in flux survey, that select only galaxy in a certain range of luminosities (see e.g. Unruh et al. 2020). In this section we show how the luminosity of a galaxy is affected by the Redshift Space Distortions and relativistic effects. Consider:

- A source with 4-velocity u_s^a that emits isotropically radiation in its rest frame $dE = L_s d\tau_s$ in a proper time τ_s, emitting photons of energy $(k_s u_o^a)|_\lambda$ (with λ the affine parameter). The number of photons emitted within a solid angle $\mathrm{d}\Omega_s$ is (Challinor and Lewis 2011)

$$\mathrm{d}N = \frac{L_S \, \mathrm{d}\tau_s \, \mathrm{d}\Omega_s}{4\pi \, (k_a u^a)|_\lambda}. \tag{2.41}$$

- An observer with 4-velocity u_o^a that collect the photons observed with energy $(k_a u_o^a)|_\lambda$ with a detector of area dA_o in time $d\tau_o$

The angles and areas are connected through the Jacobi relation $(1+z)^2 d\Omega_s dA_s = d\Omega_o dA_o$ ($dA_s = det\mathrm{D}_o d\Omega_o$ with D_0 the Jacobi map) (Challinor and Lewis 2011). The total energy received by A is then (Challinor and Lewis 2011)

$$\mathrm{d}E_\mathrm{o} = \left(k_\mu u^\mu\right)\big|_\mathrm{o} \, \mathrm{d}N = \frac{L_\mathrm{s} \mathrm{d}\tau_\mathrm{o} \mathrm{d}A_\mathrm{o}}{4\pi(1+z)^4 \det \mathscr{D}_\mathrm{o}}, \tag{2.42}$$

considering $d\tau_o/d\tau_s = 1+z$. The luminosity distance in an unperturbed space-time is given by (Dodelson 2003)

$$d_L = \sqrt{\frac{L}{4\pi F}} = (1+z)\chi, \tag{2.43}$$

but in the perturbed case (always at first order) it becomes (Bertacca 2015,Challinor and Lewis 2011)

$$d_L(\hat{n}) = (1+z)^2 \left(\det \mathscr{D}_0\right)^{1/2}. \tag{2.44}$$

The magnification is defined as (Jeong, Schmidt, and Hirata 2012, Borzyszkowski, Bertacca, and Porciani 2017)

$$\mathscr{M} = \left(\frac{d_\mathrm{L}}{\tilde{d}_\mathrm{L}}\right)^{-2}, \tag{2.45}$$

where $\tilde{d}_{\rm L}$ is the luminosity distance in a background unperturbed universe evaluated at the observed redshift of the galaxy. Note that in absence of perturbation $d_L = \bar{d}_L$ and so $\mathscr{M} = 1$. The full expression of the Jacobi map is obtained from the linear perturbation theory (Challinor and Lewis 2011), and we ends up with the final form of the Magnification (Borzyszkowski, Bertacca, and Porciani 2017)

$$\begin{aligned}\mathscr{M} = 1 - 2\left(1 - \frac{1}{\mathscr{H}\chi_{\rm s}}\right)\left[\psi_{\rm o} - \left(n^i_{\rm o} v_i\right)_{\rm o}\right] \\ + 2\left(1 - \frac{1}{\mathscr{H}\chi_{\rm s}}\right)\left[\int_0^{\chi_{\rm s}} \partial_0(\phi+\psi)\mathrm{d}\chi + \psi_{\rm e} - \left(n^i_{\rm s} v_i\right)_{\rm e}\right] \\ + 2\phi_{\rm e} - \frac{2}{\chi_{\rm e}}\int_0^{\chi_{\rm e}} (\phi+\psi)\mathrm{d}\chi + 2\kappa. \quad (2.46)\end{aligned}$$

As before even in the Magnification equation appear all the contributions from the peculiar velocities, lensing, Sachs-Wolfe effects and Shapiro time delay as expected.

2.3 LIGER method

There are two methods that can be used to create survey simulations that are able to accounts for the Redshift Space Distortions and relativistic effects: one is to create simulations of cosmic structure formation using equations consistently derived from general relativity, accounting in detail for the relativistic effects solving the geodesic equation for particles, taking into account the relativistic potentials (Adamek et al. 2016); another is to account for General Relativistic corrections *a posteriori*, meaning that we start from a Newtonian simulation and we then apply all the corrections. This is the method that we adopt in this thesis using the available code LIGER (Borzyszkowski, Bertacca, and Porciani 2017, Elkhashab, Porciani, and Bertacca 2021). This code

- Takes as input a very generic Newtonian simulation;
- Select some specific observer;
- It shifts all the positions of the galaxies in the Newtonian simulations accounting for all the Redshift Space Distortion and the general relativistic effects. It do this applying a coordinate system transformation that accounts for relativistic local and integrated along the Line Of Sight contributions. See section(2.2)
- As output it gives the distribution of the galaxies of each input simulation snapshot as they would be observed in our perturbed past light cone with the galaxies positions shifted considering the Redshift Space Distortion and the general relativistic effects selected. See section(3.3)

In this section we are going to show how LIGER, taking into account all the corrections as showed in the previous section, actually implement the displacements of the galaxies positions in practice. Since the aim is to understand how perturbations in the metric alter the null geodesic of the photons, the first step is to compute the gravitational potential in function of space and time starting from the particles distribution in the simulation. At a linear order in the perturbations the source equation for Ψ in the Poisson gauge for a pressure-less fluid in a ΛCDM universe can be written in terms of the matter density contrast in the synchronous comoving gauge δ_{syn} as the standard Poisson equation (see e.g. Chisari and Zaldarriaga 2011,Green and Wald 2012):

$$\Phi = \Psi = \phi, \tag{2.47}$$

$$\nabla^2\phi = 4\pi G a^2 \bar{\rho}_m \delta_{syn}, \tag{2.48}$$

$$v^i = v^i_{syn}. \tag{2.49}$$

with G the Newton's gravitational constant and $\bar{\rho}$ the matter density in the FRW background. Since $\delta_{syn} = \delta_{sim}$ (Borzyszkowski, Bertacca, and Porciani 2017) these equations can be written in terms of the matter density contrast of the simulation:

$$\Phi = \Psi = \phi, \tag{2.50}$$

$$\nabla^2\phi = 4\pi G a^2 \bar{\rho}_m \delta_{sim}, \tag{2.51}$$

$$v^i = v^i_{sim}. \tag{2.52}$$

The simulation is divided into snapshots and the gravitational potential (in each of them) is calculated starting from the simulation particle distribution calculating the matter density contrast on a regular Cartesian grid with the cloud in cell method (for a discussion on the particle assigment scheme see section(4.2.1)). The Poisson equation is then solved using a fast Fourier transform (see e.g. Duhamel and Vetterli 1990) obtaining the potential in function of space (depending on the position in the simulation) and in time (since it is solved for all the snapshots): $\phi(\mathbf{x}, t)$.

Once we know how the perturbed metric is written and how the gravitational potential evolves in space and time, we are able to apply the particles displacements of equations (2.46), (2.38), (2.39) and (2.40). Note that the effects in these equations give both local terms evaluated at a specific position and non-local terms (integrated terms). The integrals in the equations are computed along the line of sight and should be performed in Redshift space, where the path is a straight line, however since at linear order in the perturbation $|\phi| \ll 1$ (see e.g. Carlson, M. White, and N. Padmanabhan 2009) and the deflections are small, the integrals are performed in Real space from the observer position to the Redshift space position of the galaxy. Obviously not all the galaxies are shifted at the same moment, LIGER first identify the snapshots (so the time) in which a given galaxy would cross the backward light cone of the observer (in a FRW universe) and then the displacements are applied when the galaxy world line

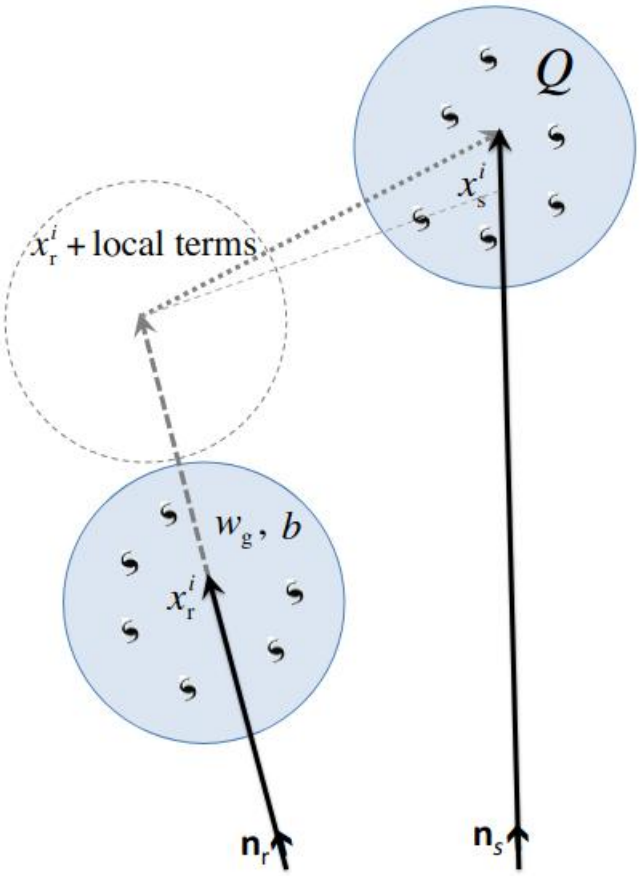

Figure 2.12: A scheme of how LIGER weight the particle shifts, accounting for both local and integrated terms. (Figure from Borzyszkowski, Bertacca, and Porciani 2017)

cross the observer past light cone. There are two main updates in the LIGER code from (Elkhashab, Porciani, and Bertacca 2021): the peculiar velocity and potential of the observe, that are the first term in equations (2.38) (2.39) (2.40) (2.46), are now taken into account while in the previous version they were neglected; and now the observer is associated with the closest simulation particle to the observer-selected location.

In figure(2.12) there is a simple scheme that shows how LIGER account for these two contributions: first the local terms are evaluated at the position of the galaxy and a first shift is applied, then the non-local terms are calculated through the integrals and a second shift is applied. However the transverse size of the light cone that intersect the worldline of the galaxies rapidly increase with redshift, requiring large simulations to cover the wide opening angle. This would create a problem for high mass resolution simulation, in which the computational time would drastically increases. This is

the reason why LIGER is able to apply the displacement directly to the dark matter particles in a simulation and compute the galaxy density field a posteriori, accounting for the galaxy bias. At linear order the matter density contrast in redshift space is (Borzyszkowski, Bertacca, and Porciani 2017)

$$\delta_s = \delta_{sim} + \delta_{RSD}, \tag{2.53}$$

where the term (see e.g. Yoo 2009b,Bonvin and Durrer 2011,Jeong, Schmidt, and Hirata 2012,Challinor and Lewis 2011)

$$\delta_{RSD} = \left(\frac{\partial_0 \mathscr{H}}{\mathscr{H}^2} + \frac{2}{\chi_s \mathscr{H}}\right) \delta \ln a + \psi_e - 2\phi_e + \frac{(\partial_0 \phi)_e}{\mathscr{H}} + 3\mathscr{H}\psi_v \tag{2.54}$$

$$- \frac{1}{\mathscr{H}} \left[n_s^i \partial_i \left(n_s^j v_j\right)\right]_e + \frac{2}{\chi_s} \int_0^{\chi_s} (\phi + \psi) \mathrm{d}\chi - 2\kappa, \tag{2.55}$$

collects all the corrections due to Redshift Space Distortions and relativistic effects. ϕ_v is the linear velocity potential at the galaxy position, $v_i = \partial_i \phi_v$ and the apparent redshift change due to the perturbations is

$$\delta \ln a = \psi_o - \left(n_s^i v_i\right)_o - \psi_e + \left(n_s^i v_i\right)_e - \int_0^{\chi_s} \partial_0 (\phi + \psi) \mathrm{d}\chi. \tag{2.56}$$

This equation is connected to the apparent redshift change (Borzyszkowski, Bertacca, and Porciani 2017)

$$\delta \ln a = \frac{\delta z}{(1+z)}, \tag{2.57}$$

and using equation(2.35) that shows how the redshift is perturbed, we ends up with the form in equation(2.56). As showed in (Challinor and Lewis 2011,Jeong, Schmidt, and Hirata 2012) instead the galaxy density contrast profile can be written in terms of three bias parameter

$$\delta_{g,s} = b\delta_{sim} + \mathscr{Q}(\mathscr{M} - 1) + \mathscr{E}\left(\delta \ln a - \mathscr{H}\phi_v\right) + \delta_{RSD}, \tag{2.58}$$

With

- The bias parameter b. At first order the intrinsic perturbation in the galaxy number density in real space is $\delta_{g,r} = b\delta_{sim}$;
- The Magnification-bias parameters that quantifies the impact of the Magnification.

$$\mathscr{Q} = - \left.\frac{\partial \ln \bar{n}_g}{\partial \ln L}\right|_{L=L_{lim}} \tag{2.59}$$

  Here $\bar{n}_g$ denotes the comoving number density of galaxies with luminosity higher than L. The Magnification factor appears for limited in flux survey with L_{lim} the limiting luminosity;

- The evolutionary-bias that accounts for the fact that the comoving number density of galaxies change with the redshift.

$$\mathscr{E} = -\frac{\partial \ln \bar{n}_{\rm g}}{\partial \ln(1+z)} \tag{2.60}$$

Assuming that: $|\mathscr{H}\psi_v \ll \delta lna|$, neglecting the velocity potential and using equation (2.53), we can write (Borzyszkowski, Bertacca, and Porciani 2017)

$$\delta_{\rm g,s} = (b-1)\delta_{\rm sim} + \delta_{\rm s} + \mathscr{E}\delta \ln a + \mathscr{Q}(\mathscr{M}-1). \tag{2.61}$$

To relate the galaxy over-density to the galaxy density in the simulations, we combine equations 2.53 and(2.58), then write the over-densities in terms of the number densities of the simulation, the final result for the galaxy number density is given by (Borzyszkowski, Bertacca, and Porciani 2017)

$$n_{g,s}(\hat{\mathbf{n}}_s,z) = [b(\bar{z})-1][w_g(\bar{z})n_{sim,r}(\hat{\mathbf{n}}_s,z) - \bar{n}_g(z)] + w_g(\bar{z})w_Q(\hat{\mathbf{n}}_s,z)n_{sim,s}(\hat{\mathbf{n}}_s,z), \tag{2.62}$$

where $n_{sim,r}$ is the real space number density, $n_{sim,s}$ the redshift space number density, $\bar{n}_{sim}$ is the simulation box averagre number density, $\bar{z} = z - \delta z$ the redhift perturbation, $w_Q = \mathscr{M}^{\mathscr{Q}}$ the magnification term and $w_g = \bar{n}_g/\bar{n}_{sim}$ denotes the mean number of galaxies per simulation particle at a given redshift. Each shift of the particle simulation are weighted by w_g. In order to estimate the matter density contrast starting from the particle in our N-body simulations, we use the standard mass weighted smoothing scheme (Elkhashab, Porciani, and Bertacca 2021)

$$1+\delta(\mathbf{x}) = \frac{\eta(\mathbf{x})}{\bar{\eta}} = \frac{1}{\bar{\eta}}\int \eta_{part}(\mathbf{y})W_{CIC}(\mathbf{x}-\mathbf{y})d^3y, \tag{2.63}$$

$$= \frac{1}{\bar{\eta}}\int \left[\sum_i \delta_D(\mathbf{y}_i-\mathbf{y})\right] W_{CIC}(\mathbf{x}-\mathbf{y})d^3y, \tag{2.64}$$

$$= \frac{1}{\bar{\eta}}\sum_i W_{CIC}(\mathbf{x}-\mathbf{y}_i), \tag{2.65}$$

where η, η_{part} and $\bar{\eta}$ are the smooth, discrete and average particle number density, respectively the index i runs over the simulation particles and W_{CIC} denotes the "cloud-in-cell" kernel (Hockney and Eastwood 1981). We use the real space particle position to get δ_{sim} and the redshift space ones to get δ_s. We sample the continuous fields δ_{sim} and δ_s on the same regular Cartesian grid that covers the past light cone of the observer.

Chapter 3

Quadratic estimator

3.1 Old Quadratic estimator

The quantity and quality of the data collected during a Survey are rapidly increasing (see e.g. Croom et al. 2021), so it is necessary to develop more and more accurate Power Spectrum estimator that can squeezing the most information possible from the observations. Here we review the Quadratic estimator for the Power Spectrum introducing a new version that is able to calculate un-windowed spectrum. The idea of Quadratic estimators is not new, it was already adopted in particular for CMB data-set analysis (see e.g. Max Tegmark, Blanton, et al. 2004, Max Tegmark, Dodelson, et al. 2002, M. Tegmark, A. J. S. Hamilton, and Xu 2002, A. J. S. Hamilton, Max Tegmark, and N. Padmanabhan 2000).

Let us parameterize the power spectrum $P(k)$ by some set of parameters grouped into a vector θ. Finding the values of the components of these vector would mean find the power spectrum $P(k)$. The standard approach to parameter estimation is to package our data set into a vector $\mathbf{x}$, and then write down the expression for the probability distribution $f(\mathbf{x};\theta)$ (Max Tegmark, Andrew J. S. Hamilton, et al. 1998). We interpret f as the probability distribution over θ given a data set $\mathbf{x}$. If we take $\mathbf{x}$ to be the measured coordinates of a set of N measured galaxies, the likelihood function f is unfortunately hopeless to compute numerically, since it involves the N -point correlation function. Even in the Gaussian approximation that is given by a product over two-point correlation functions (S. D. M. White 1979, Fry 1984), this requires evaluating a multivariate polynomial of degree $N/2$ in the correlations of the $N(N+1)/2$ galaxy pairs. The traditional approach has therefore been to take $\mathbf{x}$ to be something else: band-power estimates of the power spectrum. These are essentially computed by multiplying the observed density field by some weight function, Fourier transforming it, taking the squared modulus of the result and averaging over shells in k-space (Max Tegmark, Andrew J. S. Hamilton, et al. 1998). We follow this approach and so we divide the power spectrum

into "bins". The goal is to measure the band-power of each, that is, the value of the power spectrum into the specific k-range (bin). Thus the power spectrum is given by the value of each bins, collected into a vector $\mathbf{p} = [p_\alpha]$ in which each p_α is the band power of the bin with $k_\alpha < k < k_{\alpha+1}$, that means that we select the k-shell that refers to the vector $\mathbf{r}$.(Max Tegmark, Andrew J. S. Hamilton, et al. 1998). A general band power estimate p_α is a quadratic function of the generic density field $n(\mathbf{r})$ (Max Tegmark, Andrew J. S. Hamilton, et al. 1998):

$$p_\alpha = \int\int E_\alpha(\mathbf{r},\mathbf{r}')\frac{n(\mathbf{r})}{\bar{n}(\mathbf{r})}\frac{n(\mathbf{r}')}{\bar{n}(\mathbf{r}')}d\mathbf{r}d\mathbf{r}', \tag{3.1}$$

for some real-valued symmetric pair weighting matrix E_α that allows different ranges of pair of galaxies at r and $\mathbf{r}'$ to be weighted with different weight. Actually it can also to isolate different ranges of wavenumber k in Fourier space, if we simply do its Fourier transformation as showed in equation(3.9) The expected value of equation(3.1) is its average outcome. The expected value is found by calculating a weighted average of its possible outcomes (see e.g. Heath, Manolopoulou, and Baio 2015), so in expectation the band power becomes (Max Tegmark, Taylor, and Heavens 1997)

$$\langle p_\alpha\rangle = \int\int E_\alpha(\mathbf{r},\mathbf{r}')\frac{\langle n(\mathbf{r})}{\bar{n}(\mathbf{r})}\frac{n(\mathbf{r}')\rangle}{\bar{n}(\mathbf{r}')}, \tag{3.2}$$

Suppose we have a point process $n(r)$ which is a “Poisson sample” of some continuous stochastic field $1+\delta(r)$, that is, the probability that an infinitesimal volume element δV contains an object is $\bar{n}(r)[1+\delta(r)]\delta V$. Following Peebles (1980a) we describe the process by dividing the space into the infinitesimal micro-cells of volume δV which has a occupation numbers $n_i = 0$ or 1. That is, the statistical average of self-correlator for a given cell is (Jeong 2010)

$$\langle n_i^3\rangle = \langle n_i^2\rangle = \langle n_i\rangle = \bar{n}(\mathbf{r}_i)\delta V_i, \tag{3.3}$$

and the correlator for different cells are given by the underlying density contrast as (Jeong 2010)

$$\langle n_i n_j\rangle_{i\neq j} = \bar{n}(\mathbf{r}_i)\bar{n}(\mathbf{r}_j)\delta V_i\delta V_j[1+\langle\delta(\mathbf{r}_i)\delta(\mathbf{r}_j)\rangle], \tag{3.4}$$

and so equation(3.3) can be written as

$$\langle p_\alpha\rangle = \sum_{r\neq r'}\frac{E_\alpha(\mathbf{r},\mathbf{r}')}{\bar{n}(\mathbf{r})\bar{n}(\mathbf{r}')}[\bar{n}(\mathbf{r})\bar{n}(\mathbf{r}')\delta V_\mathbf{r}\delta V_{\mathbf{r}'}(1+\langle\delta(\mathbf{r})\delta(\mathbf{r}')\rangle] + \sum_{\mathbf{r}=\mathbf{r}'}\frac{E_\alpha(\mathbf{r},\mathbf{r}')}{\bar{n}(\mathbf{r})\bar{n}(\mathbf{r}')}\delta V_\mathbf{r}\bar{n}(\mathbf{r}')\delta_D(\mathbf{r}-\mathbf{r}'). \tag{3.5}$$

This because the assumption that we can describe the process dividing the volume into infinitesimal micro-cell, allows us to pass from integral on $\mathbf{r}$ to summation over the

micro volume δV, where equation(3.4) holds and so can be substituted, writing the expectation value in terms of summation over $\mathbf{r} \neq \mathbf{r}'$, but also over $\mathbf{r} = \mathbf{r}'$. Developing equation(3.5) we find

$$\langle p_\alpha \rangle = \sum_{r \neq r'} E_\alpha(\mathbf{r},\mathbf{r}')\delta V_{\mathbf{r}}\delta V_{\mathbf{r}'} + \sum_{r \neq r'} E_\alpha(\mathbf{r},\mathbf{r}')\delta V_{\mathbf{r}}\delta V_{\mathbf{r}'}\langle \delta(\mathbf{r})\delta(\mathbf{r}')\rangle + \sum_{\mathbf{r}=\mathbf{r}'} \frac{E_\alpha(\mathbf{r},\mathbf{r}')}{\bar{n}(\mathbf{r})}\delta V_{\mathbf{r}}\delta_D(\mathbf{r}-\mathbf{r}'), \tag{3.6}$$

and so writing everything another time in function of $\mathbf{r}$ as in Jeong (2010), it gives

$$\langle p_\alpha \rangle = \int\int E_\alpha(\mathbf{r},\mathbf{r}')d^3\mathbf{r}d^3\mathbf{r}' + \int\int E_\alpha(\mathbf{r},\mathbf{r}')\langle \delta(\mathbf{r})\delta(\mathbf{r}')\rangle d^3\mathbf{r}d^3\mathbf{r}' + \int \frac{E_\alpha(\mathbf{r},\mathbf{r}')}{\bar{n}(\mathbf{r})}d^3\mathbf{r}. \tag{3.7}$$

We see that the expectation value is given by the summation of a term that contains the average of the weight matrix all over the possible pair, one that account for the correlation function weighted by the matrix and the last one that as the typical behaviour of the Poissonian shot noise $1/\bar{n}(\mathbf{r})$. Writing everything in Fourier space we obtain the result obtained in Max Tegmark, Andrew J. S. Hamilton, et al. (1998)

$$\langle p_\alpha \rangle = W(0) + \int W_\alpha(k)P(k)\frac{d^3k}{(2\pi)^3} + b_\alpha. \tag{3.8}$$

The first term is the average of Fourier transform of the weight matrix all over the possible pairs and is connected to the mean density of the survey, the second contains the power spectrum convolved with the window function and the third is the Poissonian noise with its characteristic behaviour $1/\bar{n}(\mathbf{r})$. The three dimensional window function is given by (Max Tegmark, Andrew J. S. Hamilton, et al. 1998)

$$W_\alpha(\mathbf{k}) = \hat{E}_\alpha(\mathbf{k},\mathbf{k}') = \int E_\alpha(\mathbf{r},\mathbf{r}')e^{-i\mathbf{k}\cdot\mathbf{r}}e^{-i\mathbf{k}'\cdot\mathbf{r}'}d^3rd^3r', \tag{3.9}$$

that averaged over all possible directions gives the one dimensional window function:

$$W_\alpha(k) = k^2\int W_\alpha(\mathbf{k})d\Omega_k. \tag{3.10}$$

We interpret (3.8) as probing a weighted average of the power spectrum, with the window function giving the weights, that depends only on the separation between the direction $\mathbf{r}$ and $\mathbf{r}'$ (note that in the discrete case, as in galaxies surveys, the integral becomes summation over pairs of pixels). For the Quadratic Estimator of the power spectrum first we create a data vector $\mathbf{q}$ which elements are quadratic functions of the data vector $\mathbf{x}$ (Max Tegmark, Andrew J. S. Hamilton, et al. 1998)

$$q_\alpha = \frac{1}{2}(\mathbf{C}^{-1}\mathbf{x})^T\mathbf{C}_{,\alpha}\mathbf{C}^{-1}\mathbf{x},$$
$$q_\alpha = \frac{1}{2}\mathbf{x}^T\mathbf{E}_\alpha\mathbf{x},$$

with

$$\mathbf{E}_\alpha = \mathbf{C}^{-1}\mathbf{C}_{,\alpha}\mathbf{C}^{-1}, \tag{3.11}$$

the pair weighting function matrix, that is the derivative of the covariance matrix with respect to the normalization of the α^{th} band. For Gaussian distributed data the Fisher information matrix for $\mathbf{p}$ is (see e.g. Max Tegmark, Taylor, and Heavens 1997, Vogeley and Szalay 1996)

$$\mathbf{F}_{\alpha\beta} = -\left\langle \frac{\partial^2 lnf}{\partial\theta_i \partial\theta_j} \right\rangle = \frac{1}{2} tr[\mathbf{C}^{-1}\mathbf{C}_{,\alpha}\mathbf{C}^{-1}\mathbf{C}_{,\beta}], \tag{3.12}$$

and Kamionkowski, Kosowsky, and Stebbins (1997) showed that both the mean and the covariance of $\mathbf{q}$ are:

$$\langle \mathbf{q} \rangle = \mathbf{F}\mathbf{p}, \tag{3.13}$$

$$\langle \mathbf{q}\mathbf{q}^T \rangle - \langle \mathbf{q} \rangle \langle \mathbf{q} \rangle^T = \mathbf{F}, \tag{3.14}$$

and so an optimal Quadratic estimator of $\mathbf{p}$ is given by

$$\mathbf{p} = \mathbf{F}^{-1}\mathbf{q}, \tag{3.15}$$

since its covariance is precisely the inverse of the Fisher matrix (Max Tegmark, Andrew J. S. Hamilton, et al. 1998). This estimator is *lossless*, that means that it retains all the cosmological information that are inside the vector $\mathbf{x}$, but it gives a power spectrum convolved with the window function (Max Tegmark, Andrew J. S. Hamilton, et al. 1998). This is a problem because as showed by J. A. Peacock and Nicholson (1991) the window function alter the actual power spectrum, changing its amplitude and shape making it smoother at low k, as showed in figures(3.1)(3.2), where are plotted the power spectra for a full sky configuration of particle between redshift $z = (1.5, 1.8)$, adopting the cosmology in table(4.1). In figure(3.1) is plotted the predicted power spectra obtained with CAMB (Lewis and Bridle 2002), while the plots in figure(3.2) are obtained using equation(1.7). The window function depends on the actual geometry of a survey, so every power spectrum obtained by a survey data will be convolved with its specific window function. So how may we account for the fact that the power spectrum obtained has inside the window function of the survey?

One possibility could be convolve a theory model power spectrum with the same window function of the survey (see e.g. Percival et al. 2001), in order to make them comparable, since both are "affected" in the same manner, but this require an high computational cost, since the window function is given by the multiplication of the window function in the three dimensions $W(\mathbf{x}) = W(x_1)W(x_2)W(x_3)$ and this has to be done for each pair of pixels. Actually another possibility is to use an estimator that gives immediately the deconvolved power spectrum. This is the reason why we are going to present the Quadratic estimator from (O. Philcox 2020, O. H. E. Philcox 2021), that presented a method that allows directly the computation of the un-windowed power spectrum, avoiding the problem of deconvolving it or to convolve a theory model.

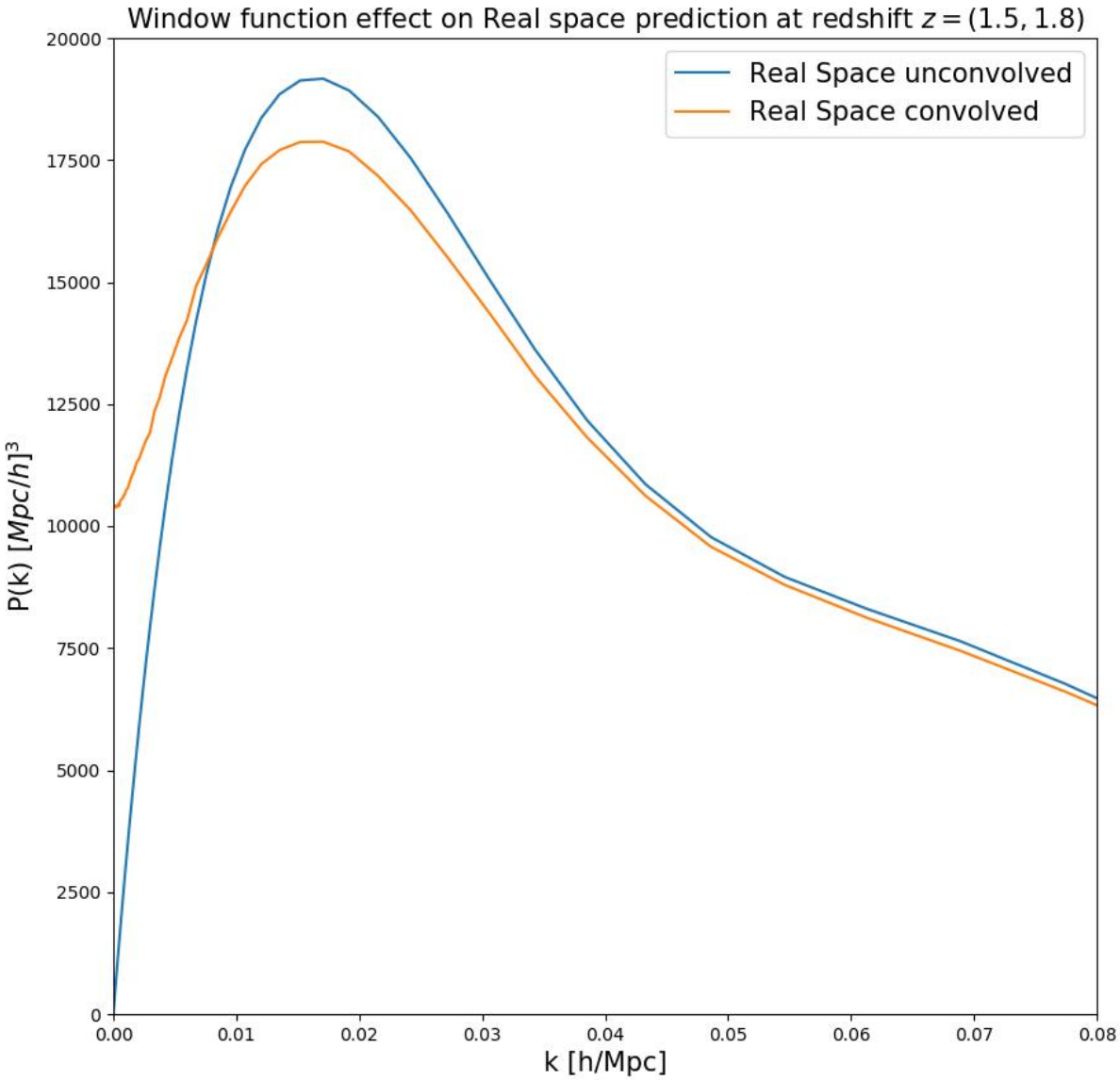

Figure 3.1: The plots shows how the window function affect the power spectrum in Real Space of a full sky particle configuration at redshift $z = (1.5, 1.8)$. The blue line is the un-convolved power spectrum, while the orange is the convolved one.

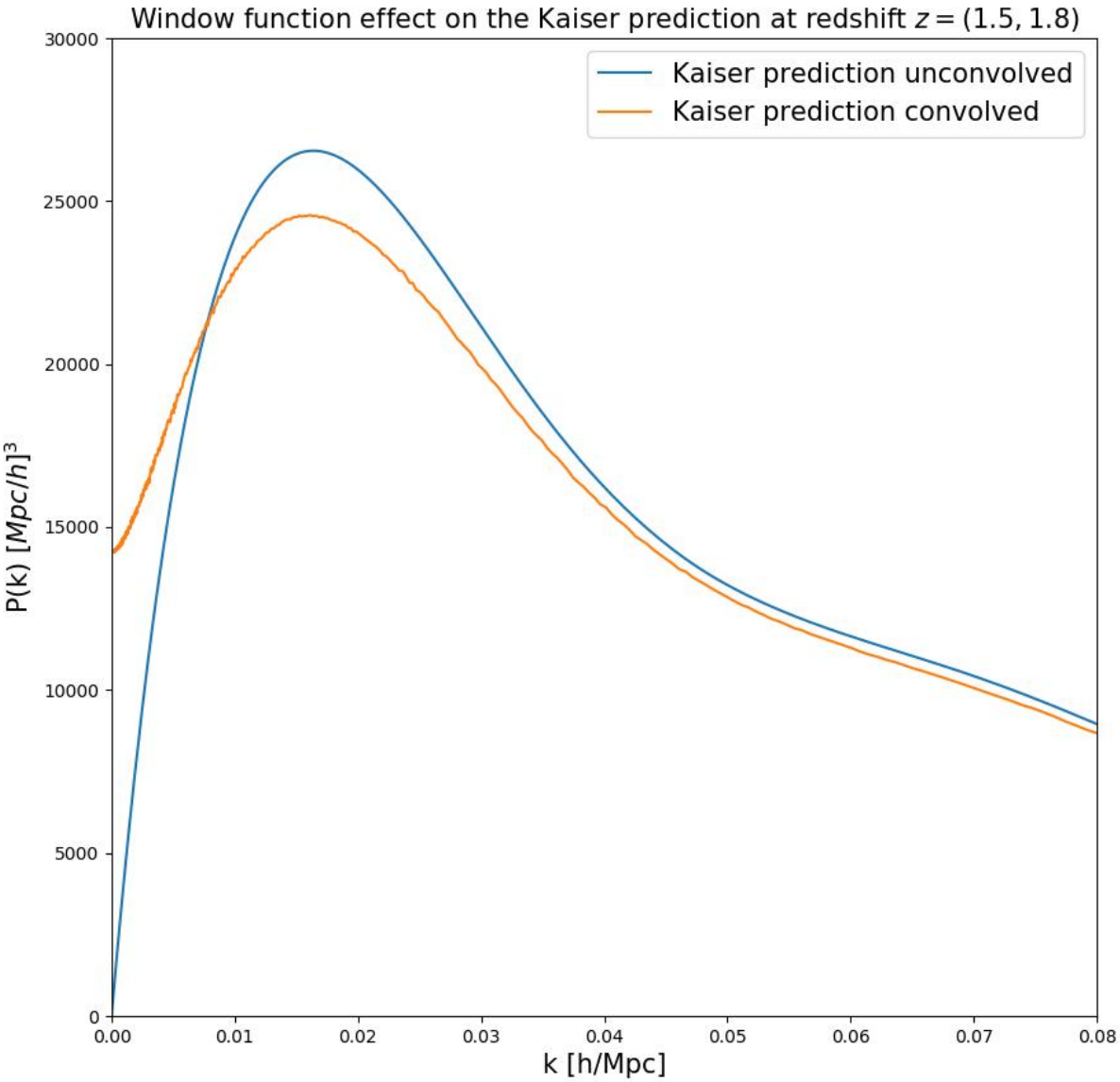

Figure 3.2: The plots shows how the window function affect the power spectrum of the Kaiser prediction of a full sky particle configuration at redshift $z = (1.5, 1.8)$. The blue line is the un-convolved power spectrum, while the orange is the convolved one.

3.2 New Quadratic estimator

In this section we apply the "new" Quadratic estimator (O. Philcox 2020,O. H. E. Philcox and Ivanov 2022) to galaxy survey simulations, so it's necessary to adopt a formalism that is suitable for this purpose. The simulation volume is divided into a grid and each grid cell is characterized by a vector $\mathbf{r}_\alpha$ that points to the centre of the α-th pixel. The data-set $\mathbf{d}$ is a vector which elements d_α are given by the subtraction of the galaxy density field n_g minus a random particle distribution density field n_r in each α-th cell as in Feldman, Kaiser, and John A. Peacock (1994) prescription.

$$d_\alpha = n_g(\mathbf{r}_\alpha) - \alpha n_r(\mathbf{r}_\alpha). \tag{3.16}$$

The galaxy and random densities are computed after some Mass Assignment Scheme (MAS) (see section(4.2.1) for details) and α is a normalization coefficient such that $\langle \mathbf{d} \rangle = 0$ (O. Philcox 2020), *i.e*

$$\alpha = \frac{\int d\mathbf{r} n_g(\mathbf{r})}{\int d\mathbf{r} n_r(\mathbf{r})}.$$

The vector $\mathbf{d}$ can be modeled as the sum of two contributions: a signal $\mathbf{m}$ contribution and a noise $\mathbf{n}$ contribution, that satisfy (assuming an uncorrelated noise from signal) (Max Tegmark, Andrew J. S. Hamilton, et al. 1998)

$$\langle \mathbf{d}\mathbf{d}^T \rangle = \mathbf{C} = \langle \mathbf{m}\mathbf{m}^T \rangle + \langle \mathbf{n}\mathbf{n}^T \rangle = \mathbf{S} + \mathbf{N}, \tag{3.17}$$

where $\mathbf{S}$ and $\mathbf{N}$ are respectively the signal and noise covariances. As for the "old" Quadratic estimator we can define a data-vector $\mathbf{q}$ which elements are quadratic functions of the data raw data vector $\mathbf{d}$ (O. Philcox 2020)

$$\hat{q}_\alpha^{QE} = \frac{1}{2}\mathbf{d}^T\mathbf{H}^{-1}\mathbf{C}_{,\alpha}\mathbf{H}^{-1}\mathbf{d} = \frac{1}{2}Tr[(\mathbf{H}^{-1}\mathbf{C}_{,\alpha}\mathbf{H}^{-1})\mathbf{d}\mathbf{d}^T], \tag{3.18}$$

where α is referred to the α-th bin, $\mathbf{C}_{,\alpha} = S_{,\alpha} = \partial\mathbf{S}/\partial p_\alpha$ is the derivative of the covariance with respect to the specific band-power of interest (it is equal to the derivative of the signal since the noise has not dependence on the band-power) and $\mathbf{H}$ is a general positive-defined-symmetric pixel weighting matrix. These two matrices are $N_{pix} \times N_{pix} \times N_{pix}$. Each element of the vector $\mathbf{q}$ is a quadratic functions of the data-set and contains a weighted average of the original data, with the weight given by $\mathbf{H}^{-1}$ and refers to a specific p_α according to the derivative term.

In expectation we have

$$\langle \hat{q}_\alpha^{QE} \rangle = \langle \frac{1}{2} Tr[(\mathbf{H}^{-1}\mathbf{C}_{,\alpha}\mathbf{H}^{-1})\mathbf{d}\mathbf{d}^T] \rangle \tag{3.19}$$

$$= \frac{1}{2} Tr[(\mathbf{H}^{-1}\mathbf{C}_{,\alpha}\mathbf{H}^{-1})\langle \mathbf{d}\mathbf{d}^T \rangle] \tag{3.20}$$

$$= \frac{1}{2} Tr[(\mathbf{H}^{-1}\mathbf{C}_{,\alpha}\mathbf{H}^{-1})\mathbf{C}] \tag{3.21}$$

$$= \frac{1}{2} Tr[(\mathbf{H}^{-1}\mathbf{C}_{,\alpha}\mathbf{H}^{-1})\mathbf{N}] + \frac{1}{2}\sum_\beta p_\beta Tr[\mathbf{H}^{-1}\mathbf{C}_{,\alpha}\mathbf{H}^{-1}\mathbf{C}_{,\beta}], \tag{3.22}$$

Assuming that $\mathbf{C} = \sum_\alpha p_\alpha \mathbf{C}_{,\alpha}$ and using equation(3.17).

Now we want to debias (3.19), so we need essentially two terms: one to be subtracted to cancel the first trace noise induced term (with the noise dependency) and the second to be multiplied to cancel the second trace term that contains the effect of the weighting matrix (and so of the window function).
So the general quadratic estimator is given by (inverting equation(3.19) to explicit p_β) (O. Philcox 2020)

$$\hat{p}_\alpha^{QE} = \sum_\beta F^{-1}_{\alpha\beta}(\hat{q}_\beta - \bar{q}_\beta), \tag{3.23}$$

with the multiplicative and subtracting terms (called Fisher and bias terms) given by:

$$F^{QE}_{\alpha\beta} = \frac{1}{2} Tr[\mathbf{H}^{-1}\mathbf{C}_{,\alpha}\mathbf{H}^{-1}\mathbf{C}_{,\beta}], \qquad \bar{q}_\alpha = \frac{1}{2} Tr[\mathbf{H}^{-1}\mathbf{C}_{,\alpha}\mathbf{H}^{-1}\mathbf{N}]. \tag{3.24}$$

This estimator is a difference between quantities measured in the actual data catalog and some uniformly distributed particle sample on which we calculate the Fisher and bias terms and since these terms contain the noise and window function effect, when they are subtracted they un-bias the estimator (It will be explained in details in the next section), so we are free from leading-order of pixelization, binning and non-Poissonian shot-noise, obtaining a power spectrum estimates that is not convolved with the window function, with the integral constrain isolated to the first k-bin. The general quadratic estimator is unbiased for all choices of symmetric and invertible pixel weighting matrix

H, since in expectation we have (dropping the "QE" index for brevity) (O. Philcox 2020)

$$\langle \hat{p}_\alpha \rangle = \sum_\beta F^{-1}_{\alpha\beta}(E[\hat{q}_\beta] - \bar{q}_\beta) = \sum_\beta F^{-1}_{\alpha\beta}\left(\frac{1}{2}Tr[\mathbf{H}^{-1}\mathbf{C}_{,\beta}\mathbf{H}^{-1}\mathbf{C}] - \bar{q}_\beta\right), \tag{3.25}$$

$$= \sum_\beta F^{-1}_{\alpha\beta}\left(\frac{1}{2}Tr[\mathbf{H}^{-1}\mathbf{C}_{,\beta}\mathbf{H}^{-1}\mathbf{N}] + \frac{1}{2}\sum_\gamma p_\gamma Tr[\mathbf{H}^{-1}\mathbf{C}_{,\beta}\mathbf{H}^{-1}\mathbf{C}_{,\gamma}] - \bar{q}_\beta\right), \tag{3.26}$$

$$= \sum_\beta F^{-1}_{\alpha\beta}\sum_\gamma p_\gamma F_{\gamma\beta}, \tag{3.27}$$

$$= \sum_\beta \sum_\gamma F^{-1}_{\alpha\beta} F_{\gamma\beta} p_\gamma, \tag{3.28}$$

$$= \sum_\gamma \delta^K_{\alpha\gamma} p_\gamma, \tag{3.29}$$

$$\langle \hat{p}_\alpha \rangle = p_\alpha. \tag{3.30}$$

so the expectation value is independent on the choice of the weight matrix **H**. The covariance matrix of **d** is given by (O. Philcox 2020)

$$\mathbf{C}_{\alpha\beta} = \mathbf{C}(\mathbf{r}_\alpha, \mathbf{r}_\beta) = \langle [n_g - \alpha n_r](\mathbf{r})[n_g - \alpha n_r](\mathbf{r}')\rangle, \tag{3.31}$$

$$= \langle n_g(\mathbf{r}) n_g(\mathbf{r}')\rangle - \alpha\langle n_g(\mathbf{r}) n_r(\mathbf{r}')\rangle - \alpha\langle n_r(\mathbf{r}) n_g(\mathbf{r}')\rangle + \tag{3.32}$$

$$\alpha^2\langle n_r(\mathbf{r}) n_r(\mathbf{r}')\rangle,$$

$$= \langle n_g(\mathbf{r}) n_g(\mathbf{r}')\rangle - 2\alpha\langle n_r(\mathbf{r}) n_g(\mathbf{r}')\rangle + \alpha^2\langle n_r(\mathbf{r}) n_r(\mathbf{r}')\rangle. \tag{3.33}$$

Assuming Poissonian statistic (Yamamoto, Nakamichi, et al. 2006)

$$\langle n_g(\mathbf{r}) n_g(\mathbf{r}')\rangle = n(\mathbf{r})n(\mathbf{r}')[1 + \xi(\mathbf{r}, \mathbf{r}')] + n(\mathbf{r})\delta(\mathbf{r} - \mathbf{r}'), \tag{3.34}$$

$$\langle n_r(\mathbf{r}) n_r(\mathbf{r}')\rangle = \alpha^{-2} n(\mathbf{r})n(\mathbf{r}') + \alpha^{-1} n(\mathbf{r})\delta_D(\mathbf{r} - \mathbf{r}'), \tag{3.35}$$

$$\langle n_r(\mathbf{r}) n_g(\mathbf{r}')\rangle = \alpha^{-1} n(\mathbf{r})n(\mathbf{r}'), \tag{3.36}$$

with $n(\mathbf{r}) = \alpha\langle n_r(\mathbf{r})\rangle = \langle n_g(\mathbf{r})\rangle$, we obtain

$$\mathbf{C}(\mathbf{r}_\alpha, \mathbf{r}_\beta) = n(\mathbf{r})n(\mathbf{r}')[1 + \xi(\mathbf{r}, \mathbf{r}')] + n(\mathbf{r})\delta(\mathbf{r} - \mathbf{r}') \\ - 2\alpha[\alpha^{-1} n(\mathbf{r})n(\mathbf{r}')] + \alpha^2[\alpha^{-2} n(\mathbf{r})n(\mathbf{r}') + \alpha^{-1} n(\mathbf{r})\delta_D(\mathbf{r} - \mathbf{r}')], \tag{3.37}$$

and finally

$$\mathbf{C}(\mathbf{r}_\alpha, \mathbf{r}_\beta) = n(\mathbf{r})n(\mathbf{r}')\xi(\mathbf{r}, \mathbf{r}') + (1 + \alpha)n(\mathbf{r})\delta_D(\mathbf{r} - \mathbf{r}') = \mathbf{S}(\mathbf{r}, \mathbf{r}') + \mathbf{N}(\mathbf{r}, \mathbf{r}'), \tag{3.38}$$

where we assume that the galaxy density field can be written as $n_g(\mathbf{r}) = n(\mathbf{r})[1 + \delta(\mathbf{r})]$ with $\delta(\mathbf{r})$ the overdensity w.r.t. the mean density, which has the correlation function

$\xi(\mathbf{r},\mathbf{r}') = \langle\delta(\mathbf{r})\delta(\mathbf{r}')\rangle$, ignoring the effect of pixellization since already considered in the estimator (3.23). Considering a signal-uncorrelated noise, also for the "new" Quadratic code the covariance is given by the sum of the two contribution. Writing the correlation function in Fourier-space expanding in multipoles via the legendre polynomial $P(k,\hat{\mathbf{k}}\cdot\hat{\mathbf{r}}') = \sum P_l(k)L_l(\hat{\mathbf{r}}')$ it gives (denoting $\int_{\mathbf{k}} = (2\pi)^{-3}\int d\mathbf{k}$):

$$C\left(\mathbf{r},\mathbf{r}'\right) = n(\mathbf{r})n\left(\mathbf{r}'\right)\int_{\mathbf{k}} e^{i\mathbf{k}\cdot(\mathbf{r}-\mathbf{r}')}\sum_{\ell} P_\ell(k)L_\ell\left(\hat{\mathbf{k}}\cdot\hat{\mathbf{r}}'\right) + (1+\alpha)n(\mathbf{r})\delta_D\left(\mathbf{r}-\mathbf{r}'\right), \quad (3.39)$$

always divided in the signal+noise contribution. Assuming $P_l(k) = \sum_a \Theta_a(\mathbf{k})P_l^a$ for some k-bins with bin weight $\Theta^a(\mathbf{k}) = 1$ if $\mathbf{k}$ is inside $|\mathbf{k}|$-bin a and zero else, is straightforward to find the derivative of the covariance w.r.t. a specific band-power

$$C_{,\alpha}\left(\mathbf{r},\mathbf{r}'\right) = n(\mathbf{r})n\left(\mathbf{r}'\right)\int_{\mathbf{k}} e^{i\mathbf{k}\cdot(\mathbf{r}-\mathbf{r}')}\Theta_a(\mathbf{k})L_\ell\left(\hat{\mathbf{k}}\cdot\hat{\mathbf{r}}'\right), \quad (3.40)$$

where α refers to a $[a,l]$ pair. These formulae allow the computation of the $\mathbf{p}$ vector, depending on which choice of $\mathbf{H}$ one assume. In the next section we will present two possible choices for the weight matrix $\mathbf{H}$.

3.2.1 Maximum Likelihood estimator

Assuming Gaussian distributed data with $\langle\mathbf{d}\rangle = 0$, the (gaussian) log-likelihood can be written as (Elsner and Wandelt 2012)

$$\mathscr{L}[\mathbf{d}](\mathbf{p}) = -2\log L[\mathbf{d}](\mathbf{p}) = \mathbf{d}^T\mathbf{C}^{-1}(\mathbf{p})\mathbf{d} + \mathrm{Tr}\log\mathbf{C}(\mathbf{p}) + \text{ const. }. \quad (3.41)$$

Supposing to have a fiducial Power Spectrum, we expand equation(3.41) around the fiducial band Power Spectrum vector around a fiducial spectrum $\mathbf{p}^{\rm fid}$

$$\mathscr{L}\left(\mathbf{p}^{\rm fid} + \delta\mathbf{p}\right) \approx \mathscr{L}\left(\mathbf{p}^{\rm fid}\right) + \delta\mathbf{p}^T\nabla_{\mathbf{p}}\mathscr{L} + \frac{1}{2}\delta\mathbf{p}^T\left(\nabla_{\mathbf{p}}\nabla_{\mathbf{p}'}\mathscr{L}\right)\delta\mathbf{p}', \quad (3.42)$$

where $\delta\mathbf{p} = \mathbf{p} - \mathbf{p}^{\rm fid}$. Assuming $\mathbf{p}^{\rm fid}$ is sufficiently close to the true spectrum (such that $\mathbf{C}_{\rm fid} \approx C_D$), $\delta\mathbf{p}$ can be estimated by minimizing (3.42) (Young 2019)

$$\nabla_{\mathbf{p}}\mathscr{L}(\mathbf{p}^{\rm fid} + \delta\mathbf{p}) = 0, \quad (3.43)$$

and it gives (O. Philcox 2020):

$$\delta\mathbf{p} = -[\nabla_{\mathbf{p}}\nabla_{\mathbf{p}'}\mathscr{L}]^{-1}\nabla_{\mathbf{p}'}\mathscr{L}, \quad (3.44)$$

so inserting it in the Gaussian likelihood we obtain the the maximum-likelihood estimator for a band-power p_α;

$$\hat{p}_\alpha - p_\alpha^{fid} = -\left[\frac{\partial^2 \mathscr{L}}{\partial p_\alpha \partial p_\beta}\right]^{-1}\left(\frac{\partial \mathscr{L}}{\partial p_\alpha}\right), \tag{3.45}$$

$$\hat{p}_\alpha^{\rm ML} = p_\alpha^{\rm fid} + \frac{1}{2}\sum_\beta \left[\frac{1}{2} Tr[\mathbf{C}_{\rm fid}^{-1}\mathbf{C}_{,\alpha}\mathbf{C}_{\rm fid}^{-1}\mathbf{C}_{,\beta}]\right]^{-1}(\mathbf{d}^T\mathbf{C}^{-1}\mathbf{C}_{,\beta}\mathbf{C}_{\rm fid}^{-1}\mathbf{d} - Tr[\mathbf{C}_{\rm fid}^{-1}\mathbf{C}_{,\beta}]), \tag{3.46}$$

$$\hat{p}_\alpha^{\rm ML} = p_\alpha^{\rm fid} + \sum_\beta F_{\alpha\beta}^{-1}\left(\hat{q}_\beta - \bar{q}_\beta\right). \tag{3.47}$$

This is just a special case of the general quadratic estimator, with $\mathbf{H}$ equal to the Covariance matrix in the fiducial cosmology $\mathbf{C}_{\rm fid}$. If $\mathbf{C}_{\rm fid}$ is equal to the true data covariance $\mathbf{C}$, i.e. $\mathbf{p}^{\rm fid} = \mathbf{p}$ and the underlying density field is Gaussian, the ML solution is optimal in the sense that it saturates the Cramér-Rao relation. In this case, the covariance of $\hat{p}_\alpha$ is simply the inverse Fisher matrix $F_{\alpha\beta}^{-1}$ and this feature is called optimality.

Under these ipothesis we show that the ML is an optimal estimator, beginning fom the definition of the Cramèr-Rao theorem, that states that if an estimator $\hat{p}_\alpha$ is optimal it must satisfy (Max Tegmark, Taylor, and Heavens 1997)

$$\mathrm{cov}\left(\hat{p}_\alpha, \hat{p}_\beta\right)\big|_{\rm CR\ bound} = \left\langle \frac{1}{2}\frac{\partial^2 \mathscr{L}[\mathbf{d}](\mathbf{p})}{\partial p_\alpha \partial p_\beta}\right\rangle^{-1} \equiv \mathscr{I}_{\alpha\beta}^{-1}, \tag{3.48}$$

where the right-hand-side is the inverse Fisher information for negative log-likelihood $\mathscr{L}[\mathbf{d}](\mathbf{p}) = -2\log L[\mathbf{d}](\mathbf{p})$ depending on parameters $\mathbf{p}$ and data $\mathbf{d}$. Assuming the Gaussian likelihood of (3.41), evaluated at the true covariance $\mathbf{C}$, the Fisher information is straightforwardly derived;

$$\mathscr{I}_{\alpha\beta} = \left\langle \frac{1}{2}\mathrm{Tr}\left[\mathrm{C}^{-1}\mathrm{C}_{,\alpha}\mathrm{C}^{-1}\mathrm{C}_{,\beta}\mathrm{C}^{-1}\left(2\mathrm{dd}^T - \mathrm{C}\right)\right]\right\rangle, \tag{3.49}$$

$$\mathscr{I}_{\alpha\beta} = \frac{1}{2}\mathrm{Tr}\left[\mathrm{C}^{-1}\mathrm{C}_{,\alpha}\mathrm{C}^{-1}\mathrm{C}_{,\beta}\mathrm{C}^{-1}\left(2\langle\mathrm{dd}^T\rangle - \mathrm{C}\right)\right], \tag{3.50}$$

$$\mathscr{I}_{\alpha\beta} = \frac{1}{2}\mathrm{Tr}\left[\mathrm{C}^{-1}\mathrm{C}_{,\alpha}\mathrm{C}^{-1}\mathrm{C}_{,\beta}\right] = \mathrm{C} \equiv F_{\alpha\beta}. \tag{3.51}$$

The ML estimator of equation(3.45) saturates its Cramér-Rao bound. Another very important observation that can be made is that $\mathrm{cov}\left(\hat{p}_\alpha, \hat{p}_\beta\right) = F_{\alpha\beta}^{-1}$ implies also that the ML estimator is lossless. This imply that all the cosmological information contained in the simulation and thus in the data-set, is completely transferred in the compressed $\mathbf{q}$ vector and the estimator of equation(3.45) retain all the information contained in this vector, transferring it to the band-powers estimates and so giving the minimal error bars possibles in the subsequently parameters inference (Max Tegmark, Andrew J. S. Hamilton, et al. 1998).

3.2.2 FKP like matrix

To calculate the Power spectrum in the FKP prescription the galaxies are weighted according to the weighting matrix (Feldman, Kaiser, and John A. Peacock 1994) $\omega(\mathbf{r}) = 1/(1+\bar{n}(\mathbf{r})P(k))$, with $P(k)$ a constant power spectrum and $\bar{n}(\mathbf{r})$ some mean density field varying in space. This weight in the extreme cases:

- when $\mathbf{r} \gg 1$, $\bar{n}(\mathbf{r})$ is large so the number of galaxies per cell volume is huge, so is convenient to give equal weight per volume, or equivalently, to weight galaxy in proportion to $1/\bar{n}(\mathbf{r})$) since the error is dominated by the finite number of the volume cells;
- when $\mathbf{r} \ll 1$, $\bar{n}(\mathbf{r})$ decreases rapidly, thus the number of galaxies per volume is low and so the dominant error is the Poissonian one and so is optimal to weight the galaxies equally.

In our approach we use the slightly modified FKP weighting matrix (O. Philcox 2020)

$$\mathrm{H}_{\mathrm{FKP}}\left(\mathbf{r},\mathbf{r}'\right) = n(\mathbf{r})n\left(\mathbf{r}'\right)P_{\mathrm{FKP}}\delta_D\left(\mathbf{r}-\mathbf{r}'\right) + n(\mathbf{r})\delta_D\left(\mathbf{r}-\mathbf{r}'\right), \tag{3.52}$$

and inverting we find the $\mathbf{H}$ matrix for the FKP like approach:

$$\mathrm{H}^{-1}_{\mathrm{FKP}}\left(\mathbf{r},\mathbf{r}'\right) = \frac{1}{n(\mathbf{r})\left[1+n(\mathbf{r})P_{\mathrm{FKP}}\right]}\delta_D\left(\mathbf{r}-\mathbf{r}'\right). \tag{3.53}$$

Note that this is not identical to the conventional FKP scheme. Our formalism applies the weight to the grid directly rather than the particles, and normalizes by $n(\mathbf{r})$ rather than some survey-averaged quantity; this is necessary to ensure that we recover the unwindowed power spectrum estimates (O. Philcox 2020).

3.3 The algorithm

We now present how the algorithm works in practice, showing the difference of the procedure using the Maximum Likelihood $\mathbf{H}^{-1} = \mathbf{C}^{-1}_{\mathrm{FID}}$, and using the FKP like weight matrix $\mathbf{H}^{-1} = \mathbf{H}^{-1}_{\mathrm{FKP}}$.

3.3.1 Matrices inversion

The most intensive step of the algorithm is to compute Fisher and Bias terms of (3.24). The non trivial part is to calculate $\mathbf{C}^{-1}_{\mathrm{fid}}$ considering that this would imply an inversion of a N^3_{pix}, so a full form and storage of it is infeasible. Instead of calculating their full form, rather we calculate their action on a generic pixelized field $x(\mathbf{r})$.

$$C[x](\mathbf{r}) \equiv \int d\mathbf{r}'\mathbf{C}\left(\mathbf{r},\mathbf{r}'\right)x\left(\mathbf{r}'\right), \tag{3.54}$$

and using the definition given in equation(3.39) for spectroscopic surveys

$$C[x](\mathbf{r}) = n(\mathbf{r}) \int_{\mathbf{k}} e^{i\mathbf{k}\cdot\mathbf{r}} \int d\mathbf{r}' e^{-i\mathbf{k}\cdot\mathbf{r}'} n\left(\mathbf{r}'\right) x\left(\mathbf{r}'\right) \sum_{\ell} P_\ell(k) L_\ell\left(\hat{\mathbf{k}}\cdot\hat{\mathbf{r}}'\right) + (1+\alpha) n(\mathbf{r}) x(\mathbf{r}), \tag{3.55}$$

with $P_l(k)$ is the fiducial Power Spectrum multipoles generated from some fiducial simulations with known cosmology. Expanding L_ℓ via spherical harmonic as in (Yamamoto, Nakamichi, et al. 2006) we obtain

$$\begin{aligned} C[x](\mathbf{r}) &= n(\mathbf{r}) \sum_{\ell} \frac{4\pi}{2\ell+1} \sum_{m=-\ell}^{\ell} \int_{\mathbf{k}} P_\ell(k) e^{i\mathbf{k}\cdot\mathbf{r}} Y^*_{\ell m}(\hat{\mathbf{k}}) \int d\mathbf{r}' Y_{\ell m}\left(\mathbf{r}'\right) n\left(\mathbf{r}'\right) x\left(\mathbf{r}'\right) e^{-i\mathbf{k}\cdot\mathbf{r}'} \\ &\quad + (1+\alpha) n(\mathbf{r}) x(\mathbf{r}), \end{aligned} \tag{3.56}$$

$$= n(\mathbf{r}) \sum_{\ell} \frac{4\pi}{2\ell+1} \sum_{m=-\ell}^{\ell} \mathscr{F}^{-1}\left[P_\ell(k) Y^*_{\ell m}(\hat{\mathbf{k}}) \mathscr{F}\left[Y_{\ell m} n x\right](\mathbf{k})\right](\mathbf{r}) + (1+\alpha) n(\mathbf{r}) x(\mathbf{r}). \tag{3.57}$$

Practically using this formalism the action of the fiducial covariance on a generic density field is simply a summation of a limited number of Fast Fourier transformation (hereafter FFT), specifically $\frac{1}{2}(1+\ell_{\max})(2+\ell_{\max})$ real-to-Fourier FFT's using the real form of the spherical harmonics as in (Hand et al. 2017) that assumes that the fiducial spectra are non zero for all even ℓ up to $\ell_{\max}$. Giving the definition in equation(3.56) is straightforward to find the expression of its derivative

$$\mathbf{C}_{,\alpha}[x](\mathbf{r}) = n(\mathbf{r}) \frac{4\pi}{2\ell+1} \sum_{m=-\ell}^{\ell} \mathscr{F}^{-1}\left[\Theta_a(\mathbf{k}) Y^*_{\ell m}(\hat{\mathbf{k}}) \mathscr{F}\left[Y_{\ell m} n x\right](\mathbf{k})\right](\mathbf{r}). \tag{3.58}$$

As before it is simply a summation of $(2\ell+1)$ FFT's. Note that equation(3.58) is equal both for the Maximum Likelihood method and for the FKP like (it appears in the Fisher and Bias terms for both), this is why we dropped the fid subscription. The next step is to invert the matrix and find $\mathbf{C}^{-1}_{\text{fid}}$ and $\mathbf{H}^{-1}_{FKP}$ and now we have to distinguish between the two methods.

3.3.1.1 Maximum Likelihood estimator

Assuming that the data distribution and the underlying density field are Gaussian the likelihood distribution of the data is

$$\mathscr{L}[\mathbf{d}](\mathbf{p}) = -2\log L[\mathbf{d}](\mathbf{p}) = \mathbf{d}^T \mathbf{C}^{-1}_{\text{fid}}(\mathbf{p})\mathbf{d} + \operatorname{Tr}\log \mathbf{C}_{\text{fid}}(\mathbf{p}) + \text{ const. }. \tag{3.59}$$

In the standard practice if we want to adopt the Maximum Likelihood estimator we need a set of simulations ran with known cosmology, in order to find the fiducial covariance matrix. In the Maximum Likelihood estimator doesn't appear $\mathbf{C}_{\text{fid}}$, but rather it's

inverse, so we calculate the action of the inverse of the covariance matrix on a generic field $\mathbf{C}_{\rm fid}^{-1}\mathbf{d}$ instead of its complete form. The algorithm uses a preconditioned conjugate-gradient descent method (hereafter CGD) as in Oh, Spergel, and Hinshaw (1999). We want to numerically solve a generic problem written as $\mathbf{C}_{\rm fid}^{-1}\mathbf{x} = \mathbf{y}$ where $\mathbf{x}$ is a generic field, but we don't know the full form of the matrix. So we multiplying this equation for $\mathbf{C}_{\rm fid}$

$$\mathbf{C}_{\rm fid}\mathbf{C}_{\rm fid}^{-1}\mathbf{x} = \mathbf{C}_{\rm fid}\mathbf{y}, \tag{3.60}$$

and then for some "preconditioner matrix" $\tilde{\mathbf{C}}$:

$$\tilde{\mathbf{C}}^{-1}\mathbf{x} = \tilde{\mathbf{C}}^{-1}\mathbf{C}_{\rm fid}\mathbf{y}. \tag{3.61}$$

$\mathbf{y}$ is found through repeating application of $\mathbf{C}_{\rm fid}$ to data, possible via equation(3.39). Convergence depends strongly on the choice of $\tilde{\mathbf{C}}$ and require that it is easily inverted and close to $\mathbf{C}_{\rm fid}$, such that $\tilde{\mathbf{C}}^{-1}\mathbf{C}_{\rm fid}^{-1} = \mathbb{1} + \mathbf{R}$ with all the Eingevalues of $\mathbf{R}$ are less than one. As preconditioner matrix the algorithm uses

$$\tilde{\mathbf{C}}(\mathbf{r},\mathbf{r}') = \mathbf{H}_{FKP}(\mathbf{r},\mathbf{r}') = n(\mathbf{r})[1 + n(\mathbf{r})P_{FKP}]\delta_D(\mathbf{r}-\mathbf{r}'), \tag{3.62}$$

with $P_{FKP} = 10^4 h^{-3}\mathrm{Mpc}^3$. This is a computationally expensive step since it requires $\frac{1}{2}N_{it}(1+\ell_{\rm max})(2+\ell_{\rm max})$ steps.

3.3.1.2 FKP like matrix

This case is much simpler, since as we saw the FKP like matrix is a diagonal matrix (3.52), so it is straightforwardly inverted

$$\mathbf{H}_{FKP}^{-1}[x](\mathbf{r}) = \frac{x(\mathbf{r})}{n(\mathbf{r})[1 + n(\mathbf{r})P_{FKP}]} \tag{3.63}$$

requiring a simple division in configuration space. $n(\mathbf{r})$ is always positive defined, avoiding the possibility of some infinite value.

3.3.2 Calculating Bias and Fisher terms

In this subsection we show how to compute in practice the Fisher and Bias term. This step is common to both method, with the only difference that is in the $\mathbf{H}$ matrix choice. We create an uniformly distributed particle sample painting it in a box that has the same box volume and grid division of our galaxy simulation catalog, utilizing the same Mass Assigment Scheme. After having chosen a value for the background density in this "toy" box, we compute the difference between the painted sample and the uniform background in each cell, obtaining the $\mathbf{m}$ vector, that is a list which elements contains the difference values of each cell as we do for the actual galaxy and random catalogs.

This is our "toy-simulation" on which we are going to calculate the Bias and fisher terms as is showed below. The fundamental aspect is that the Fisher and Bias terms are calculated on this "toy" simulation, because this allow the Fisher and Noise matrices to be written as expectation values of a pairs of vectors, the only requirement is that the inverse covariance of this "toy" catalog has to be precisely known and is for this reason that a uniform catalog is used. These quantities contains the $\mathbf{H}^{-1}$ and $\mathbf{C}_{,\alpha}$ matrices that contain the "window function effect", and so if they are subtracted, a unbiased estimator is recovered as already showed. In practice the Fisher and Bias terms are calculating creating each time a new data vector $\mathbf{m}$ and calculating the bias and fisher terms on each Monte Carlo realization and then doing an average on all the realizations of this "toy catalog", before being subtracted.

First we rewrite the terms in a separable form expliciting the random fields $\mathbf{m}$:

$$2F^{QE}_{\alpha\beta} = \langle \mathbf{m}^T \mathbf{H}^{-1} \mathbf{C}_{,\alpha} \mathbf{H}^{-1} \mathbf{C}_{,\beta} \mathbf{A}^{-1} \mathbf{m} \rangle \qquad 2\bar{q}_\alpha = \langle \mathbf{m}^T \mathbf{H}^{-1} \mathbf{C}_{,\alpha} \mathbf{H}^{-1} \mathbf{N} \mathbf{A}^{-1} \mathbf{m} \rangle \quad (3.64)$$

This is true for any invertible matrix $\mathbf{A}$ such that $\mathbf{A} = \langle \mathbf{m}\mathbf{m}^T \rangle$ and in fact this is the condition that the uniformly distributed particle sample has to fullfill.

- In each simulation (denoted as $\mathbf{m}$) the terms are so computed:
  - Compute:
    - $\mathbf{H}^{-1}\mathbf{m}$ applied to the map via preconditioned CGD using (3.56) for the Maximum Likelihood estimator or simply using the analytic form for the FKP like matrix,
    - compute $\mathbf{N}\mathbf{A}^{-1}\mathbf{m}$ applied to the map.
  - For each band-power α:
    - Compute $\mathbf{y}_\alpha = \mathrm{C}_{,\alpha} \left[\mathbf{H}^{-1}\mathbf{m} \right]$ via (3.58);
    - Accumulate the bias contribution $\frac{1}{2} \left(\mathbf{H}^{-1}\mathbf{m} \right)^T \mathbf{y}_\alpha \mathbf{N}\mathbf{A}^{-1}\mathbf{m}$;
    - Compute $\mathbf{y}_\beta = \mathbf{C}_{,\beta}\mathbf{A}^{-1}\mathbf{m}$
    - Accumulate the Fisher matrix contribution $\frac{1}{2}\mathbf{y}_\alpha^T \mathbf{H}^{-1} \left[\mathbf{y}_\beta \right]$ from each choice of β.

3.3.3 Accumulating the estimator

As last step we compute the band-powers estimations equation(3.18) or equation(3.45), depending on choice of the weighting matrix, utilizing the Fisher and Bias terms obtained in the last step. This part is only matrices operations.

Chapter 4

Results

4.1 The catalog

In this chapter we are going to presents the results of our analysis. First we present how the catalogs are computed, then we discuss how we implemented our analysis with the quadratic code and at the end the obtained spectra. The catalogs are created in the following way:

- CAMB (Lewis and Bridle 2002) is used to produce the initial power spectrum, considering as cosmological parameters the ones from the Planck 2018 collaboration (N. Aghanim et al. 2020) as showed in table(4.1)

Ω_m	Ω_b	Ω_Λ	h	n_s
0.31724	0.05081	0.68560	0.67	0.97

Table 4.1: Cosmological parameters used to compute the initial power spectrum, from Planck 2018 collaboration (N. Aghanim et al. 2020)

- The Dark Matter simulations are ran starting from the computed initial power spectrum using the MUSIC code (Hahn and Abel 2011). The method uses an adaptive convolution of Gaussian white noise with a real space transfer function kernel together with an adaptive multi-grid Poisson solver to generate displacements and velocities following second order Lagrangian perturbation theory (2LPT). The new algorithm achieves relative errors of order 10^{-4} for displacements and velocities in the refinement region and thus improves in terms of errors by about two orders of magnitude over previous approaches. In addition, errors are localized at coarse-fine boundaries and do not suffer from Fourier-space induced interference ringing. This code uses a second-order Lagrangian perturbation theory (2LPT) for large scale dynamics, while small scales are solved with a

particle mesh (PM) algorithm. The 2LPT basically write the particle positions as $\mathbf{x} = \mathbf{q} + \Psi$ with $\mathbf{x}$ the initial position, $\mathbf{q}$ the final position and Ψ a displacement vector. The displacement vector Ψ is expanded at second order $\Psi = \Psi^{(1)} + \Psi^{(2)} + ...$, so the equation of motions can be written as (Scoccimarro 1998, Buchert 1994)

$$\nabla \cdot \Psi^{(1)} = -D_1 \delta_L(\mathbf{q}) \quad \nabla \cdot \Psi^{(2)} = \frac{1}{2} D_2 \sum_{1 \neq j} (\Psi^{(1)}_{i,i} \Psi^{(1)}_{j,j} - \Psi^{(1)}_{i,j} \Psi^{(1)}_{j,i}) \tag{4.1}$$

where $\Psi^{(1)}_{i,j} = \partial \Psi_i / \partial \Psi_j$ and $D_2 \approx -3/7 D_1^2 \Omega_m^{-1/143}$ (Buchert 1994) the second order grow factor for a flat universe with non-zero cosmological constant. So the particles position is obtained in each snapshot as $\mathbf{x} = \mathbf{q} - D_1 \Psi^{(1)} + D_2 \Psi^{(2)}$.

- The galactic densities are built using the equation(2.62), then each cells is multiplied by it's grid volume to get the number counts, since we are multiplying a density for a volume. The shot noise is added by sampling each cell, so in this way each cell i ends up with n_i galaxies. Finally in each cell are randomly assigned N_i galaxies coordinates. For the random catalogue instead is computed the average background density for the galaxy distribution, then it is integrated with redshift to compute the density distribution. Basically we got the average number density and then we compute the cumulative number counts, so we go from $n_g(z)$ to $N_g(z)$ and then we sample the function $P_(z) = int_0^z N_{G(z)}$ to create the random catalog. We keep adding random galaxies till the total number of random particles is equal to 5 times the total number of galaxies.

- LIGER is applied to the simulations in order to create catalogs with the particle positions shifted as described in chapter(2). As described it takes in input the Newtonian Dark matter simulations and gives as output the simulation with the particles shifted. As showed in section(3.3) it computes the potential in each snapshot solving the Poisson equation in Fourier space

$$-k^2 \phi(\mathbf{k}) = 4\pi G \bar{\rho} \delta, \tag{4.2}$$

where the overdensities are computed on a cartesian grid using the cloud in cell particle interpolation, ϕ is the computed potential and $\bar{\rho}$ the mean density. As presented in section(3.3) it doesn't applies all the shifts at the same time, but rather it first identify the snapshots within which a given galaxy would cross the backward light cone of the observer in the absence of metric perurbations and then calculates and apply the redshift-space displacements considering a few outputs surrounding this time. Finally, it computes the intersection of the world line of the galaxy with the straight light cone of the observer in redshift space using a cubic interpolation. Since as showed in section(3.3) it apply the shift to the dark matter particle and then recover the galaxy pattern, we need a bias relation.

As said in section(3.3) LIGER is able to account also for the observer terms in equation(2.38), equation(2.39) and equation(2.40), but in our analysis the catalogs are computed avoiding these terms. We reserve an analysis with the observer term for future works. To pass from the matter density to the galaxy density we use the bias relation from (Pozzetti et al. 2016)

$$b(z) = 0.68(z-1) + 1.46. \tag{4.3}$$

The shift equations presented in section(2.2) allows to select with effect we want to consider and apply the shifts only consider them. It allows to create two catalogs (the catalogs are already avaiable from the previous work of Elkhashab, Porciani, and Bertacca (2021))

- *vRSD*: that contains the particle shifted only due to the peculiar velocities of the galaxies;
- *GR*: that contains the particle shifted accounting also for the general relativistic effects presented.

At the end our analysis will be performed on these two types of catalogs, that mean that we will have two power spectra: one that has the peculiar velocity effect and one that contains also the general relativistic effects, so even though we expect they will be enough similar, we want to understand if some differences are detectable. For both type we run 50 realizations for a full sky survey as showed, that means that our simulations are restricted in a full sphere layer between specific redshift. In figure(4.1) we show the projected density field for a 15 $h\,\mathrm{Mpc}^{-1}$ slice of the full sky catalog at $z = (1, 1.25)$. Red spots represents over-density regions in the sky, on the contrary blue spots under-dense regions. We run our analysis for two very distant redshift bins, in order to detect some different behaviour at variuos distances. The chosen redshift bin are a sphere layer between $z = (0.9, 1.1)$ and $z = (1.5, 1.8)$. In figure(4.2) are showed instead some layers with width 15 h Mpc at $z = (1, 1.25)$ of the GR and vRSD simulations and the Real Space counterpart, that is the catalog without the shifts. Already without any analysis is possible to appreciate by eye what discussed in the section(1.2). The galaxy pattern in redshift space (vRSD) presents the described "squashed" configuration, with respect to the real space, due to the apparent shift due to the peculiar motion of the galaxies. The GR catalog instead is very similar to the vRSD one as expected, since it contains both the peculiar velocities and general relativistic effects, that are presents but their effect on the galaxy pattern is not so high to be appreciated by eye. This is the first (very qualitative) confirmation that the expected power spectra will be very similar with a very similar behaviour and that the differences between the two will be very small.

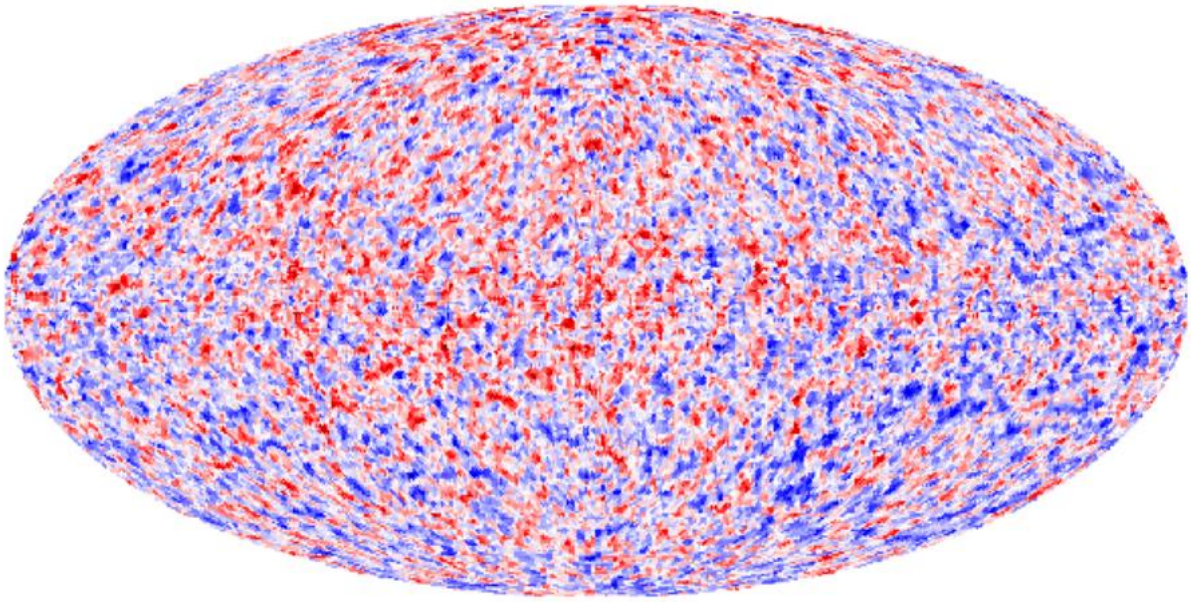

Figure 4.1: The projected density field of a full-sky realization mock for $z = (1, 1.25)$. (Relativistic effects in next-generation surveys, Elkhashab Yousry Master thesis, 2019)

4.2 Method

4.2.1 Simulation volume

As said we use the vRSD and GR catalogs from Elkhashab, Porciani, and Bertacca (2021) and in this section we see the chosen volume inside which run them. As discussed in section(2.1) and section(2.2) the peculiar velocities and the general relativistic effects are expected to modify the behaviour of the power spectrum at large scales (see figure(2.9) and figure(2.10)) so this implies that our analysis is focused on the low k modes of the power spectrum. It is thus crucial to have the biggest simulation volume possible, because the higher the volume the lower the modes at which we can push our analysis, since the lower k modes observable is set by the fundamental frequency (see section(4.2.3) for a discussion on the fundamental frequency in our analysis). Unfortunately for how the Quadratic estimator algorithm is constructed our analysis cannot be applied to too low modes. The $n(\mathbf{r})$ quantity that appears in the FKP-like matrix set a limit to our analysis. It is computed first interpolating the number density of the random catalog in function of the redshift (or the comoving distance), that is, first the volume is divided into small redshift bin and second the number density is obtained dividing the number of random galaxies in that bin by the volume of the bin. The result is an interpolating function showed in figure(4.3) for the $z = (0.9, 1.1)$ case, where on the x axes there is the comoving distance and on the y axes there is the value of $n(\mathbf{r})$. We see

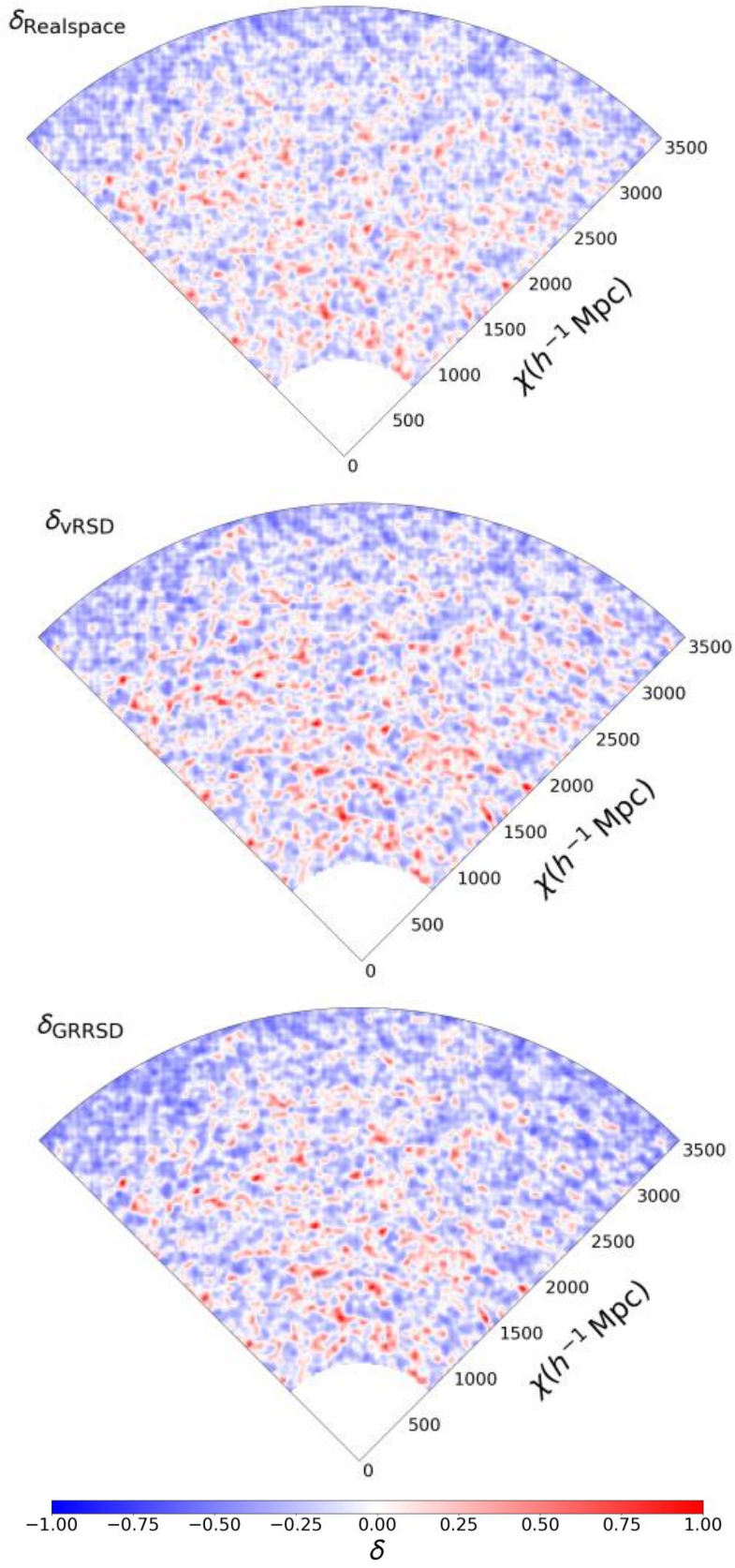

Figure 4.2: Three slices with width 15 $h\,\text{Mpc}^{-1}$ respective of a realization mock in Real Space, of the vSRD catalog and GR catalog for $z = (1, 1.25)$. (Relativistic effects in next-generation surveys, Elkhashab Yousry Master thesis, 2019)

that it is a step function since it is restricted to the selected redshift bin and that random catalog number density decreases with the distance. The interpolating function takes in input a redshift value and gives as output the value of the random number density (so it gives non zero value only for redshift between the selected layer). It is applied to a grid that has in each cell the value of the redshift at that distance cell, in order to obtain a grid that in each cell has the value of the random density field at that specific redshift. This means that volume cannot be chosen in an arbitrary way, but it has to be chosen sufficiently small so that when it is divided in to the grid, each redshift in each cell correspond to a "physical value". This means that if for example we chose a volume bigger than the Hubble volume, the algorithm trying to assign to each cell a redshift value, it will give an error for the cells that are in the region higher then the Hubble volume. For this reason we are restricted in the choice of the simulation volume, and thus we choose a box volume with $L_{side} = 10\ h^{-1}$Gpc that in any case is still suitable for our purpose, since it is enough to study sufficiently large scales. Note that the $n(r)$ that appears in the covariance matrix and its derivative (see equations (3.56) and (3.40)) is different from that just explained. It is computed directly from the random catalog grid, in which it is multiplied for the alpha factor (to normalize the grid to the galaxy catalog) and then each value is divided for the cell volume, in order to find the density.

Another limit set by the algorithm itself is that due to the presence of the $\Theta^a(\mathbf{k})$ weight in equation(3.40), that is 1 if $\mathbf{k}$ is inside $|\mathbf{k}|$-bin a and zero else, the power spectrum can be measured only up to the Nyquist frequency k_{Ny}, that is $k_{Ny} = \pi/L_{cell}$ and set the highest frequency that can be used to properly sample the galaxy distribution (Falck et al. 2017), since for higher modes the weight is zero. This is not a problem for us since small scales are out of our interest.

4.2.2 Monte Carlo simulations

As showed in section(3.3) the Fisher and bias terms are calculated averaging over a several running Monte Carlo simulations and then subtracting it from the estimator to unbias it. O. Philcox (2020) states that computing these traces via Monte Carlo, it increases the estimator variance by a factor

$$\sqrt{1 + \frac{1}{N_{mc}}} \tag{4.4}$$

with N_{mc} the number of Monte Carlo simulations. The number of simulations suggested by O. Philcox (2020) to properly account for the window function effect is between 50 and 100. To choose how many Monte Carlo simulations to use we test how the power spectrum of one realization changes with the number of simulations used. In figure(4.4 is showed the power spectrum of one realizations for the $z = (1.5, 1.8)$ redshift bin after various number of Monte Carlo simulation. As expected the more the number

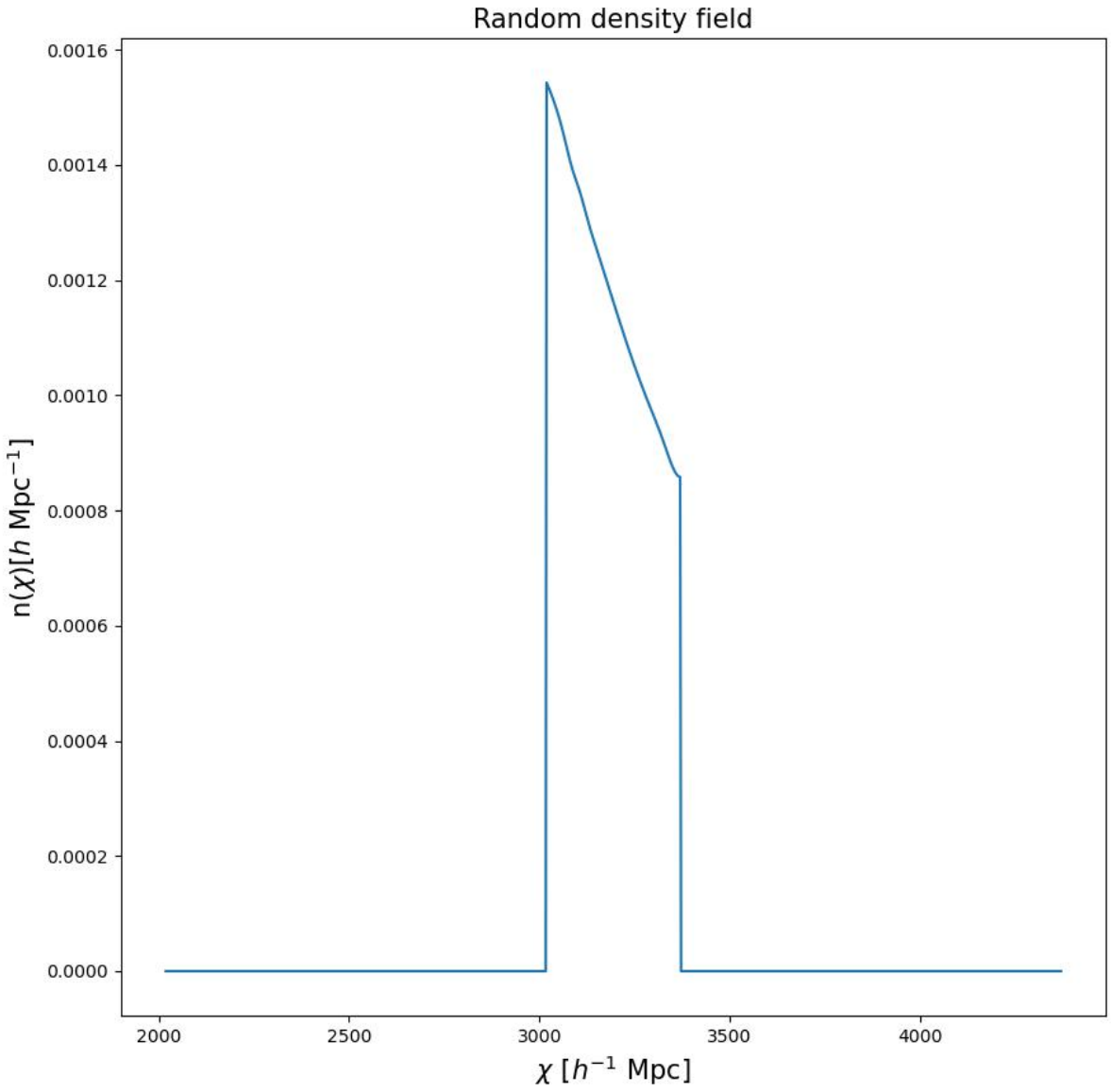

Figure 4.3: Random density field of one realization in function of the comoving distance for a GR realization at $z = (1.5, 1.8)$. This is the $n(\mathbf{r})$ term that appears in equations (3.56) and (3.40).

of simulations the more accurate the power spectrum is, converging to the final power spectrum from which is totally subtracted the window function and bias effects. So for each realizations we run 100 Monte Carlo simulations, increasing the estimator variance of

$$\sqrt{1+\frac{1}{100}} \approx 0.5\% \tag{4.5}$$

4.2.3 Dependencies

To recover the actual power spectrum for the catalogs, we find that there are two specific settings to set in the algorithm, that without them it gives an un-physical or under-estimated power spectrum. These two settings are:

- k_{min}: We are interested in the largest scales possible of the power spectrum, so we tried to set the minimum k mode to $k_{min} = 0$, in order to have the first bin at $k = 0.0025\ h\,\mathrm{Mpc}^{-1}$, since our bin width is set to $\Delta k = 0.005\ h\,\mathrm{Mpc}^{-1}$. This however for some realizations leads to a power spectrum with a negative first bin. This surely is wrong since the power spectrum can't be negative by definition. We overlap this issue setting as k_{min} a mode barely less than the fundamental frequency, that is

  $$k_{fund} = \frac{2\pi}{L_{box}} = 0.000628\ h\,\mathrm{Mpc}^{-1}, \tag{4.6}$$

  so our k_{min} is set to

  $$k_{min} = 0.0005\ h\,\mathrm{Mpc}^{-1}, \tag{4.7}$$

  in order to be sure that we include the fundamental frequency in our analysis. Applying this correction the obtained power spectrum is positive at all scales.

- *Pixelization effects*: In the cosmological simulations we have to paint the galaxy mass distribution into a discrete grid, assigning to each cell a certain value of the density field, meaning that it is spread in a discrete way, while in reality (being a field) it is smooth. As showed in Cui et al. (2008) the discretized number density contrast can be expressed as

  $$\delta^d = \frac{1}{N} = \sum_i n_i e^{i\mathbf{r}_i\cdot\mathbf{k}} - \delta^K_{\mathbf{K},0}, \tag{4.8}$$

  and so the power spectrum is

  $$P(k) = \langle|\delta(\mathbf{k})|^2|\rangle = \langle|\delta^d(\mathbf{k})|^2\rangle - \frac{1}{N} \tag{4.9}$$

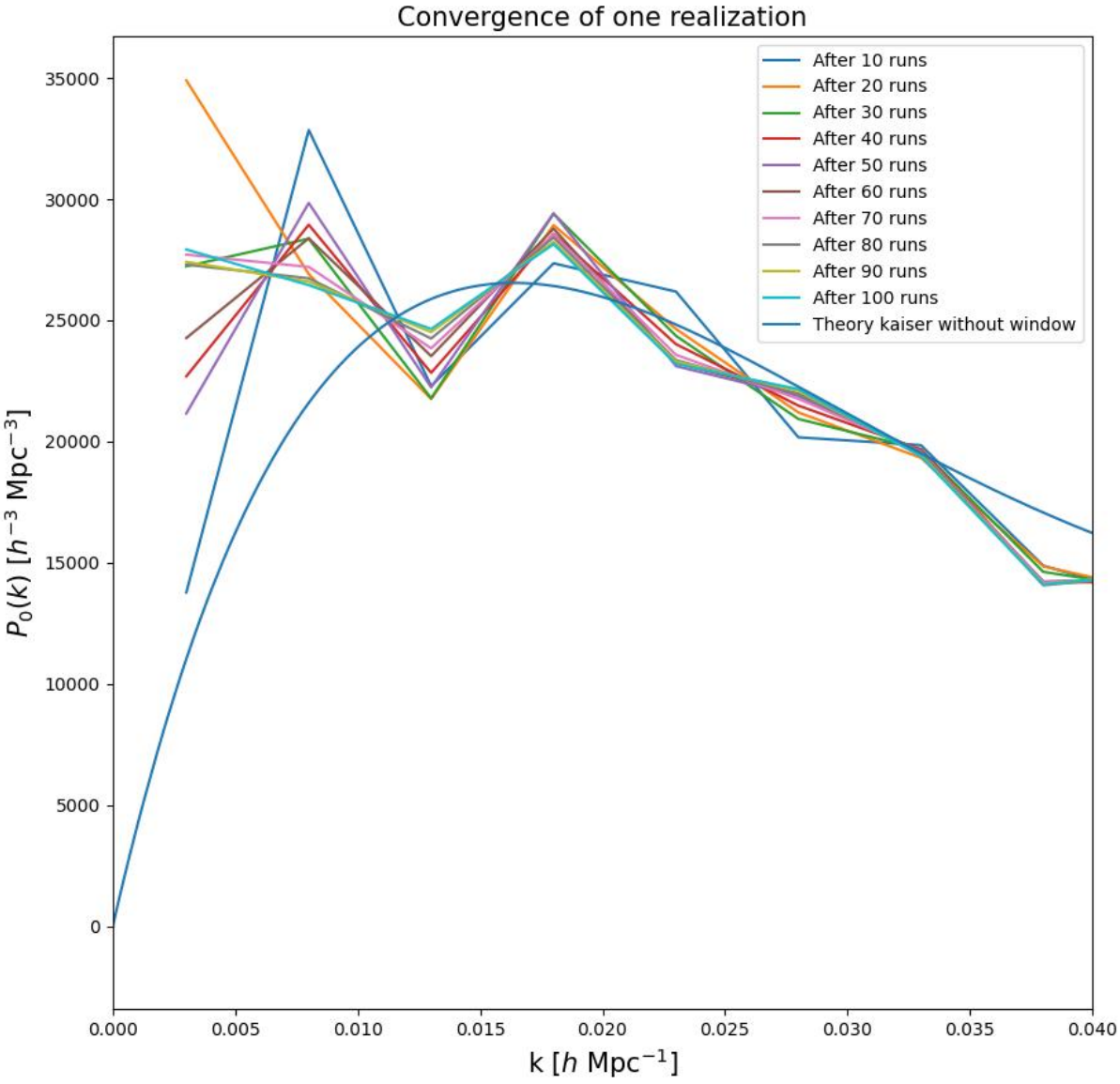

Figure 4.4: The convergence of the power spectrum of a GR realization at $z = (1.5, 1.8)$ after various Monte Carlo run. Each line is a power spectrum computed after the number of Monte Carlo simulations showed in the legend. For comparison with plot the kaiser prediction (blue line)(1.7).

where $1/N$ is the shot-noise term related to the discreteness effect. Since the number of object in a N-body simulations is very high, this method is unfeasible and so we write the density contrast in Fourier space

$$\delta^f(\mathbf{k}) = \frac{1}{N}\sum_g n^f(\mathbf{r}_g) e^{i\mathbf{r}_g\cdot\mathbf{k}} - \delta^K_{\mathbf{K},0}, \tag{4.10}$$

where the superscript f represents the FFT and $n^f(\mathbf{r}_g)$ is the convolved density value on th $\mathbf{g}-th$ grid point at the position $\mathbf{r}_g = \mathbf{g}H$ (where $\mathbf{g}$ is an integer vector; H is the grid spacing)

$$n^f(\mathbf{r}_g) = \int n(\mathbf{r}) W(\mathbf{r}-\mathbf{r}_g) d\mathbf{r}$$

where $W(\mathbf{r})$ is the Mass Assigment Scheme (MAS). After several steps (Jing 2005) we obtain the final power spectrum estimator

$$\langle|\delta^f(\mathbf{k})|^2\rangle = \sum_{\mathbf{n}} |W(\mathbf{k}+2k_N\mathbf{n})|^2 P(\mathbf{k}+2k_N\mathbf{n}) + \frac{1}{N}\sum_{\mathbf{n}} |W(\mathbf{k}+2k_N\mathbf{n})|^2, \tag{4.11}$$

(note that this form is very similar too equation(4.9). Here $W(\mathbf{k})$ is the Fourier transform of $W(\mathbf{r})$, $k_N = \pi/H$ is the Nyquist wavenumber and the summation is over all 3D integers vectors $\mathbf{n}$. The MAS introduces a $W^2(\mathbf{k})$ term both in the true power spectrum that now is convolved with it and in the shot-noise part. Obviously the convolved power spectrum is not the true power spectrum, that is the one that we are interested to measure, so we have to deconvolve the MAS effect from it. Knowing how is the shape of $W(\mathbf{k})$ is possible to recover the true power spectrum, by simply dividing the convolved one by the window function $W(\mathbf{k})$ (in Fourier space, since in Real space it would be a de-convolution). In figure(4.5) are showed the most used MAS schemes that are (Jeong 2010): the Nearest Grid Point (NGP) in solid line, Cloud In Cell (CIC) as dotted line and Triangular Shaped Cloud (TSC) dashed line. In figure(4.5) is shown how these three MAS schemes assign the matter field to the grid point. The NGP assign all the value of the matter field only to a grid cell, so it is a step function centered in the cell centre, the CIC is a first order distribution that assign the field using a pyramidal function, and the TSC is a second order distribution (the most accurate) that has a "bell" shape. The difference is that in the first case the value of the smooth field is totally assigned to that cell, while in the other cases most of its value is assigned to the selected cell, but it is spread also in the surrounding cells, with the value in the other cells that depends on the chosen scheme. TSC is the most accurate since assign the value to each cell with a smooth second order distribution, so we use it. The impact of the window function is modeled as

$$\sum_n W^2(\mathbf{k}+2k_N\mathbf{n}) = \prod_{i=1}^{3}\left[1-\sin^2\left(\frac{\pi k}{2k_N}\right)+\frac{2}{15}\sin^4\left(\frac{\pi k}{2k_N}\right)\right], \tag{4.12}$$

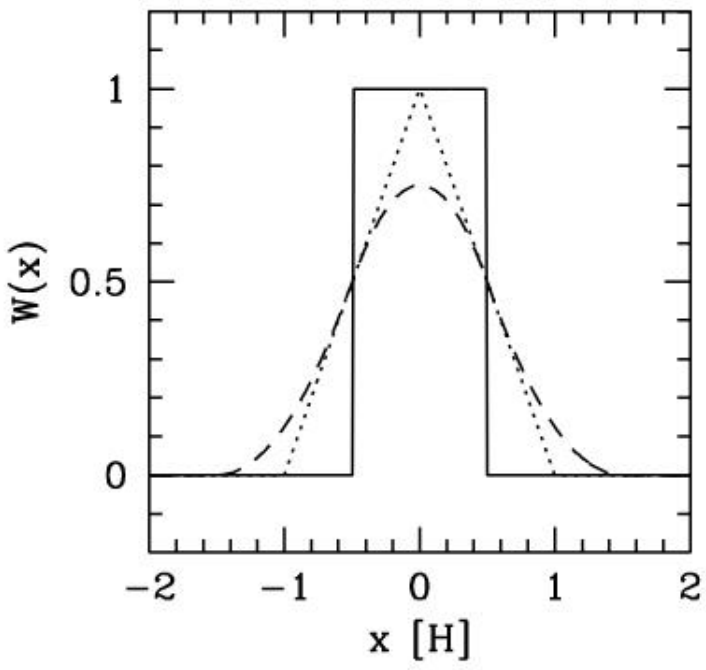

Figure 4.5: A scheme that shows the three most used Mass Assigment Scheme: NGP in solid line, CIC in dotted line and TSC in dashed line. (Cui et al. 2008)

and this is the correction that the algorithm applies to the density grid to recover the actual power spectrum.

In figure(4.6) are shown how these settings change the power spectrum of the same realization. The green power spectrum is the one with only the pixelization correction, the blue contains only the correction due the pixelization effect and the orange one is the power spectrum after having applied both corrections. We see that if we don't account for the k_{min} correction (but accounting for the pixelization effect), we obtain a negative power spectrum at first bin, that is un-physical, while if we don't account for the pizelization effect (accounting for the k_{min} correction) we recover an underestimated power spectrum. Thus we run our realizations accounting for both corrections recovering the right power spectrum without negative value and with the actual power, showed as orange line.

4.2.4 FKP Comparison

As shown in section(3.2) for computing the Quadratic estimator we have to select which choice of the matrix $\mathbf{H}$ we want to adopt, in order to compute the Fisher and Bias term

$$F^{QE}_{\alpha\beta} = \frac{1}{2} Tr[\mathbf{H}^{-1}\mathbf{C}_{,\alpha}\mathbf{H}^{-1}\mathbf{C}_{,\beta}], \qquad \bar{q}_\alpha = \frac{1}{2} Tr[\mathbf{H}^{-1}\mathbf{C}_{,\alpha}\mathbf{H}^{-1}\mathbf{N}], \tag{4.13}$$

and

$$\hat{q}_\alpha = \frac{1}{2} Tr[(\mathbf{H}^{-1}\mathbf{C}_{,\alpha}\mathbf{H}^{-1})\mathbf{d}\mathbf{d}^T]. \tag{4.14}$$

The choice is between the Maximum likelihood estimator with $\mathbf{H}$ equal to the covariance of the used fiducial cosmology

$$\mathbf{H} = \mathbf{C}_{\text{fid}}, \tag{4.15}$$

and the FKP-like estimator with

$$\mathbf{H} = \mathbf{H}_{\text{FKP}} = n(\mathbf{r}) n\left(\mathbf{r}'\right) P_{\text{FKP}} \delta_D\left(\mathbf{r} - \mathbf{r}'\right) + n(\mathbf{r}) \delta_D\left(\mathbf{r} - \mathbf{r}'\right). \tag{4.16}$$

The ML approach requires significantly more computational expense than the FKP-like estimate, mainly due to the necessity to invert the fiducial covariance $\mathbf{C}_{\text{fid}}$, while the inversion of the weight matrix in the latter case is immediate. For this reason we opt for the FKP-like estimate, that makes our computation faster. The cons of this choice is that the Maximum likelihood estimator produces minimum variance error bars on the power spectrum, with a particular improvement on large scales, while the FKP-like is optimal at smaller scales (although it still gives an un-windowed power spectrum at all scales). We will investigate the impact of the variance in the next section.

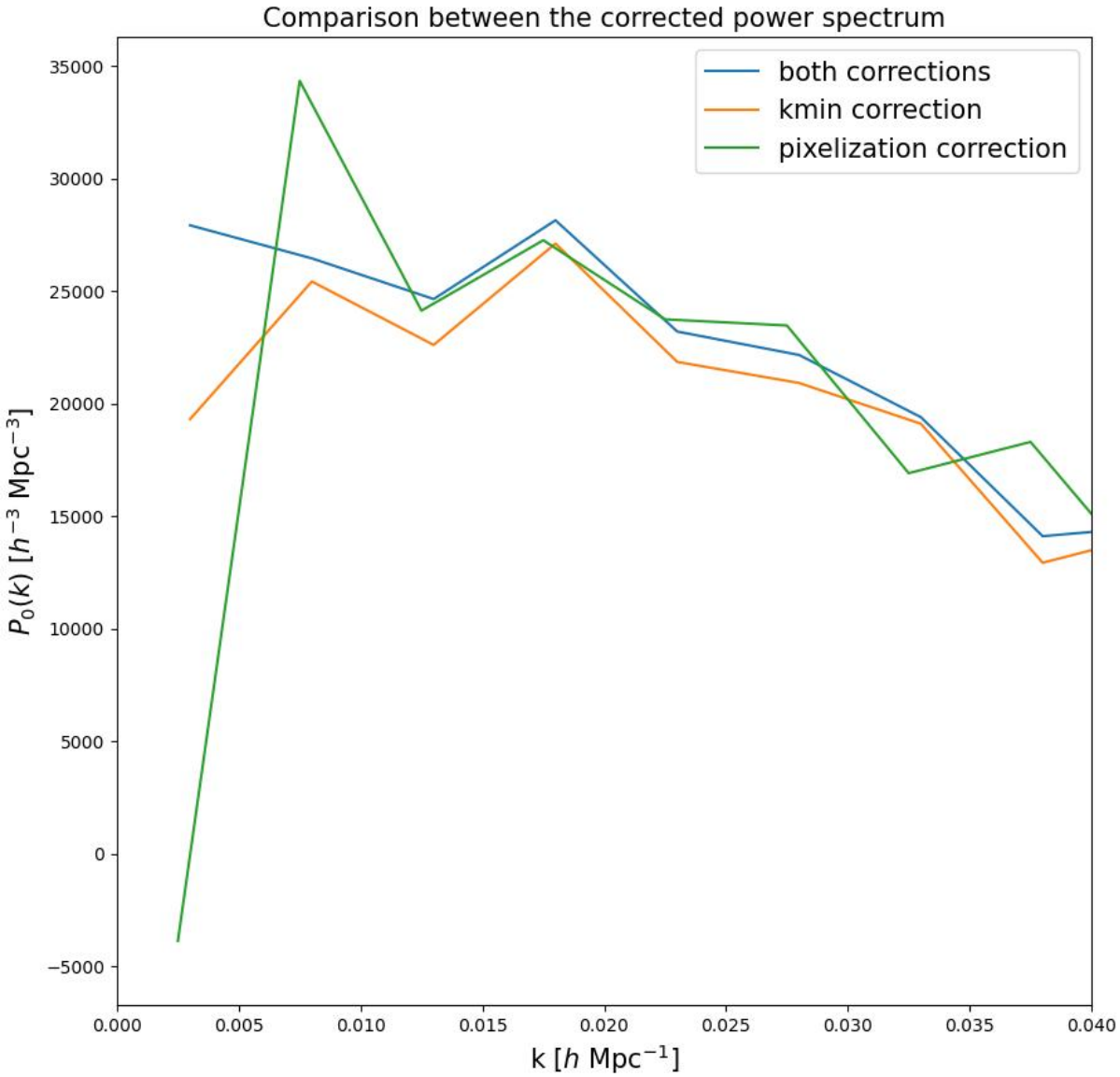

Figure 4.6: Comparison between the chenging of the power spectrum applying the k_{min} setting and the pixelization correction. The power spectra are computed at $z = (1.5, 1.8)$

We test if the FKP-like estimator actually gives an unwindowed power spectrum even with higher variance at large scales comparing our results with the power spectrum estimate using the normal FKP estimator. The latter measures the galaxy power spectrum weighting the galaxy according to (J. A. Peacock 1998)

$$\omega(\mathbf{r}) = \frac{1}{1+\bar{n}(\mathbf{r})P(k)}, \tag{4.17}$$

with the differences from our weight matrix already presented in section(3.2.2). We run the analysis for the power spectra computed with our estimator and the normal FKP estimator, for 15 realizations of the GR catalog at $z = (1.5, 1.8)$. The FKP realizations are computed with NBODYKIT and clearly it gives a power spectrum convolved with the window function. In figure(4.7) the blue dots are the power spectrum computed with the quadratic estimator, the green line the one computed with NBODYKIT and the orange line is the theory predicted by the kaiser formula (equation(1.7)) without the window function. As expected the blue dots follow the un-windowed prediction by kaiser (a part for the first bin that will be discussed in the next section) and they depart from the power spectrum computed with the FKP estimator since it contains also the effect of the window function.

4.3 Un-windowed power spectra

We apply the quadratic estimator to the catalogs presented in 4.1, for various redshift bins. We calculate the monopole of the power spectrum and so as in equation(3.39) the power spectrum is expanded via Legendre polynomials

$$P(k, \hat{\mathbf{k}} \cdot \hat{\mathbf{r}}') = \sum P_l(k) L_l(\hat{\mathbf{r}}'), \tag{4.18}$$

where the coefficients are defined as

$$P_l(k) = (2l+1) \int \frac{d\sigma_{\mathbf{k}}}{4\pi} L_l(\hat{r}') P(k), \tag{4.19}$$

with the monopole that corresponds to $l = 0$. As showed in Raccanelli, Bertacca, Jeong, et al. (2016) if the $\alpha(z)$ term is note set to zero, that is we are not adopting the flat-sky approximation, the monopole of the power spectrum in Redshift Space is written as

$$P_0^s = \left(1 + \frac{2}{3}\beta + \frac{1}{5}\beta^2 + \frac{\alpha^2}{3k^2\chi^2}\beta^2\right) P(k). \tag{4.20}$$

Note that as saw in section(1.8) adopting the wide angle formalism will introduce a dependence on the k modes that brings a phase shift between the Real and Redshift

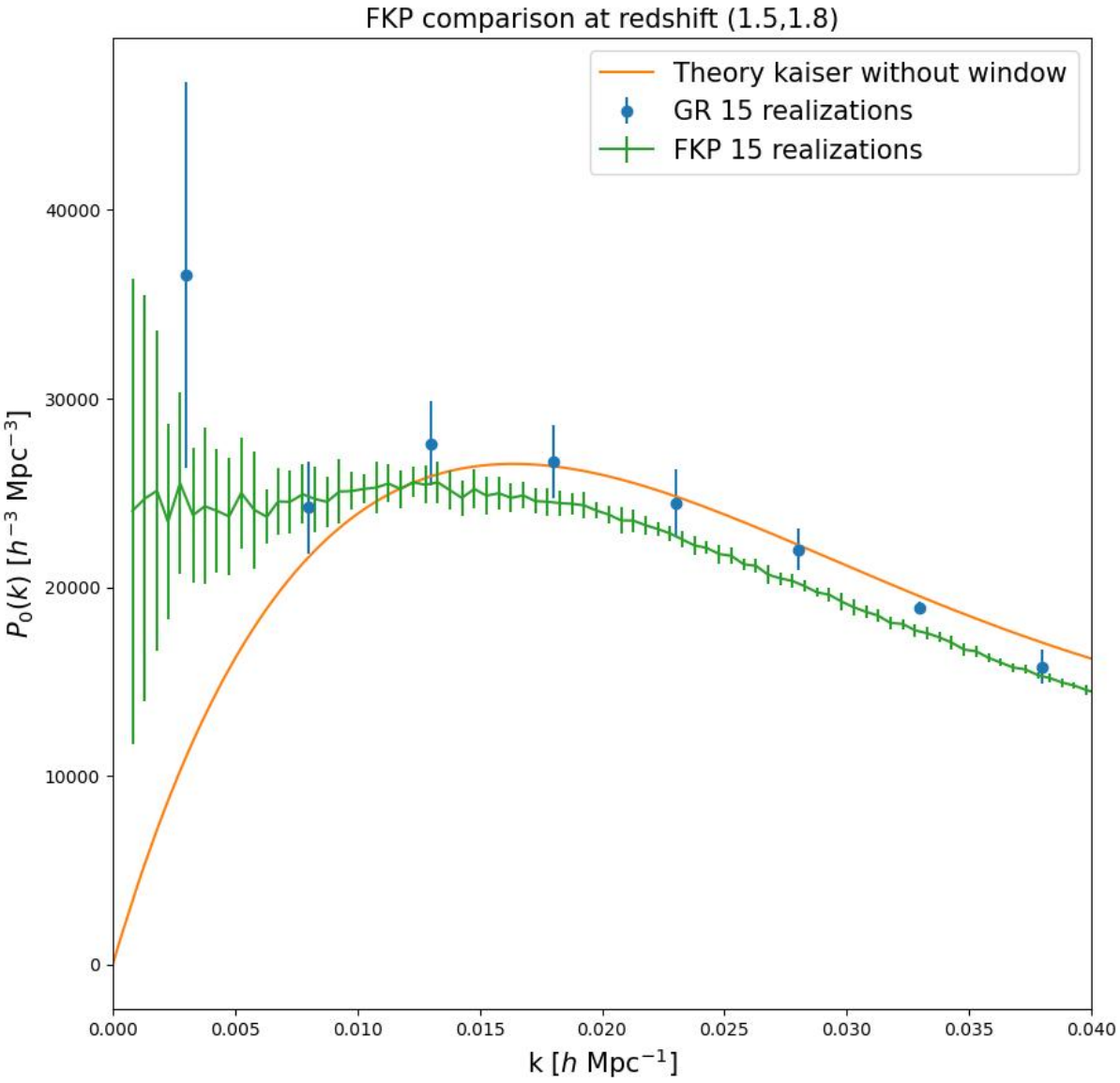

Figure 4.7: Comparison between the power spectrum estimates computed with the Quadratic estimator (blue dots) and the power spectrum estimates computed with the FKP prescription (green line), compared with the kaiser prediction (orange line) (1.7).

Space.As said we run our analysis for 50 realizations of the vSRD catalog and 50 realizations of the vRSD catalog for the $z = (0.9, 1.1)$ and $z = (1.5, 1.8)$ redshift bins. In figure(4.8) and figure (4.9) are showed the obtained average of all the realizations of the un-windowed power spectra in each bin. The green line is the kaiser prediction (equation(1.7)) un-convolved with the window function, the blue and orange dots are the average un-windowed monopole values obtained with the quadratic estimator presented in section(3.2) for the GR (blue dots) and vRSD (orange dots) catalogs presented in section(4.1).

We analyze the results for the $z = (1.5, 1.8)$ redshift bin. The first thing that is immediate to observe is that as anticipated in section(4.1) the power spectra of the GR and vRSD catalogs are very similar, in fact they present the same behaviour, making their detachment visible only for scales $k < 0.015\, h\,\mathrm{Mpc}^{-1}$. The vRSD power spectrum fits very well the predicted un-windowed theory from kaiser, meaning that the power spectrum obtained with the quadratic estimator actually is not convolved with the window function. It is easy to see that the estimate in the first bin it has more power than expected by the prediction prediction. We explain this discrepancy considering that as suggested in O. Philcox (2020)) the first k bin is affected by the integral constraint. As showed in Max Tegmark, Andrew J. S. Hamilton, et al. (1998) the integral constraint is a direct consequence of the fact that in a survey we don't know the selection function $\bar{n}(\mathbf{r})$, in fact if this wouldn't be true, the power spectrum estimation would be simply the square of the ratio of the observed and expected number of galaxies in our sample. Since we don't know $\bar{n}(\mathbf{r})$ a priori, we use the galaxies themselves to normalize it, thus the density fluctuation automatically vanish at the size of the whole survey. In equation(1.60) we see that with the presence of the noise b_α there is also an additional term $W(0)$ relative to the integral constraint that should be subtracted for recover an actual totally un-bias power spectrum. Unfortunately the quadratic estimator can unbias the power spectrum estimation from the window function and the noise effects, but not from the integral constraint, that, as explained, affect only the first bin. We explain this over-power at very large scales on the first bin also considering this behaviour as signal of doppler term and wide angle effects, as explained in the next paragraph. As showed in section(2.1) the estimates for the GR catalog and so the power spectrum that contains also the general relativistic effects has the same behaviour respect at small scale, while at large scale the GR power spectrum is amplified. As expected we see that the two spectra have different behaviour, so it is clearly shown the importance of accounting for the general relativistic effects for a proper analysis, especially at scales $k < 0.0015\, h\,\mathrm{Mpc}^{-1}$, as anticipated in section(2.1).

In figure(4.8) is shown instead the $z = (0.9, 1.1)$ case both for the GR and vRSD catalog. As before the first bin is affected by the integral constrain, so it has more power than expected. Contrary to the previous case we see that in this redshift bin the estimated monopole for the vRSD catalog agree with the theory only for scales $k > 0.020\, h\,\mathrm{Mpc}^{-1}$

while for higher scales there is a deviation that over estimate the power. The same happen to the GR catalog, in fact both catalogs have the same behaviour at all scales. We interpret this result as signature of the presence of the "Doppler term" explained in section(1.5). In this section we saw that if we don't neglect the v/r term, it can affect the power spectrum at large scales. The green line that is the kaiser prediction uses the flat-sky approximation, where this term is neglected, while LIGER in computing the shifts account also for the modification that derives from accounting also for the Doppler term. In fact we see that as showed in section(1.5) the power spectrum estimates accounting for the doppler term present an over-power at large scale, with respect to the Kaiser prediction, that is exactly what we found. Another reason in favour of this explanation is that the redshift bin in which we observer this discrepancy is the lower one $z = (0.9, 1.1)$, while for the other it appears only at the first bin. In fact also this aspect is in a certain way expected, since we saw that the lower the redshift the higher the importance of the doppler term, since it scales with distance. In figure(4.10) are shown the power spectra from Elkhashab, Porciani, and Bertacca (2021), where a normal FKP weight formalism is used. The redshift bin of interest are the first and the last, as in our computation. The dotted blue line is the predicted kaiser power spectrum (as in our plots). We see that in this case the effect of the window function at large scales is prominent in both bins, while in our computation since we are free from these effects, we recover the expected behaviour at large scales, where we have much more power. This shows how crucial is to be able to avoid the window function effect to study the redshift space distortion and general relativistic effects at large scales.

As said the vRSD catalog is computed accounting for the Redshift Space Distortions due to the peculiar velocities of the galaxies, while the GR one is computed accounting for the Redshift Space Distortions plus the general relativistic effects, so it is necessary to understand if these effects are measurable, that is, if the two power spectra are "different enough". This means that if we want to understand how significant are the general relativistic effects we call P^{GR} their partial contribution to the galaxy power spectrum and the respective counterpart (without general relativistic effects) as $P^{NOgr} = P - P^{gr}$. We then fit the power spectra extracted from our mock catalogues with the model $M = \varepsilon P^{gr} + P^{NOgr} = P + (\varepsilon - 1)P^{gr}$ with ε that can be either 0 or 1. We want to understand with how much statistical significance the data favour $\varepsilon = 0$ instead of $\varepsilon = 1$, that is, how much the data favour the presence or not of the general relativistic effects to properly fit the model. In order to do this we use a frequentist approach called "Simple hypotheses". To the $\varepsilon = 0$ hypothesis we assign $\mathfrak{L}_1$, that is the likelihood of the data under this hypothesis and instead $\mathfrak{L}_2$ to the $\varepsilon = 1$ hypothesis. We compute the likelihood-ratio $\lambda = \mathfrak{L}_1/\mathfrak{L}_2$ that will be small if the data favour the $\varepsilon = 1$ hypothesis, while it will be high if the data favour the $\varepsilon = 0$ one. Assuming Gaussian error each

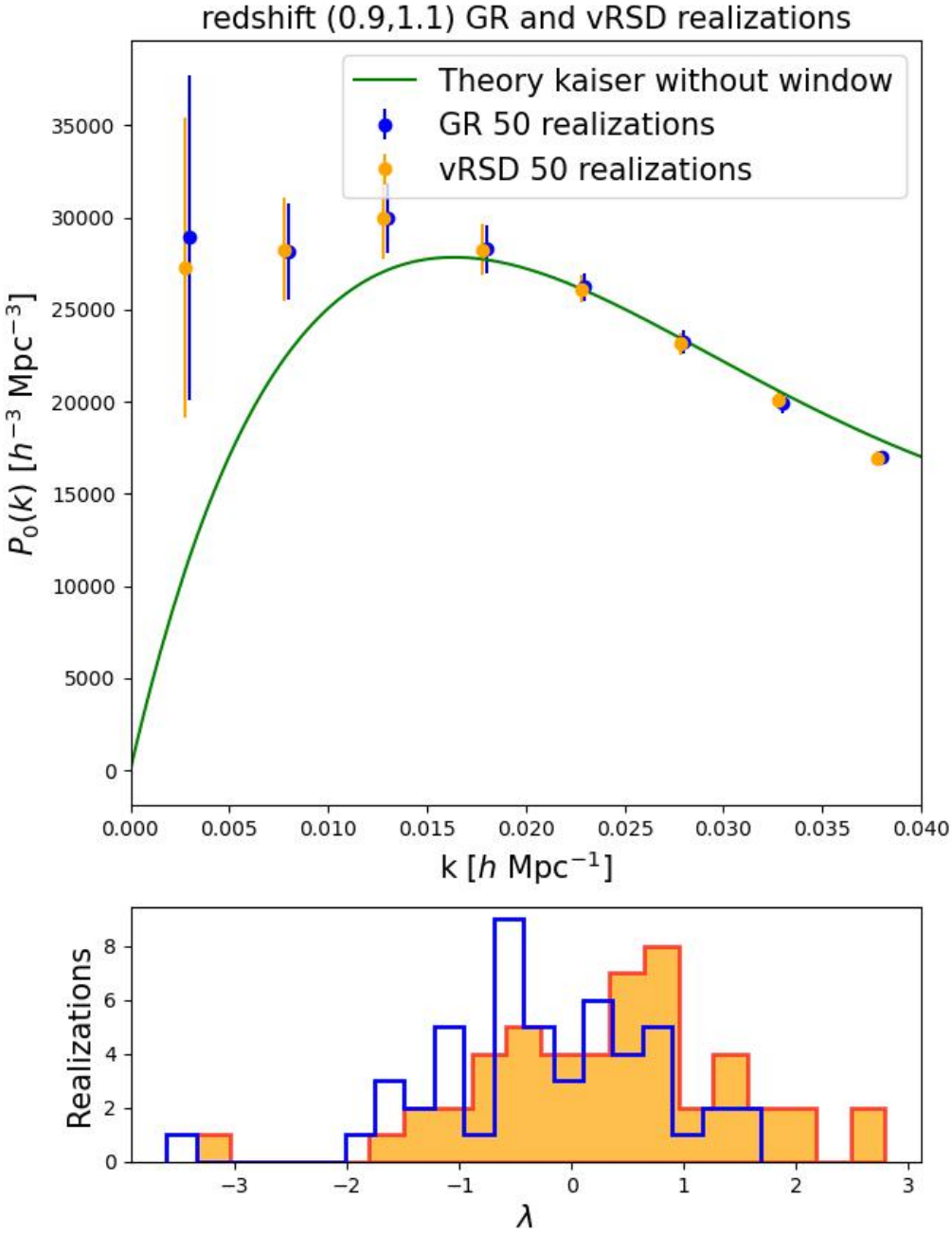

Figure 4.8: *Top:*Power spectrum estimates with the Quadratic estimator for the $z = (0.9, 1.1)$ redshift bin for 50 realizations of the GR catalog (blue dots) and vRSD catalog (orange dots), compared with the un-windowed kaiser prediction (green line). *Bottom:* Likelihood test bewteen the GR and vRSD catalogs.

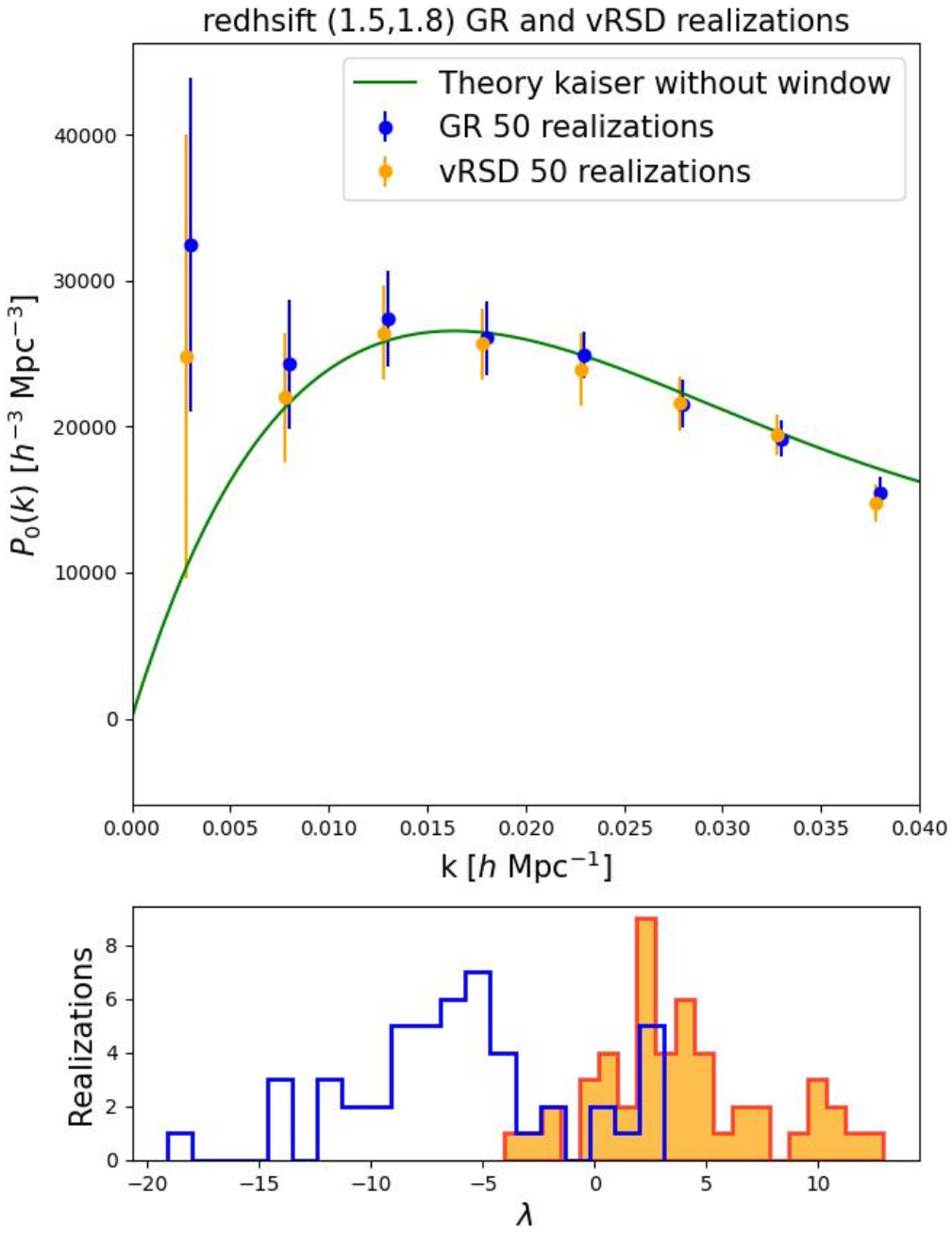

Figure 4.9: *Top:*Power spectrum estimates with the Quadratic estimator for the $z = (1.5, 1.8)$ redshift bin for 50 realizations of the GR catalog (blue dots) and vRSD catalog (orange dots), compared with the un-windowed kaiser prediction (green line). *Bottom:* Likelihood test bewteen the GR and vRSD catalogs.

likelihood can be written as

$$\mathfrak{L}(M_i|\mathbf{d}) = \frac{1}{(2\pi)^{n/2}\det\mathbf{C}_i}\exp\left[-\frac{1}{2}(\mathbf{d}-\boldsymbol{\mu}_i)^T\cdot\mathbf{C}_i^{-1}\cdot(\mathbf{d}-\boldsymbol{\mu}_i)\right], \tag{4.21}$$

where $\mathbf{d}$ is a n-dimensional vector that contains the monopole moments of the power spectrum extracted from one realization of the GR mock, μ_i and $\mathbf{C}_i$ are the expected data and covariance matrix under the hypothesis that the model M_i is true. We use M_2 as the model referred to the hypothesis used to compute the GR catalog and so μ_2 and $\mathbf{C}_2$ are the average power spectrum and covariance matrix of the GR realizations, while M_1 the one referred to the hypothesis used to compute the vRSD catalog and and so μ_1 and $\mathbf{C}_1$ are the average power spectrum and covariance matrix of the vRSD realizations. The likelihood-ratio test is (Elkhashab, Porciani, and Bertacca 2021)

$$\lambda = 2\ln\frac{\mathfrak{L}(M_1|\mathbf{d})}{\mathfrak{L}(M_2|\mathbf{d})} = \chi_2^2 - \chi_1^2 + \ln\det\mathbf{C}_2 - \ln\det\mathbf{C}_1, \tag{4.22}$$

with

$$\chi_i^2 = (\mathbf{d}-\boldsymbol{\mu}_i)^T\cdot\mathbf{C}_i^{-1}\cdot(\mathbf{d}-\boldsymbol{\mu}_i) \text{ for } i\text{=GR, vRSD.} \tag{4.23}$$

If this quantity is positive the data favour M_1 while if it is negative M_2, that is, if it is positive the data favour the model without the relativistic effects, while if it is negative the data favour the model without them. The likelihood-ratio test distribution are shown in the low panels of figure(4.8) and figure(4.9) with on the x-axes the λ value while in the y-axes the number of realizations with that value. We see that in the $z = (0.9, 1.1)$ case both the distribution generated under the hypothesis that M_1 is true and the one generated considering M_2 true have basically the same λ value distribution, so it is impossible to distinguish which hypothesis is true and thus in this case the general relativistic effects can't be distinguished. Different is the $z = (1.5, 1.8)$ case where the two distributions cover quite different ranges of λ values, in fact the distribution of the M_1 hypothesis has a peak around $\lambda = +5$ while the one that consider M_2 true has a peak around $\lambda = -5$, so in this case we consider that the general relativistic effects are distinguishable from the Redshift Space Distortions connected to the peculiar velocities of the galaxies, so they are detectable. Since the higher the separation between the histogram the higher the general relativistic effects are detectable, we parametrize the discrepancy between the histogram in terms of Signal over Noise ratio

$$S/N = \frac{(m_1 - m2)}{s_1}, \tag{4.24}$$

where m_1 and m_2 are the mean of the distribution GR and vRSD distributions, while s_1 is the standard deviation of the GR distribution. We compute the S/N ratio for both bins, obtaining

- $S/N = 2.05$, for the $z = (1.5, 1.8)$ redshift bin;
- $S/N = 0.57$, for the $z = (0.9, 1.1)$ redshift bin.

These results are in line with what observed, in fact in the lower redshift bin the S/N is too high, the distributions are not separated and this means that the general relativistic effects are not detectable, while in the higher redshift bin the separation of the distributions mean a high S/N ratio and so in this case the effects are separable from the peculiar velocities of the galaxies.

As last thing we compute an analysis on the errors obtained with the quadratic estimator. As described in section(1) after inflation the distribution of matter was almost Gaussian so we expect that the error at large scale should reproduce the error of a Gaussian matter distribution. We compute the Gaussian error as in (Max Tegmark, Andrew J. S. Hamilton, et al. 1998)

$$\sigma_G^2 \simeq P^0(k)\sqrt{\frac{2(2\pi)^3}{V_{\text{eff}}(k)V_k}}, \tag{4.25}$$

where

$$V_{\text{eff}}(k) = \int_{\mathbf{S}} \left[\frac{\bar{n}(\mathbf{x})P_0^2(k)}{1+\bar{n}(\mathbf{x})P_0^2(k)}\right]^2 d^3x, \tag{4.26}$$

is the effective volume probed and V_k si the volume of the k-shell centered around k with width Δk and if $k \gg \Delta k$ it is $V_k \equiv 4\pi k^2 \Delta k$. In figure(4.11) and figure(4.12) are shown the ratio between the Quadratic estimation errors and the Gaussian error. We see that in both cases our error are higher than the Gaussian, with a ratio around ≈ 1.25 for the $z = (0.9, 1.1)$ and ≈ 6 for the $z = (1.5, 1.8)$ bin. This result (especially for the higher bin) is not expected, since the Gaussian errors computed with equation(4.25) they are computed assuming a Gaussian distribution, that at these redshift should be a good approximation and are not affected by the window function effects, so they should be comparable with the errors from our analysis. Furthermore the higher the redshift the higher the galaxy distribution should reproduce the Gaussian one, but in our analysis we see that at higher redshift the error are more different from the Gaussian respect to the lower redshift. Note also that for the $z = (1.5, 1.8)$ bin there is a notable difference between the ratio of the GR and vRSD error, with the former that are more near to the Gaussian one. It seems that deconvolving the window function increases the variance of our estimates and for high redshift bin the an analysis that accounts also for the general relativistic effects can reproduce better (but not well) the error expected by a Gaussian overdensity. For comparison we show the error from Elkhashab, Porciani, and Bertacca (2021) but for different redshift bin. We see that in this case the error (green line) and the integral constraints (purple line) are way lower than the gaussian one (red one) as expected at large scales.

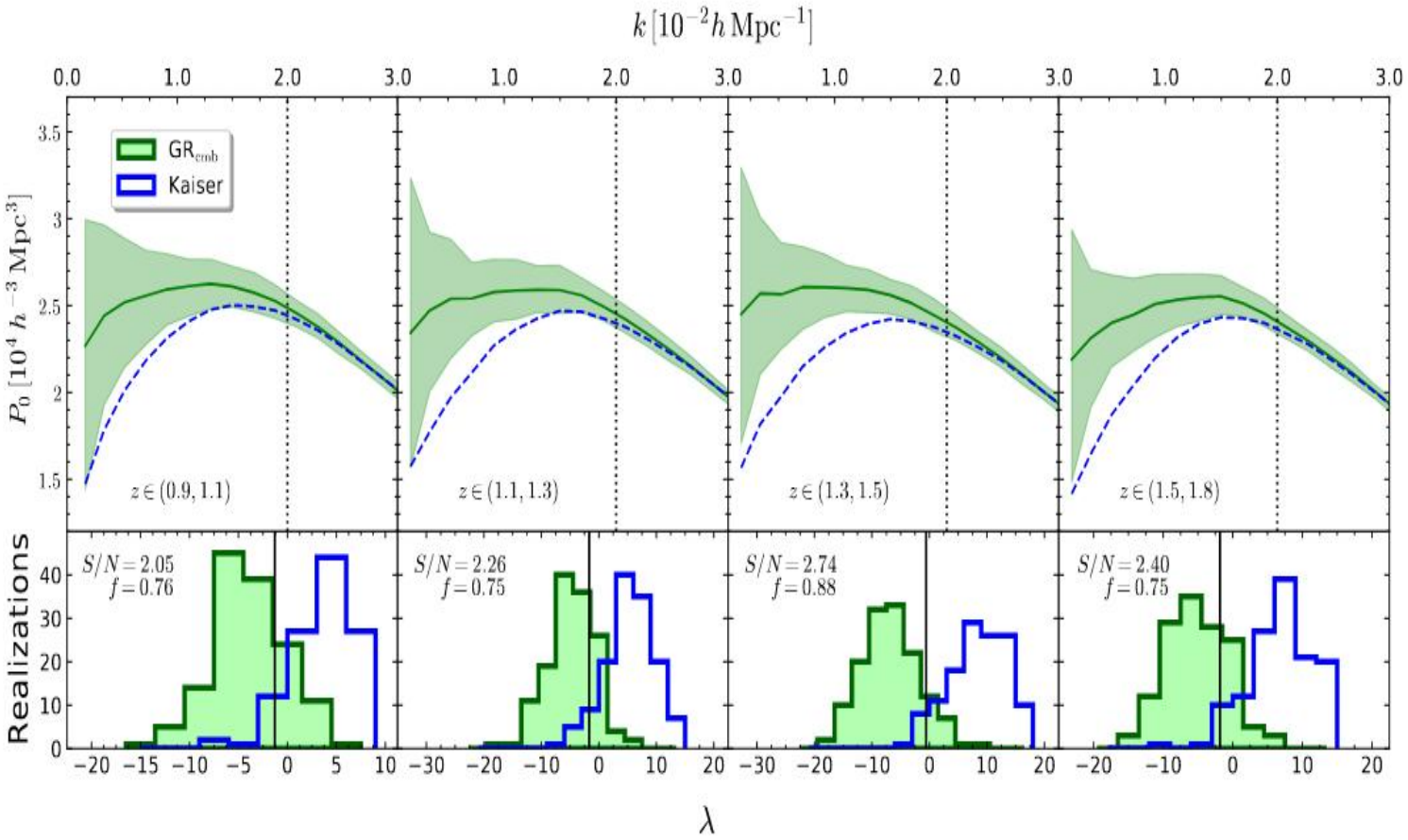

Figure 4.10: *Top panel*: GR power spectra obtained in Elkhashab, Porciani, and Bertacca (2021), compared with the kaiser theory, for various redshift bins. *Low panel*: Likelihood ratio test of each bin between the GR catalog and the kaiser prediction. (Figure from (Elkhashab, Porciani, and Bertacca 2021))

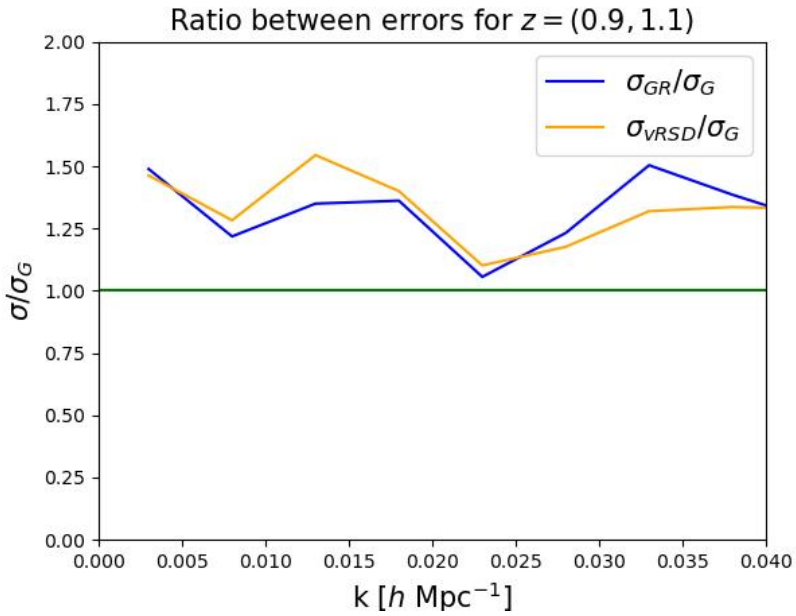

Figure 4.11: Ratio between our error and the Gaussian for the $z = (0.9, 1.1)$ redshift bin.

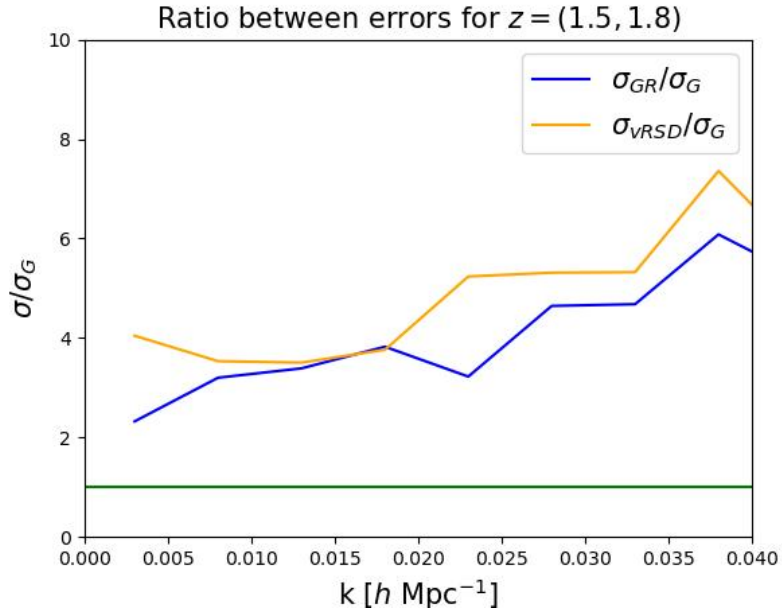

Figure 4.12: Ratio between our error and the Gaussian for the $z = (1.5, 1.8)$ redshift bin.

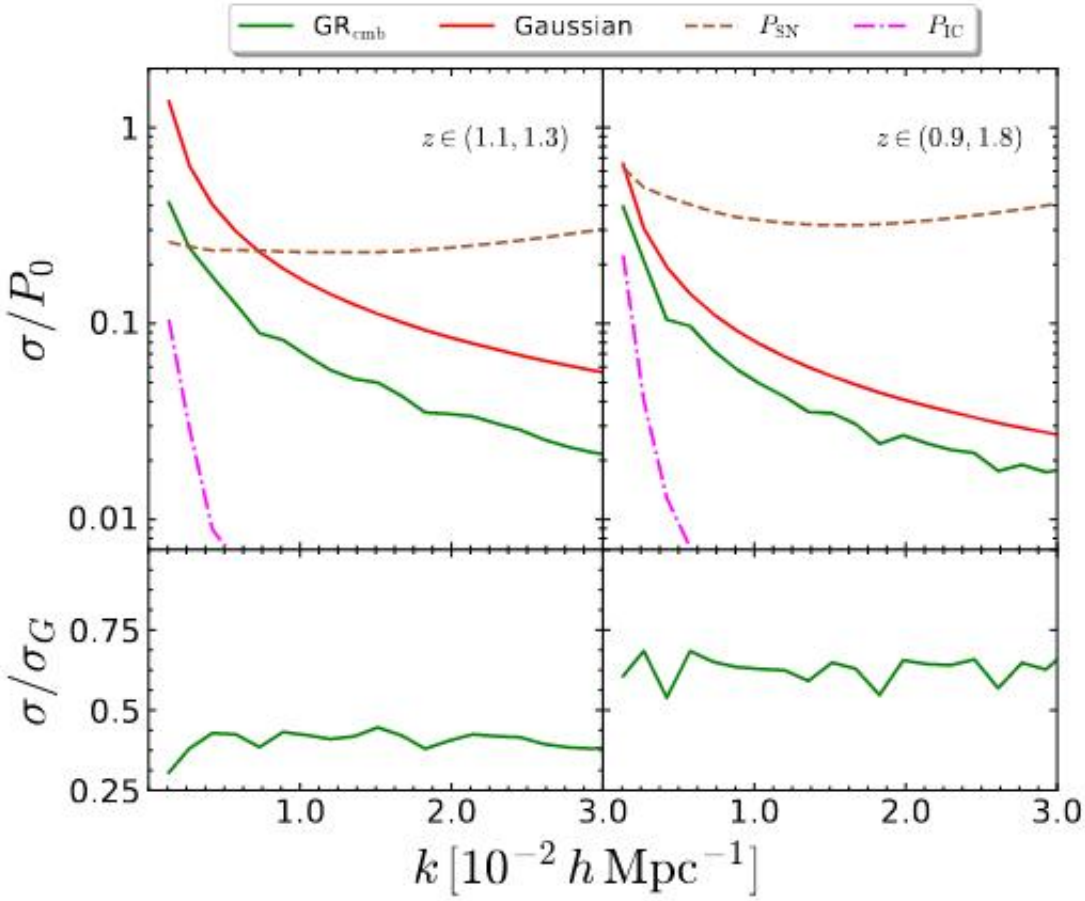

Figure 4.13: The error (green line) and the integral constraint (purple line) obtained from Elkhashab, Porciani, and Bertacca (2021), compared with the Gaussian one (red line). Are shown the $z = (1, 1.3)$ and $z = (0.9, 1.8)$ redshift bins.

Chapter 5

Conclusion

Redshift-space distortions analyses are a powerful tool in cosmology. Incoming survey data need more and more accurate estimator in order to fully extract all available information contained. In the first chapter we showed how the galaxy pattern from Real to Redshift Space is altered by the Redshift Space Distortions due to the peculiar velocity of the galaxies that alter the observed redshift of a galaxy and so its distance. Future galaxy surveys will cover very deep and large portion of the sky (Euclid, SKA, SPHERE etc.) almost approaching the Hubble radius and so can be demonstrated that also general relativistic effects such as Sachs-Wolfe effect, gravitational and Doppler lensing and Shapiro-time delay can modify the observed redshift and so the position of the galaxy. It is crucial to accounts for all these effect to obtain a proper analysis and as showed also for the inference of cosmological paramteres. In the second chapter we presented all these effects, explaining how they would affect the power spectrum. The problem is that these effects are detectable only at very large scale, where the window function of the survey is dominant, making their analysis impossible. In this work we investigate if these effects are measurable in absence of the window function effects. Always in the second chapter we presented the code LIGER, that is able to create survey map in Redshift space, simply starting from a Newtonian simulation and applying all the shifts in the galaxy positions a priori. The shift can account both for the Redshift Space Distortions and the general relativistic effects. Thanks to this we are able to create two catalogs: vRSD that contains the shift in the galaxy pattern only due to the peculiar velocity of the galaxy and GR that accounts also for the shifts due to the general relativistic effects. Our goal is to measure the power spectra for these two catalogs at various redshift ($z = (0.9, 1.1)$ and $z = (1.5, 1.8)$) not convolved with the window function. We compute the monopole of the power spectrum using a new version of the Quadratic estimator presented in the third chapter, that is able to compute a un-convolved power spectrum, unbiasing the estimator subtracting the window function and the bias term as showed. We run 50 realizations for the GR and vRSD catalog in both redshift. Our result are shown in the last chapter. We found that the algorithm is very sensible to

the choice of the k_{min} (the modes from which the power spectrum is computed) and the accounting of the pixelization effect. It is able to reproduce the actual power spectrum if $k_{min} > 0$, so we set $k_{min} = 0.005\,h\,\mathrm{Mpc}^{-1}$, and if we account for the pixelization effects. without the first condition some realizations present a negative power spectrum, that is un-physical, while without the second condition, the obtained power spectrum is under-powered. The correct power spectrum with both the corrections is shown as orange line in figure(4.6). We showed that the window function effects are deleted through the subtraction of the Fisher and Bias term, computed via Monte Carlo simulations. We testes the convergence of the power spectrum in function of the number of simulations ran and we found that with 100 Monte Carlo simulations the power spectrum converges to the un-windowed one, as showed in figure(4.4). The quadratic estimator presents two possible way to compute the un-windowed spectra, the likelihood analysis and the FKP-like analysis. For computational reason we chose the second option, and in order to be sure that it gives an un-windowed spectra we test it against the spectra computed with the classical FKP estimator with NBODYKIT that clearly contains the windoe function effect. The result is shown in figure(4.7) for 15 realizations, showing that our estimator actually differs from the FKP power spectrum, since it is actually free from the window function effects. In the figure(4.8) and figure(4.9) are shown the estimated power spectra for the two redshift bins and the likelihood ratio test, used to understand if the general relativistic effects are detectable The main results can be summarized as follow:

- $z = (1.5, 1.8)$ redshift bin:
  - The power spectrum for the vRSD catalog is in perfect agreement with the Kaiser prediction not convolved with the window function, meaning that the obtained power spectrum is completely un-convoled;
  - The power spectrum of the GR catalog has the expected behaviour showed in section(2.1), since it amplifies the power at large scale due to the presence of the relativistic effects;
  - In both cases the first bin has a very huge power, more then expected. O. Philcox (2020) shows that it is affected by the Integral Constraint, so he suggests to do not consider it in the analysis;
  - The likelihood ratio test shows that the ratio distribution for the GR and vRSD catalog are quite far, meaning that in this case the general relativistic effects can be actually distinguished by the the effects induced by the peculiar velocities of the galaxies;
  - The comparison with the Gausssian errors shows that our error are rather higher than the Gaussian. This result is not expected since the higher the redshift bin, the more the galaxy configuration should reproduce a Gaussian one, and thus also its errors.

- $z = (0.9, 1.1)$ redshift bin:
  - The power spectrum in this redshift bin presents an over-power estimates at large scales. Since we are sure that the obtained monopole is not convolved with the window function (as showed for the $z = (1.5, 1.8)$ redshift bin), we interpret this behaviour at large scales as probing the presence of the doppler term effects. Our explanation is also supported by the fact that they appear in the smaller redshift bin, as the wide angle prescription suggests;
  - The likelihood ratio analysis in this bins presents two lihelihood ratio distributions for the two catalogs that are basically the same, meaning that the presence of the doppler term make the general relativistic effects not distinguishable from the peculiar velocities;
  - Comparing the errors with the Gaussian errors we found that in this case our error are still higher then the Gaussian, but less than the other redshift bin. Another time this is not expected since this is the lowest redshift bin, and the disagreement should be higher than the higher bin.

The issue of the error remains an open question, but in the future would be interesting to run the quadratic estimator assuming the maximum Likelihood Estimator presented in section(3.2.1), that as said at large scale could gives less errors bar. It will be interesting also to run our analysis also for lower redshift bin, for example at $z < 0.4$, where the doppler term effects are dominant, extending our analysis also to the dipole and quadrupole of the power spectrum to have a more complete analysis of the changing in the power spectrum due to the wide angle effects. Next analyses could be done also for more complicated survey geometry as for Euclid, in order to be able to make predictions on what will be actually observable during the mission.

List of Figures

1.1 The schematic process of how the potential of the inflaton changes. At the beginning the inflaton potential remains almost constant, before beginning to oscillate during the reheating phase. (Figure from Gonzalez, Padilla, and Matos 2020). 3

1.2 Behaviour of the Hubble radius (equation1.1) during inflation, in which are highlighted when a generic scale k^{-1} (as previous defined as $k = 2\pi/\lambda$) enters and exits the horizon (Figure from Nandi 2017a). 3

1.3 Taking four coordinate points that makes a square, is qualitatively shown the difference between the physical and comoving distance. The first depends on time and is bigger since the expasion of the square, while the latter remain constant, since it expands with the Universe.(Figure from Dodelson 2003) 5

1.4 Differences of the positions measured between the Real and Redshift spaces, figure from A. J. S. Hamilton (1998). 10

1.5 Difference between a survey in Real space and Redshift space (Figure from Praton, Melott, and McKee 1997) 11

1.6 Visualization of how the over-densities change between the Redshift and real space. (Figure from A. J. S. Hamilton 1998) 18

1.7 Comparison between the predicted power spectrum in Real space and with kaiser formula for a full sky survey with $z = (1.5, 1.8)$. The Real Space power spectrum is computed with equation(1.54) assuming the cosmology in table(4.1), while the power spectrum in Redshift space is computed with equation(1.7) with same cosmology. 19

1.8 *Left:* How galaxies moves from Redshift to Real Space adopting the plane parallel approximation, giving rise to the "Pancake" of God shape. *Right*: How the situation change adopting the wide angle formalism, now the galaxies moves along different Line of Sight, giving rise to the "Croissant" of God shape.(Figure from Raccanelli, Bertacca, Jeong, et al. 2016) 22

1.9 Position of galaxies in the wide angle formalism. here each galaxy has its own Line Of Sight through it is projected, and so now the θ angle is the observational angle, while ϕ is the angle between the galaxies separation directiona and the Line of Sight (Figure from Raccanelli, Samushia, and Percival 2010) 25

1.10 The angle averaged power spectra for $z = 0.1$ computed in the flat-sky approximation (solid black line) with $f_{NL} = 0$ (for a detailed discussion on f_{NL} see section(2.1)), accounting for wide angle effect, that is the Doppler term (dotted black) with $f_{NL} = 0$, in the flat-sky approximation (solid black line) with $f_{NL} = 5$ and accounting for wide angle effect, that is the Doppler term (dotted black) with $f_{NL} = 5$ (Figure from Raccanelli, Bertacca, Jeong, et al. 2016). For comparison are showed the expected error obtained with the SPHEREx (Spectro-Photometer for the History of the Universe, Epoch of Reionization and Ices Explorer), that is a mission that will scan the whole sky. SPHEREx will survey hundreds of millions of galaxies near and far, some so distant their light has taken 10 billion years to reach Earth. 26

1.11 The angle averaged power spectra for $z = 1$ computed in the flat-sky approximation (solid black line) with $f_{NL} = 0$ (for a detailed discussion on f_{NL} see section(2.1)), accounting for wide angle effect, that is the Doppler term (dotted black) with $f_{NL} = 0$, in the flat-sky approximation (solid black line) with $f_{NL} = 5$ and accounting for wide angle effect, that is the Doppler term (dotted black) with $f_{NL} = 5$ (Figure from Raccanelli, Bertacca, Jeong, et al. 2016). For comparison are showed the expected error obtained with the SPHEREx (Spectro-Photometer for the History of the Universe, Epoch of Reionization and Ices Explorer), that is a mission that will scan the whole sky. SPHEREx will survey hundreds of millions of galaxies near and far, some so distant their light has taken 10 billion years to reach Earth. 27

1.12 2D redshift space galaxy correlation function accounting (black lines, right) and not accounting (colored contour, left) for the wide angle effects, at redshift bins $z = 0.1$ (top) and $z = 1$ (bottom). At high redshift the Doppler term is negligible. At low-z, in the plane-parallel approximation, the lines overlap meaning that the doppler term is negligible. However, the top right panel shows how the doppler term in the low-z case is not negligible, since the black lines and colored contour are not overlapping, meaning that at low-z the correlation function strongly depends on if the doppler term effects are considered or not. (Figure from Raccanelli, Bertacca, Jeong, et al. 2016) 28

2.1 A scheme of how the Gravitational lensing distorts the position of a source. The inferred poisition on the sky of the galaxy depends on hoy the photon path was influenced by the inhomogeneity between the observer and the source. Source: "http://cmbcorrelations.pbworks.com", credit: Peter Laursen 30

2.2 A scheme of how doppler lensing works in which are shown how the galaxies are magnified or de-magnified according to their peculiar motion(Bacon et al. 2014) 30

2.3 A scheme of how Sachs-Wolfe effect works. Are shown the two cases in which a photon acquires or loose energy. Source: (Figure from Nandi 2017b) 31

2.4 The red dot are the points where the doppler lensing multipoles power is equal to the gravitational one in function of the redshift, with the blue line the interpolating function. The plot shows the ranges in which the gravitational and doppler lensing dominates. The former at large redshift and small observational angle, while the latter for low redshift and wide observational angle. (Figure from Bacon et al. 2014) 34

2.5 Ratio between the correlation function accounting for general relativistc effects and in the Newtonian case. (Figure from Bertacca et al. 2012) . . 35

2.6 The dependence of the galaxy clustering on the f_{NL} value: (from top) $f_{NL} = -5000, -500, 0, +500, +5000$. (Figure from Dalal et al. 2008) . 38

2.7 Ellipsoidal error on the f_{NL} and n_{NG} parameters, accounting (solid line) and not accounting (dotted line) for general relativistic effects (Figure from Raccanelli, Bertacca, Maartens, et al. 2016) 39

2.8 Ellipsoidal error on the w_0 and w_a parameters, accounting (solid line) and not accounting (dotted line) for general relativistic effects(Figure from Raccanelli, Bertacca, Maartens, et al. 2016) 40

2.9 The three dimensional galaxy power spectra of the Kaiser prediction (dotted line) (Kaiser 1987), of the kaiser prediction with a $f_{NL} = -0.147$ (dashed line) and the one that accounts for the General relativistic effects (thick line), all at various redshift bins and bias factor b. The vertical line is at $k = aH$, that is the horizon.(Jeong, Schmidt, and Hirata 2012) 42

2.10 The two-dimensional redshift galaxy power spectrum divided in component of the modes parallel to the line Of Sight $k_{//}$ and perpendicular $k_{\perp}$, for various redshift(Jeong, Schmidt, and Hirata 2012) and bias factor 43

2.11 The configuration of how the path of a photon is altered and consequently the position of the emitting galaxy (Figure from Borzyszkowski, Bertacca, and Porciani 2017) 44

2.12 A scheme of how LIGER weight the particle shifts, accounting for both local and integrated terms. (Figure from Borzyszkowski, Bertacca, and Porciani 2017) 51

3.1 The plots shows how the window function affect the power spectrum in Real Space of a full sky particle configuration at redshift $z = (1.5, 1.8)$. The blue line is the un-convolved power spectrum, while the orange is the convolved one. 59

3.2 The plots shows how the window function affect the power spectrum of the Kaiser prediction of a full sky particle configuration at redshift $z = (1.5, 1.8)$. The blue line is the un-convolved power spectrum, while the orange is the convolved one. 60

4.1 The projected density field of a full-sky realization mock for $z = (1, 1.25)$. (Relativistic effects in next-generation surveys, Elkhashab Yousry Master thesis, 2019) 74

4.2 Three slices with width 15 h Mpc^{-1} respective of a realization mock in Real Space, of the vSRD catalog and GR catalog for $z = (1, 1.25)$. (Relativistic effects in next-generation surveys, Elkhashab Yousry Master thesis, 2019) 75

4.3 Random density field of one realization in function of the comoving distance for a GR realization at $z = (1.5, 1.8)$. This is the $n(\mathbf{r})$ term that appears in equations (3.56) and (3.40). 77

4.4 The convergence of the power spectrum of a GR realization at $z = (1.5, 1.8)$ after various Monte Carlo run. Each line is a power spectrum computed after the number of Monte Carlo simulations showed in the legend. For comparison with plot the kaiser prediction (blue line)(1.7). 79

4.5 A scheme that shows the three most used Mass Assigment Scheme: NGP in solid line, CIC in dotted line and TSC in dashed line. (Cui et al. 2008) 81

4.6 Comparison between the chenging of the power spectrum applying the k_{min} setting and the pixelization correction. The power spectra are computed at $z = (1.5, 1.8)$ 83

4.7 Comparison between the power spectrum estimates computed with the Quadratic estimator (blue dots) and the power spectrum estimates computed with the FKP prescription (green line), compared with the kaiser prediction (orange line) (1.7). 85

4.8 *Top:*Power spectrum estimates with the Quadratic estimator for the $z = (0.9, 1.1)$ redshift bin for 50 realizations of the GR catalog (blue dots) and vRSD catalog (orange dots), compared with the un-windowed kaiser prediction (green line). *Bottom:* Likelihood test bewteen the GR and vRSD catalogs. 88
4.9 *Top:*Power spectrum estimates with the Quadratic estimator for the $z = (1.5, 1.8)$ redshift bin for 50 realizations of the GR catalog (blue dots) and vRSD catalog (orange dots), compared with the un-windowed kaiser prediction (green line). *Bottom:* Likelihood test bewteen the GR and vRSD catalogs. 89
4.10 *Top panel*: GR power spectra obtained in Elkhashab, Porciani, and Bertacca (2021), compared with the kaiser theory, for various redshift bins. *Low panel*: Likelihood ratio test of each bin between the GR catalog and the kaiser prediction. (Figure from (Elkhashab, Porciani, and Bertacca 2021)) 92
4.11 Ratio between our error and the Gaussian for the $z = (0.9, 1.1)$ redshift bin. 93
4.12 Ratio between our error and the Gaussian for the $z = (1.5, 1.8)$ redshift bin. 93
4.13 The error (green line) and the integral constraint (purple line) obtained from Elkhashab, Porciani, and Bertacca (2021), compared with the Gaussian one (red line). Are shown the $z = (1, 1.3)$ and $z = (0.9, 1.8)$ redshift bins. 94

List of Tables

4.1 Cosmological parameters used to compute the initial power spectrum, from Planck 2018 collaboration (N. Aghanim et al. 2020) 71

Bibliography

Adamek, Julian et al. (Mar. 2016). "General relativity and cosmic structure formation". In: *Nature Physics* 12.4, pp. 346–349. DOI: 10.1038/nphys3673. URL: https://doi.org/10.1038%2Fnphys3673.

Allahverdi, Rouzbeh et al. (2010). "Reheating in Inflationary Cosmology: Theory and Applications". In: *Annual Review of Nuclear and Particle Science* 60.1, pp. 27–51. DOI: 10.1146/annurev.nucl.012809.104511. eprint: https://doi.org/10.1146/annurev.nucl.012809.104511. URL: https://doi.org/10.1146/annurev.nucl.012809.104511.

Altmann, S. L., C. J. Bradley, and William Hume-Rothery (1963). "On the symmetries of spherical harmonics". In: *Philosophical Transactions of the Royal Society of London. Series A, Mathematical and Physical Sciences* 255.1054, pp. 199–215. DOI: 10.1098/rsta.1963.0002. eprint: https://royalsocietypublishing.org/doi/pdf/10.1098/rsta.1963.0002. URL: https://royalsocietypublishing.org/doi/abs/10.1098/rsta.1963.0002.

Anand, Gagandeep S. et al. (July 2019). "Peculiar Velocities of Galaxies Just Beyond the Local Group". In: *The Astrophysical Journal* 880.1, p. 52. DOI: 10.3847/1538-4357/ab24e5. URL: https://doi.org/10.3847/1538-4357/ab24e5.

Bacon, David J. et al. (June 2014). "Cosmology with Doppler lensing". In: *Monthly Notices of the Royal Astronomical Society* 443.3, pp. 1900–1915. DOI: 10.1093/mnras/stu1270. URL: https://doi.org/10.1093%2Fmnras%2Fstu1270.

Bardeen, James M. (Oct. 1980). "Gauge-invariant cosmological perturbations". In: *Phys. Rev. D* 22 (8), pp. 1882–1905. DOI: 10.1103/PhysRevD.22.1882. URL: https://link.aps.org/doi/10.1103/PhysRevD.22.1882.

Bartelmann, Matthias (Nov. 2010). "Gravitational lensing". In: *Classical and Quantum Gravity* 27.23, p. 233001. DOI: 10.1088/0264-9381/27/23/233001. URL: https://doi.org/10.1088%2F0264-9381%2F27%2F23%2F233001.

Bartolo, N. et al. (Nov. 2004). "Non-Gaussianity from inflation: theory and observations". In: *Physics Reports* 402.3-4, pp. 103–266. DOI: 10.1016/j.physrep.2004.08.022. URL: https://doi.org/10.1016%2Fj.physrep.2004.08.022.

Baumann, Daniel (2018). *TASI Lectures on Primordial Cosmology*. DOI: 10.48550/ARXIV.1807.03098. URL: https://arxiv.org/abs/1807.03098.

Benson, Andrew J. (2010). "Galaxy formation theory". In: *Physics Reports* 495.2, pp. 33–86. ISSN: 0370-1573. DOI: https://doi.org/10.1016/j.physrep.2010.06.001. URL: https://www.sciencedirect.com/science/article/pii/S037015731000150X.

Bertacca, Daniele (Sept. 2015). "Observed galaxy number counts on the light cone up to second order: III. Magnification bias". In: *Classical and Quantum Gravity* 32.19, p. 195011. DOI: 10.1088/0264-9381/32/19/195011. URL: https://doi.org/10.1088%2F0264-9381%2F32%2F19%2F195011.

— (July 2020). "Generalization of the Kaiser Rocket effect in general relativity in the wide-angle galaxy 2-point correlation function". In: *International Journal of Modern Physics D* 29.12, p. 2050085. DOI: 10.1142/s0218271820500856. URL: https://doi.org/10.1142%2Fs0218271820500856.

Bertacca, Daniele et al. (Aug. 2012). "Beyond the plane-parallel and Newtonian approach: wide-angle redshift distortions and convergence in general relativity". In: *Journal of Cosmology and Astroparticle Physics* 2012.10, pp. 025–025. DOI: 10.1088/1475-7516/2012/10/025. URL: https://doi.org/10.1088%2F1475-7516%2F2012%2F10%2F025.

Bertschinger, Edmund (1994). "Cosmic structure formation". In: *Physica D: Nonlinear Phenomena* 77.1. Special Issue Originating from the 13th Annual International Conference of the Center for Nonlinear Studies Los Alamos, NM, USA, 17ndash;21 May 1993, pp. 354–379. ISSN: 0167-2789. DOI: https://doi.org/10.1016/0167-2789(94)90145-7. URL: https://www.sciencedirect.com/science/article/pii/0167278994901457.

Beutler, Florian, Emanuele Castorina, and Pierre Zhang (Mar. 2019). "Interpreting measurements of the anisotropic galaxy power spectrum". In: *Journal of Cosmology and Astroparticle Physics* 2019.03, pp. 040–040. DOI: 10.1088/1475-7516/2019/03/040. URL: https://doi.org/10.1088%2F1475-7516%2F2019%2F03%2F040.

Bonvin, Camille (Nov. 2014). "Isolating relativistic effects in large-scale structure". In: *Classical and Quantum Gravity* 31.23, p. 234002. DOI: 10.1088/0264-9381/31/23/234002. URL: https://doi.org/10.1088%2F0264-9381%2F31%2F23%2F234002.

Bonvin, Camille and Ruth Durrer (Sept. 2011). "What galaxy surveys really measure". In: *Physical Review D* 84.6. DOI: 10.1103/physrevd.84.063505. URL: https://doi.org/10.1103%2Fphysrevd.84.063505.

Borzyszkowski, Mikolaj, Daniele Bertacca, and Cristiano Porciani (Jan. 2017). "liger: mock relativistic light cones from Newtonian simulations". In: *Monthly Notices of*

the Royal Astronomical Society 471.4, pp. 3899–3914. DOI: 10.1093/mnras/stx1423. URL: https://doi.org/10.1093%2Fmnras%2Fstx1423.

Boughn, S.P. and R.G. Crittenden (2005). "A detection of the integrated Sachs–Wolfe effect". In: *New Astronomy Reviews* 49.2. Sources and Detection of Dark Matter and Dark Energy in the Universe, pp. 75–78. ISSN: 1387-6473. DOI: https://doi.org/10.1016/j.newar.2005.01.005. URL: https://www.sciencedirect.com/science/article/pii/S1387647305000096.

Brandenberger, Robert H. (2001). *A Status Review of Inflationary Cosmology*. arXiv: hep-ph/0101119 [hep-ph].

Breton, Michel-Andrè s, Sylvain de la Torre, and Jade Piat (May 2022). "Impact of lensing magnification on the analysis of galaxy clustering in redshift space". In: *Astronomy &amp Astrophysics* 661, A154. DOI: 10.1051/0004-6361/202142487. URL: https://doi.org/10.1051%2F0004-6361%2F202142487.

Buchert, Thomas (Apr. 1994). "Lagrangian theory of gravitational instability of Friedman–Lemaître cosmologies – a generic third-order model for non-linear clustering". In: *Monthly Notices of the Royal Astronomical Society* 267.4, pp. 811–820. ISSN: 0035-8711. DOI: 10.1093/mnras/267.4.811. eprint: https://academic.oup.com/mnras/article-pdf/267/4/811/4056911/mnras267-0811.pdf. URL: https://doi.org/10.1093/mnras/267.4.811.

Byrnes, Christian T. and Ki-Young Choi (2010). "Review of Local Non-Gaussianity from Multifield Inflation". In: *Advances in Astronomy* 2010, pp. 1–18. DOI: 10.1155/2010/724525. URL: https://doi.org/10.1155%2F2010%2F724525.

Cardona, Wilmar, Martin Kunz, and Valeria Pettorino (Mar. 2017). "DeterminingiH/isub0/subwith Bayesian hyper-parameters". In: *Journal of Cosmology and Astroparticle Physics* 2017.03, pp. 056–056. DOI: 10.1088/1475-7516/2017/03/056. URL: https://doi.org/10.1088%2F1475-7516%2F2017%2F03%2F056.

Carlberg, R. G., H. M. P. Couchman, and P. A. Thomas (Apr. 1990). "Cosmological Velocity Bias". In: 352, p. L29. DOI: 10.1086/185686.

Carlson, Jordan, Martin White, and Nikhil Padmanabhan (Aug. 2009). "Critical look at cosmological perturbation theory techniques". In: *Physical Review D* 80.4. DOI: 10.1103/physrevd.80.043531. URL: https://doi.org/10.1103%2Fphysrevd.80.043531.

Carroll, Sean M. (2019). *Spacetime and Geometry: An Introduction to General Relativity*. Cambridge University Press. DOI: 10.1017/9781108770385.

Castorina, Emanuele and Martin White (June 2018). "The Zeldovich approximation and wide-angle redshift-space distortions". In: *Monthly Notices of the Royal Astronomical Society*. DOI: 10.1093/mnras/sty1437. URL: https://doi.org/10.1093%2Fmnras%2Fsty1437.

Castorina, Emanuele and Martin White (July 2020). "Wide-angle effects for peculiar velocities". In: *Monthly Notices of the Royal Astronomical Society* 499.1, pp. 893–905. ISSN: 0035-8711. DOI: 10.1093/mnras/staa2129. eprint: https://academic.oup.com/mnras/article-pdf/499/1/893/33873622/staa2129.pdf. URL: https://doi.org/10.1093/mnras/staa2129.

Celoria, Marco and Sabino Matarrese (2018). *Primordial Non-Gaussianity*. DOI: 10.48550/ARXIV.1812.08197. URL: https://arxiv.org/abs/1812.08197.

Challinor, Anthony and Antony Lewis (Aug. 2011). "Linear power spectrum of observed source number counts". In: *Physical Review D* 84.4. DOI: 10.1103/physrevd.84.043516. URL: https://doi.org/10.1103%2Fphysrevd.84.043516.

Chisari, Nora Elisa and Matias Zaldarriaga (June 2011). "Connection between Newtonian simulations and general relativity". In: *Physical Review D* 83.12. DOI: 10.1103/physrevd.83.123505. URL: https://doi.org/10.1103%2Fphysrevd.83.123505.

Coles, Peter (Sept. 1986). "The spatial correlations of Abell clusters". In: *Monthly Notices of the Royal Astronomical Society* 222.1, 9P–14P. ISSN: 0035-8711. DOI: 10.1093/mnras/222.1.9P. eprint: https://academic.oup.com/mnras/article-pdf/222/1/9P/3930172/mnras222-009P.pdf. URL: https://doi.org/10.1093/mnras/222.1.9P.

Cooray, Asantha and Ravi Sheth (2002). "Halo models of large scale structure". In: *Physics Reports* 372.1, pp. 1–129. ISSN: 0370-1573. DOI: https://doi.org/10.1016/S0370-1573(02)00276-4. URL: https://www.sciencedirect.com/science/article/pii/S0370157302002764.

Croom, Scott M et al. (Feb. 2021). "The SAMI Galaxy Survey: the third and final data release". In: *Monthly Notices of the Royal Astronomical Society* 505.1, pp. 991–1016. ISSN: 0035-8711. DOI: 10.1093/mnras/stab229. eprint: https://academic.oup.com/mnras/article-pdf/505/1/991/38391840/stab229.pdf. URL: https://doi.org/10.1093/mnras/stab229.

Cuesta-Lazaro, Carolina et al. (Mar. 2018). "Gravitational corrections to light propagation in a perturbed FLRW universe and corresponding weak-lensing spectra". In: *Monthly Notices of the Royal Astronomical Society* 477.1, pp. 741–754. ISSN: 0035-8711. DOI: 10.1093/mnras/sty672. eprint: https://academic.oup.com/mnras/article-pdf/477/1/741/24649170/sty672.pdf. URL: https://doi.org/10.1093/mnras/sty672.

Cui, Weiguang et al. (Nov. 2008). "An Ideal Mass Assignment Scheme for Measuring the Power Spectrum with Fast Fourier Transforms". In: *The Astrophysical Journal* 687.2, pp. 738–744. DOI: 10.1086/592079. URL: https://doi.org/10.1086%2F592079.

Cunha, Carlos, Dragan Huterer, and Olivier Doré (July 2010). "Primordial non-Gaussianity from the covariance of galaxy cluster counts". In: *Physical Review D* 82.2. DOI: 10.1103/physrevd.82.023004. URL: https://doi.org/10.1103%2Fphysrevd.82.023004.

Dalal, Neal et al. (June 2008). "Imprints of primordial non-Gaussianities on large-scale structure: Scale-dependent bias and abundance of virialized objects". In: *Physical Review D* 77.12. DOI: 10.1103/physrevd.77.123514. URL: https://doi.org/10.1103%2Fphysrevd.77.123514.

Davis, Marc (1998). "Cosmic velocity fields and their interpretation". In: *Proceedings of the National Academy of Sciences* 95.1, pp. 78–81. DOI: 10.1073/pnas.95.1.78. eprint: https://www.pnas.org/doi/pdf/10.1073/pnas.95.1.78. URL: https://www.pnas.org/doi/abs/10.1073/pnas.95.1.78.

Demiański, M. and A. G. Doroshkevich (Feb. 1999). "Super–Large-Scale Structure and Large-Scale Bias". In: *The Astrophysical Journal* 512.2, pp. 527–546. DOI: 10.1086/306779. URL: https://doi.org/10.1086/306779.

DESI Collaboration et al. (2016). *The DESI Experiment Part I: Science,Targeting, and Survey Design*. DOI: 10.48550/ARXIV.1611.00036. URL: https://arxiv.org/abs/1611.00036.

Desjacques, Vincent, Donghui Jeong, and Fabian Schmidt (2018). "Large-scale galaxy bias". In: *Physics Reports* 733. Large-scale galaxy bias, pp. 1–193. ISSN: 0370-1573. DOI: https://doi.org/10.1016/j.physrep.2017.12.002. URL: https://www.sciencedirect.com/science/article/pii/S0370157317304192.

Dodelson, Scott (2003). *Modern Cosmology*. Academic Press, Elsevier Science.

Doré, Olivier et al. (2014). *Cosmology with the SPHEREX All-Sky Spectral Survey*. DOI: 10.48550/ARXIV.1412.4872. URL: https://arxiv.org/abs/1412.4872.

Duhamel, P. and M. Vetterli (1990). "Fast fourier transforms: A tutorial review and a state of the art". In: *Signal Processing* 19.4, pp. 259–299. ISSN: 0165-1684. DOI: https://doi.org/10.1016/0165-1684(90)90158-U. URL: https://www.sciencedirect.com/science/article/pii/016516849090158U.

Dunham, Samuel J. et al. (Apr. 2019). "Lens Model and Source Reconstruction Reveal the Morphology and Star Formation Distribution in the Cool Spiral LIRG SGAS J143845.1145407". In: *The Astrophysical Journal* 875.1, p. 18. DOI: 10.3847/1538-4357/ab0d7d. URL: https://doi.org/10.3847/1538-4357/ab0d7d.

Elkhashab, Mohamed Yousry, Cristiano Porciani, and Daniele Bertacca (Oct. 2021). "The large-scale monopole of the power spectrum in a Euclid-like survey: wide-angle effects, lensing, and the 'finger of the observer'". In: *Monthly Notices of*

the Royal Astronomical Society 509.2, pp. 1626–1645. DOI: 10.1093/mnras/stab3010. URL: https://doi.org/10.1093%2Fmnras%2Fstab3010.

Elsner, F. and B. D. Wandelt (June 2012). "Likelihood, Fisher information, and systematics of cosmic microwave background experiments". In: *Astronomy &amp Astrophysics* 542, A60. DOI: 10.1051/0004-6361/201219293. URL: https://doi.org/10.1051%2F0004-6361%2F201219293.

Falck, B. et al. (Mar. 2017). "The Effect of Corner Modes in the Initial Conditions of Cosmological Simulations". In: *The Astrophysical Journal* 837.2, p. 181. DOI: 10.3847/1538-4357/aa60c7. URL: https://doi.org/10.3847%2F1538-4357%2Faa60c7.

Feldman, Hume A., Nick Kaiser, and John A. Peacock (May 1994). "Power-spectrum analysis of three-dimensional redshift surveys". In: *The Astrophysical Journal* 426, p. 23. DOI: 10.1086/174036. URL: https://doi.org/10.1086%2F174036.

Fry, J. N. (Feb. 1984). "Galaxy N-point correlation functions - Theoretical amplitudes for arbitrary N". In: 277, pp. L5–L8. DOI: 10.1086/184189.

Garriga, Jaume, Mario Livio, and Alexander Vilenkin (Dec. 1999). "Cosmological constant and the time of its dominance". In: *Physical Review D* 61.2. DOI: 10.1103/physrevd.61.023503. URL: https://doi.org/10.1103%2Fphysrevd.61.023503.

Gaztanaga, Enrique, Camille Bonvin, and Lam Hui (Jan. 2017). "Measurement of the dipole in the cross-correlation function of galaxies". In: *Journal of Cosmology and Astroparticle Physics* 2017.01, pp. 032–032. DOI: 10.1088/1475-7516/2017/01/032. URL: https://doi.org/10.1088/1475-7516/2017/01/032.

Gonzalez, J. Alberto Vazquez, Luis E. Padilla, and Tonatiuh Matos (Jan. 2020). "Inflationary cosmology: from theory to observations". In: *Revista Mexicana de Fı sica E* 17.1 Jan-Jun, pp. 73–91. DOI: 10.31349/revmexfise.17.73. URL: https://doi.org/10.31349%2Frevmexfise.17.73.

Green, Stephen R. and Robert M. Wald (Mar. 2012). "Newtonian and relativistic cosmologies". In: *Phys. Rev. D* 85 (6), p. 063512. DOI: 10.1103/PhysRevD.85.063512. URL: https://link.aps.org/doi/10.1103/PhysRevD.85.063512.

Grimm, Nastassia, Fulvio Scaccabarozzi, et al. (Nov. 2020). "Galaxy power spectrum in general relativity". In: *Journal of Cosmology and Astroparticle Physics* 2020.11, pp. 064–064. DOI: 10.1088/1475-7516/2020/11/064. URL: https://doi.org/10.1088%2F1475-7516%2F2020%2F11%2F064.

Grimm, Nastassia and Jaiyul Yoo (Oct. 2021). "General relativistic effects in weak lensing angular power spectra". In: *Phys. Rev. D* 104 (8), p. 083548. DOI: 10.1103/

PhysRevD.104.083548. URL: https://link.aps.org/doi/10.1103/PhysRevD.104.083548.

Hahn, Oliver and Tom Abel (July 2011). "Multi-scale initial conditions for cosmological simulations". In: *Monthly Notices of the Royal Astronomical Society* 415.3, pp. 2101–2121. DOI: 10.1111/j.1365-2966.2011.18820.x. URL: https://doi.org/10.1111%2Fj.1365-2966.2011.18820.x.

Hamilton, A. J. S. (1998). "Linear Redshift Distortions: A Review". In: *Astrophysics and Space Science Library*. Springer Netherlands, pp. 185–275. DOI: 10.1007/978-94-011-4960-0_17. URL: https://doi.org/10.1007%2F978-94-011-4960-0_17.

— (Apr. 2001). "Formulae for growth factors in expanding universes containing matter and a cosmological constant". In: *Monthly Notices of the Royal Astronomical Society* 322.2, pp. 419–425. ISSN: 0035-8711. DOI: 10.1046/j.1365-8711.2001.04137.x. eprint: https://academic.oup.com/mnras/article-pdf/322/2/419/2862567/322-2-419.pdf. URL: https://doi.org/10.1046/j.1365-8711.2001.04137.x.

Hamilton, A. J. S., Max Tegmark, and Nikhil Padmanabhan (Sept. 2000). "Linear redshift distortions and power in the IRAS Point Source Catalog Redshift Survey". In: *Monthly Notices of the Royal Astronomical Society* 317.1, pp. L23–L27. ISSN: 1365-2966. DOI: 10.1046/j.1365-8711.2000.03888.x. URL: http://dx.doi.org/10.1046/j.1365-8711.2000.03888.x.

Hand, Nick et al. (July 2017). "An optimal FFT-based anisotropic power spectrum estimator". In: *Journal of Cosmology and Astroparticle Physics* 2017.07, pp. 002–002. ISSN: 1475-7516. DOI: 10.1088/1475-7516/2017/07/002. URL: http://dx.doi.org/10.1088/1475-7516/2017/07/002.

Hartley, W G et al. (Oct. 2021). "Dark Energy Survey Year 3 Results: Deep Field optical near-infrared images and catalogue". In: *Monthly Notices of the Royal Astronomical Society* 509.3, pp. 3547–3579. DOI: 10.1093/mnras/stab3055. URL: https://doi.org/10.1093%2Fmnras%2Fstab3055.

Heath, Anna, Ioanna Manolopoulou, and Gianluca Baio (July 2015). "A Review of Methods for the Analysis of the Expected Value of Information". In: *Medical Decision Making* 37. DOI: 10.1177/0272989X17697692.

Hockney, R and J Eastwood (1981). "Computer simulations using particles mcgraw-hill". In: *New York* 61.

Hubble, Edwin (Mar. 1929). "A Relation between Distance and Radial Velocity among Extra-Galactic Nebulae". In: *Proceedings of the National Academy of Science* 15.3, pp. 168–173. DOI: 10.1073/pnas.15.3.168.

Hui, Lam, Enrique Gaztañ aga, and Marilena LoVerde (Mar. 2008). "Anisotropic magnification distortion of the 3D galaxy correlation. II. Fourier and redshift space".

In: *Physical Review D* 77.6. DOI: 10.1103/physrevd.77.063526. URL: https://doi.org/10.1103%2Fphysrevd.77.063526.

Jeong, Donghui (Aug. 2010). "Cosmology with high (z > 1) redshift galaxy surveys". In: pp. 260–295.

Jeong, Donghui, Fabian Schmidt, and Christopher M. Hirata (Jan. 2012). "Large-scale clustering of galaxies in general relativity". In: *Physical Review D* 85.2. DOI: 10.1103/physrevd.85.023504. URL: https://doi.org/10.1103%2Fphysrevd.85.023504.

Jing, Y. P. (Feb. 2005). "Correcting for the Alias Effect When Measuring the Power Spectrum Using a Fast Fourier Transform". In: *The Astrophysical Journal* 620.2, pp. 559–563. DOI: 10.1086/427087. URL: https://doi.org/10.1086%2F427087.

Kaiser, Nick (June 1987). "Clustering in real space and in redshift space". In: 227, pp. 1–21. DOI: 10.1093/mnras/227.1.1.

Kamionkowski, Marc, Arthur Kosowsky, and Albert Stebbins (June 1997). "Statistics of cosmic microwave background polarization". In: *Phys. Rev. D* 55 (12), pp. 7368–7388. DOI: 10.1103/PhysRevD.55.7368. URL: https://link.aps.org/doi/10.1103/PhysRevD.55.7368.

Karachentsev, I. D. et al. (Oct. 2006). "Peculiar velocities of 3000 spiral galaxies from the 2MFGC catalog". In: *Astrophysics* 49.4, pp. 450–461. DOI: 10.1007/s10511-006-0044-9. arXiv: astro-ph/0611945 [astro-ph].

Kravtsov, Andrey V. and Stefano Borgani (2012). "Formation of Galaxy Clusters". In: *Annual Review of Astronomy and Astrophysics* 50.1, pp. 353–409. DOI: 10.1146/annurev-astro-081811-125502. eprint: https://doi.org/10.1146/annurev-astro-081811-125502. URL: https://doi.org/10.1146/annurev-astro-081811-125502.

Kwak, Sang and Jong Kim (Apr. 2017). "Central limit theorem: The cornerstone of modern statistics". In: *Korean Journal of Anesthesiology* 70, p. 144. DOI: 10.4097/kjae.2017.70.2.144.

Lewis, Antony and Sarah Bridle (Nov. 2002). "Cosmological parameters from CMB and other data: A Monte Carlo approach". In: *Phys. Rev. D* 66 (10), p. 103511. DOI: 10.1103/PhysRevD.66.103511. URL: https://link.aps.org/doi/10.1103/PhysRevD.66.103511.

Linder, Eric V. (Mar. 2003). "Exploring the Expansion History of the Universe". In: *Phys. Rev. Lett.* 90 (9), p. 091301. DOI: 10.1103/PhysRevLett.90.091301. URL: https://link.aps.org/doi/10.1103/PhysRevLett.90.091301.

— (Aug. 2005). "Cosmic growth history and expansion history". In: *Physical Review D* 72.4. DOI: 10.1103/physrevd.72.043529. URL: https://doi.org/10.1103%2Fphysrevd.72.043529.

Lokas, E. L. (Jan. 2000). "Universal profile of dark matter haloes and the spherical infall model". In: *Monthly Notices of the Royal Astronomical Society* 311.2, pp. 423–432. DOI: 10.1046/j.1365-8711.2000.03082.x. URL: https://doi.org/10.1046%2Fj.1365-8711.2000.03082.x.

Lorenz, Christiane S., David Alonso, and Pedro G. Ferreira (Jan. 2018). "Impact of relativistic effects on cosmological parameter estimation". In: *Physical Review D* 97.2. DOI: 10.1103/physrevd.97.023537. URL: https://doi.org/10.1103%2Fphysrevd.97.023537.

Margony, Bruce (Jan. 1999). "The Sloan Digital Sky Survey". In: *Philosophical Transactions of the Royal Society of London. Series A: Mathematical, Physical and Engineering Sciences* 357.1750. Ed. by G. P. Efstathiou et al., pp. 93–103. DOI: 10.1098/rsta.1999.0316. URL: https://doi.org/10.1098%2Frsta.1999.0316.

Matarrese, Sabino, Marcello A Musso, and Antonio Riotto (May 2004). "The influence of super-horizon scales on cosmological observables generated during inflation". In: *Journal of Cosmology and Astroparticle Physics* 2004.05, pp. 008–008. DOI: 10.1088/1475-7516/2004/05/008. URL: https://doi.org/10.1088/1475-7516/2004/05/008.

Matsubara, Takahiko (June 2000). "The Gravitational Lensing in Redshift-Space Correlation Functions of Galaxies and Quasars". In: *The Astrophysical Journal* 537.2, pp. L77–L80. DOI: 10.1086/312762. URL: https://doi.org/10.1086/312762.

Meerburg, P. Daniel et al. (2019). *Primordial Non-Gaussianity*. DOI: 10.48550/ARXIV.1903.04409. URL: https://arxiv.org/abs/1903.04409.

N. Aghanim, and et al. (Sept. 2020). "iPlanck/i 2018 results". In: *Astronomy &amp Astrophysics* 641, A6. DOI: 10.1051/0004-6361/201833910. URL: https://doi.org/10.1051%2F0004-6361%2F201833910.

Nandi, Debottam (2017a). *Hamiltonian formalism of cosmological perturbations and higher derivative theories*. DOI: 10.48550/ARXIV.1707.02976. URL: https://arxiv.org/abs/1707.02976.

— (July 2017b). "Hamiltonian formalism of cosmological perturbations and higher derivative theories". In.

Oh, Siang Peng, David N. Spergel, and Gary Hinshaw (Jan. 1999). "An Efficient Technique to Determine the Power Spectrum from Cosmic Microwave Background Sky Maps". In: *The Astrophysical Journal* 510.2, pp. 551–563. ISSN: 1538-4357. DOI: 10.1086/306629. URL: http://dx.doi.org/10.1086/306629.

Okumura, Teppei et al. (Nov. 2015). "Galaxy power spectrum in redshift space: Combining perturbation theory with the halo model". In: *Physical Review D* 92.10. DOI: 10.1103/physrevd.92.103516. URL: https://doi.org/10.1103%2Fphysrevd.92.103516.

P. A. R. Ade, and et al. (Sept. 2016). “iPlanck/i2015 results”. In: *Astronomy &amp Astrophysics* 594, A13. DOI: 10.1051/0004-6361/201525830. URL: https://doi.org/10.1051%2F0004-6361%2F201525830.

Padmanabhan, T. (1995). “Structure formation: Models, Dynamics and Status”. In: DOI: 10.48550/ARXIV.ASTRO-PH/9508121. URL: https://arxiv.org/abs/astro-ph/9508121.

Pápai, Pé ter and István Szapudi (Sept. 2008). “Non-perturbative effects of geometry in wide-angle redshift distortions”. In: *Monthly Notices of the Royal Astronomical Society* 389.1, pp. 292–296. DOI: 10.1111/j.1365-2966.2008.13572.x. URL: https://doi.org/10.1111%2Fj.1365-2966.2008.13572.x.

Peacock, J. A. (1998). *Cosmological Physics*. Cambridge University Press. DOI: 10.1017/CBO9780511804533.

Peacock, J. A. and D. Nicholson (Nov. 1991). “The large-scale clustering of radio galaxies”. In: *Monthly Notices of the Royal Astronomical Society* 253.2, pp. 307–319. ISSN: 0035-8711. DOI: 10.1093/mnras/253.2.307. eprint: https://academic.oup.com/mnras/article-pdf/253/2/307/32290448/mnras253-0307.pdf. URL: https://doi.org/10.1093/mnras/253.2.307.

Peebles, P. J. E. (1980a). *The large-scale structure of the universe*.

— (1980b). *The large-scale structure of the universe*.

— (Dec. 1982). “Large-scale background temperature and mass fluctuations due to scale-invariant primeval perturbations”. In: 263, pp. L1–L5. DOI: 10.1086/183911.

Percival, Will J. et al. (Nov. 2001). “The 2dF Galaxy Redshift Survey: the power spectrum and the matter content of the Universe”. In: *Monthly Notices of the Royal Astronomical Society* 327.4, pp. 1297–1306. ISSN: 0035-8711. DOI: 10.1046/j.1365-8711.2001.04827.x. eprint: https://academic.oup.com/mnras/article-pdf/327/4/1297/3279954/327-4-1297.pdf. URL: https://doi.org/10.1046/j.1365-8711.2001.04827.x.

Philcox, Oliver (2020). “Cosmology without windows”. In: *Phys. Rev. D 103, 103504 (2021)*. URL: arXiv:2012.09389%20[astro-ph.CO].

Philcox, Oliver H. E. (Dec. 2021). “Cosmology without window functions. II. Cubic estimators for the galaxy bispectrum”. In: *Phys. Rev. D* 104 (12), p. 123529. DOI: 10.1103/PhysRevD.104.123529. URL: https://link.aps.org/doi/10.1103/PhysRevD.104.123529.

Philcox, Oliver H. E. and Mikhail M. Ivanov (Feb. 2022). “BOSS DR12 full-shape cosmology: constraints from the large-scale galaxy power spectrum and bispectrum monopole”. In: *Physical Review D* 105.4. ISSN: 2470-0029. DOI: 10.1103/physrevd.105.043517. URL: http://dx.doi.org/10.1103/PhysRevD.105.043517.

Pozzetti, L. et al. (Apr. 2016). "Modelling the number density of Hiα/iemitters for future spectroscopic near-IR space missions". In: *Astronomy &amp Astrophysics* 590, A3. DOI: 10.1051/0004-6361/201527081. URL: https://doi.org/10.1051%2F0004-6361%2F201527081.

Praton, Elizabeth A., Adrian L. Melott, and Margaret Q. McKee (Apr. 1997). "The Bull's-Eye Effect: Are Galaxy Walls Observationally Enhanced?" In: *The Astrophysical Journal* 479.1, pp. L15–L18. DOI: 10.1086/310567. URL: https://doi.org/10.1086/310567.

R. Scaramella, and et al. (June 2022). "iEuclid/i preparation". In: *Astronomy &amp Astrophysics* 662, A112. DOI: 10.1051/0004-6361/202141938. URL: https://doi.org/10.1051%2F0004-6361%2F202141938.

Raccanelli, Alvise, Daniele Bertacca, Olivier Doré, et al. (Aug. 2014). "Large-scale 3D galaxy correlation function and non-Gaussianity". In: *Journal of Cosmology and Astroparticle Physics* 2014.08, pp. 022–022. DOI: 10.1088/1475-7516/2014/08/022. URL: https://doi.org/10.1088/1475-7516/2014/08/022.

Raccanelli, Alvise, Daniele Bertacca, Donghui Jeong, et al. (2016). *Doppler term in the galaxy two-point correlation function: wide-angle, velocity, Doppler lensing and cosmic acceleration effects*. DOI: 10.48550/ARXIV.1602.03186. URL: https://arxiv.org/abs/1602.03186.

Raccanelli, Alvise, Daniele Bertacca, Roy Maartens, et al. (June 2016). "Lensing and time-delay contributions to galaxy correlations". In: *General Relativity and Gravitation* 48.7. DOI: 10.1007/s10714-016-2076-8. URL: https://doi.org/10.1007%2Fs10714-016-2076-8.

Raccanelli, Alvise, Francesco Montanari, et al. (May 2016). "Cosmological measurements with general relativistic galaxy correlations". In: *Journal of Cosmology and Astroparticle Physics* 2016.05, pp. 009–009. DOI: 10.1088/1475-7516/2016/05/009. URL: https://doi.org/10.1088%2F1475-7516%2F2016%2F05%2F009.

Raccanelli, Alvise, Lado Samushia, and Will J. Percival (Sept. 2010). "Simulating redshift-space distortions for galaxy pairs with wide angular separation". In: *Monthly Notices of the Royal Astronomical Society* 409.4, pp. 1525–1533. DOI: 10.1111/j.1365-2966.2010.17388.x. URL: https://doi.org/10.1111%2Fj.1365-2966.2010.17388.x.

Ryden, B. (2017). *Introduction to Cosmology*. Cambridge University Press. ISBN: 9781107154834. URL: https://books.google.it/books?id=07WSDQAAQBAJ.

Sasaki, Misao (Oct. 1987). "The magnitude–redshift relation in a perturbed Friedmann universe". In: *Monthly Notices of the Royal Astronomical Society* 228.3, pp. 653–669. ISSN: 0035-8711. DOI: 10.1093/mnras/228.3.653. eprint: https://academic.oup.com/mnras/article-pdf/228/3/653/18522427/

mnras228-0653.pdf. URL: https://doi.org/10.1093/mnras/228.3.653.

Scoccimarro, R. (Oct. 1998). "Transients from initial conditions: a perturbative analysis". In: *Monthly Notices of the Royal Astronomical Society* 299.4, pp. 1097–1118. DOI: 10.1046/j.1365-8711.1998.01845.x. URL: https://doi.org/10.1046%2Fj.1365-8711.1998.01845.x.

Sefusatti, E. et al. (May 2016). "Accurate estimators of correlation functions in Fourier space". In: *Monthly Notices of the Royal Astronomical Society* 460.4, pp. 3624–3636. DOI: 10.1093/mnras/stw1229. URL: https://doi.org/10.1093%2Fmnras%2Fstw1229.

Sevilla-Noarbe, I. et al. (May 2021). "Dark Energy Survey Year 3 Results: Photometric Data Set for Cosmology". In: *The Astrophysical Journal Supplement Series* 254.2, p. 24. DOI: 10.3847/1538-4365/abeb66. URL: https://doi.org/10.3847%2F1538-4365%2Fabeb66.

Shapiro, Irwin I. (Dec. 1964). "Fourth Test of General Relativity". In: *Phys. Rev. Lett.* 13 (26), pp. 789–791. DOI: 10.1103/PhysRevLett.13.789. URL: https://link.aps.org/doi/10.1103/PhysRevLett.13.789.

Sheth, Ravi K. and Antonaldo Diaferio (Apr. 2001). "Peculiar velocities of galaxies and clusters". In: *Monthly Notices of the Royal Astronomical Society* 322.4, pp. 901–917. ISSN: 0035-8711. DOI: 10.1046/j.1365-8711.2001.04202.x. eprint: https://academic.oup.com/mnras/article-pdf/322/4/901/3339045/322-4-901.pdf. URL: https://doi.org/10.1046/j.1365-8711.2001.04202.x.

Sheth, Ravi K., H. J. Mo, and Giuseppe Tormen (May 2001). "Ellipsoidal collapse and an improved model for the number and spatial distribution of dark matter haloes". In: *Monthly Notices of the Royal Astronomical Society* 323.1, pp. 1–12. ISSN: 0035-8711. DOI: 10.1046/j.1365-8711.2001.04006.x. eprint: https://academic.oup.com/mnras/article-pdf/323/1/1/3204200/323-1-1.pdf. URL: https://doi.org/10.1046/j.1365-8711.2001.04006.x.

Slosar, Anž e et al. (Aug. 2008). "Constraints on local primordial non-Gaussianity from large scale structure". In: *Journal of Cosmology and Astroparticle Physics* 2008.08, p. 031. DOI: 10.1088/1475-7516/2008/08/031. URL: https://doi.org/10.1088%2F1475-7516%2F2008%2F08%2F031.

Somerville, Rachel S. and Romeel Davé (2015). "Physical Models of Galaxy Formation in a Cosmological Framework". In: *Annual Review of Astronomy and Astrophysics* 53.1, pp. 51–113. DOI: 10.1146/annurev-astro-082812-140951. eprint: https://doi.org/10.1146/annurev-astro-082812-140951. URL: https://doi.org/10.1146/annurev-astro-082812-140951.

Strauss, Michael A. and Jeffrey A. Willick (Aug. 1995). "The density and peculiar velocity fields of nearby galaxies". In: *Physics Reports* 261.5-6, pp. 271–431. DOI: 10.1016/0370-1573(95)00013-7. URL: https://doi.org/10.1016%2F0370-1573%2895%2900013-7.

Strauss, Michael A., Amos Yahil, et al. (Oct. 1992). "A Redshift Survey of IRAS Galaxies. V. The Acceleration on the Local Group". In: 397, p. 395. DOI: 10.1086/171796.

Tegmark, M., A. J. S. Hamilton, and Y. Xu (Oct. 2002). "The power spectrum of galaxies in the 2dF 100k redshift survey". In: *Monthly Notices of the Royal Astronomical Society* 335.4, pp. 887–908. ISSN: 1365-2966. DOI: 10.1046/j.1365-8711.2002.05622.x. URL: http://dx.doi.org/10.1046/j.1365-8711.2002.05622.x.

Tegmark, Max, Michael R. Blanton, et al. (May 2004). "The Three-Dimensional Power Spectrum of Galaxies from the Sloan Digital Sky Survey". In: *The Astrophysical Journal* 606.2, pp. 702–740. ISSN: 1538-4357. DOI: 10.1086/382125. URL: http://dx.doi.org/10.1086/382125.

Tegmark, Max, Scott Dodelson, et al. (May 2002). "The Angular Power Spectrum of Galaxies from Early Sloan Digital Sky Survey Data". In: *The Astrophysical Journal* 571.1, pp. 191–205. ISSN: 1538-4357. DOI: 10.1086/339894. URL: http://dx.doi.org/10.1086/339894.

Tegmark, Max, Andrew J. S. Hamilton, et al. (June 1998). "Measuring the Galaxy Power Spectrum with Future Redshift Surveys". In: *The Astrophysical Journal* 499.2, pp. 555–576. DOI: 10.1086/305663. URL: https://doi.org/10.1086%2F305663.

Tegmark, Max, Andy N. Taylor, and Alan F. Heavens (May 1997). "Karhunen-Loeve Eigenvalue Problems in Cosmology: How Should We Tackle Large Data Sets?" In: *The Astrophysical Journal* 480.1, pp. 22–35. DOI: 10.1086/303939. URL: https://doi.org/10.1086%2F303939.

Troxel, M.A, Austin Peel, and Mustapha Ishak (Dec. 2013). "Effects of anisotropy on gravitational infall in galaxy clusters using an exact general relativistic model". In: *Journal of Cosmology and Astroparticle Physics* 2013.12, pp. 048–048. DOI: 10.1088/1475-7516/2013/12/048. URL: https://doi.org/10.1088%2F1475-7516%2F2013%2F12%2F048.

Tsujikawa, Shinji (2003). *Introductory review of cosmic inflation*. DOI: 10.48550/ARXIV.HEP-PH/0304257. URL: https://arxiv.org/abs/hep-ph/0304257.

Turok, N. (2002). "A critical review of inflation". In: *Class. Quant. Grav.* 19. Ed. by P. Dunsby, G. Ellis, and Roy Maartens, pp. 3449–3467. DOI: 10.1088/0264-9381/19/13/305.

Uggla, Claes and John Wainwright (Aug. 2011). "Cosmological perturbation theory revisited". In: *Classical and Quantum Gravity* 28.17, p. 175017. DOI: 10.1088/0264-9381/28/17/175017. URL: https://doi.org/10.1088%2F0264-9381%2F28%2F17%2F175017.

Unruh, Sandra et al. (June 2020). "The importance of magnification effects in galaxy-galaxy lensing". In: *Astronomy &amp Astrophysics* 638, A96. DOI: 10.1051/0004-6361/201936915. URL: https://doi.org/10.1051%2F0004-6361%2F201936915.

Valentino, Eleonora Di et al. (July 2021). "In the realm of the Hubble tension—a review of solutions sup$*$/*sup*". In: *Classical and Quantum Gravity* 38.15, p. 153001. DOI: 10.1088/1361-6382/ac086d. URL: https://doi.org/10.1088/1361-6382/ac086d.

Velten, H. E. S., R. F. vom Marttens, and W. Zimdahl (Nov. 2014). "Aspects of the cosmological "coincidence problem"". In: *The European Physical Journal C* 74.11. DOI: 10.1140/epjc/s10052-014-3160-4. URL: https://doi.org/10.1140%2Fepjc%2Fs10052-014-3160-4.

Vogeley, Michael S. and Alexander S. Szalay (July 1996). "Eigenmode Analysis of Galaxy Redshift Surveys. I. Theory and Methods". In: 465, p. 34. DOI: 10.1086/177399. arXiv: astro-ph/9601185 [astro-ph].

Walker, Stephen et al. (Jan. 2019). "The Physics of Galaxy Cluster Outskirts". In: *Space Science Reviews* 215.1. DOI: 10.1007/s11214-018-0572-8. URL: https://doi.org/10.1007%2Fs11214-018-0572-8.

Wechsler, Risa H. and Jeremy L. Tinker (Sept. 2018). "The Connection Between Galaxies and Their Dark Matter Halos". In: *Annual Review of Astronomy and Astrophysics* 56.1, pp. 435–487. DOI: 10.1146/annurev-astro-081817-051756. URL: https://doi.org/10.1146%2Fannurev-astro-081817-051756.

Weltman, A. et al. (2020). "Fundamental physics with the Square Kilometre Array". In: *Publications of the Astronomical Society of Australia* 37. DOI: 10.1017/pasa.2019.42. URL: https://doi.org/10.1017%2Fpasa.2019.42.

White, S. D. M. (Jan. 1979). "The hierarchy of correlation functions and its relation to other measures of galaxy clustering." In: 186, pp. 145–154. DOI: 10.1093/mnras/186.2.145.

Yamamoto, Kazuhiro, Masashi Nakamichi, et al. (Feb. 2006). "A Measurement of the Quadrupole Power Spectrum in the Clustering of the 2dF QSO Survey". In: *Publications of the Astronomical Society of Japan* 58.1, pp. 93–102. ISSN: 2053-051X. DOI: 10.1093/pasj/58.1.93. URL: http://dx.doi.org/10.1093/pasj/58.1.93.

Yamamoto, Kazuhiro, Hiroaki Nishioka, and Yasushi Suto (Dec. 1999). "The Cosmological Light-Cone Effect on the Power Spectrum of Galaxies and Quasars in Wide-

Field Redshift Surveys". In: *The Astrophysical Journal* 527.2, pp. 488–497. DOI: 10.1086/308126. URL: https://doi.org/10.1086%2F308126.

Yang, Weiqiang et al. (Dec. 2018). "Interacting dark energy with time varying equation of state and the mml:math xmlns:mml="http://www.w3.org/1998/Math/MathML" display="inline"mml:msubmml:miH/mml:mimml:mn0/mml:mn/mml:msub/mml:math tension". In: *Physical Review D* 98.12. DOI: 10.1103/physrevd.98.123527. URL: https://doi.org/10.1103%2Fphysrevd.98.123527.

Yoo, Jaiyul (Jan. 2009a). "Complete treatment of galaxy two-point statistics: Gravitational lensing effects and redshift-space distortions". In: *Phys. Rev. D* 79 (2), p. 023517. DOI: 10.1103/PhysRevD.79.023517. URL: https://link.aps.org/doi/10.1103/PhysRevD.79.023517.

— (Jan. 2009b). "Complete treatment of galaxy two-point statistics: Gravitational lensing effects and redshift-space distortions". In: *Physical Review D* 79.2. DOI: 10.1103/physrevd.79.023517. URL: https://doi.org/10.1103%2Fphysrevd.79.023517.

Yoo, Jaiyul and Uroš Seljak (Dec. 2014). "Wide-angle effects in future galaxy surveys". In: *Monthly Notices of the Royal Astronomical Society* 447.2, pp. 1789–1805. ISSN: 0035-8711. DOI: 10.1093/mnras/stu2491. eprint: https://academic.oup.com/mnras/article-pdf/447/2/1789/8093828/stu2491.pdf. URL: https://doi.org/10.1093/mnras/stu2491.

Young, G. Alastair (2019). "Mathematical Statistics: An Introduction to Likelihood Based Inference Richard J. Rossi John Wiley & Sons, 2018, xv + 422 pages, £85.99, ebook ISBN: 978-1-118-77104-4, LCCN 2018010628 (ebook)". In: *International Statistical Review* 87.1, pp. 178–179. DOI: https://doi.org/10.1111/insr.12315. eprint: https://onlinelibrary.wiley.com/doi/pdf/10.1111/insr.12315. URL: https://onlinelibrary.wiley.com/doi/abs/10.1111/insr.12315.